

AN ABSTRACT OF THE THESIS OF

Thomas D. Walsh for the degree of Master of Science in Atmospheric Sciences
presented on June 27, 1994.

Title: Tracer Transport in the Martian Atmosphere as Simulated by a Mars GCM

Abstract Approved: Redacted for Privacy 18/94

This paper investigates the atmospheric circulation and transport characteristics of the Martian atmosphere (as modeled by a Mars GCM) for three sets of conditions. The conditions are based on a combination of season and dust loading (as parameterized by the optical depth, τ). The first experiment is for the Northern Spring Equinox with no dust loading ($\tau = 0$). Experiment 2 is for Northern Hemisphere Winter Solstice with no dust loading. Experiment 3 is for Northern Hemisphere Winter Solstice under moderately dusty conditions ($\tau = 1.0$). These cases allow a comparison between seasons and a look at the effects of dust in the atmosphere on the circulation and transport processes.

After presenting some of the theoretical and mathematical background pertinent to atmospheric transport and circulation the results of the study are given. These include analyses of the zonal-mean winds, the time-evolution of the mean tracer field, the mean meridional circulation, and the effective transport circulation

[Plumb and Mahlman, 1987]. In addition we estimate the time scales for "stratospheric" overturning and calculate a set of eddy diffusion coefficients (K_{yy} and K_{zz}) for each case.

These coefficients are a means of parameterizing the strength of eddy mixing. Others [Conrath, 1971; Zurek, 1976; Kong and McElroy, 1977; Toon et al., 1977; Anderson and Leovy, 1987] have estimated, using various methods, values for the vertical diffusion coefficient K_{zz} of the order of 10^3 m²/s. The results here show that there is no "typical" value of K_{zz} (or K_{yy}) which can be used to characterize the atmosphere globally, and K_{zz} seldom reaches 10^3 m²/s except in isolated regions and/or under dusty conditions. Both K_{yy} and K_{zz} are dependent upon season, dust loading, and location in the atmosphere. In addition to identifying the regions of strong mixing, probable sources of the eddy activity which is responsible for the mixing are discussed.

In all three cases the effective transport circulation (which includes both advection and diffusion) is structurally similar to the mean meridional circulation but somewhat more intense. The Martian equinox circulation is structurally similar to Earth's circulation; both are characterized by a dual Hadley cell system with rising branch over the equator, poleward flow aloft, and return flow at low levels. The mean zonal winds are westerly in both hemispheres with easterlies near the ground and at high altitudes over the equator. The jet stream in the northern hemisphere peaks at 45 m/s at equinox.

Unlike the Earth, Mars' circulation changes dramatically with the seasons. For solstice conditions the mean meridional circulation is characterized by a

large, intense cross-equatorial Hadley cell which dominates the circulation pattern. The mean zonal winds are now predominately westerly in the northern winter hemisphere and easterly in the southern hemisphere. The westerly jet reaches 95 m/s while the easterly jet reaches 30 m/s. There is a band of westerlies (up to 10 m/s) found in low southern latitudes near the ground. Dust in the atmosphere acts to intensify the strength of the circulation (while having little effect on the structure); there is a two- to three-fold increase in the strength of the mean winds between the two winter solstice experiments.

**Tracer Transport in the Martian
Atmosphere as Simulated by a Mars GCM**

by

Thomas D. Walsh

**A THESIS
submitted to
Oregon State University**

**in partial fulfillment of
the requirements for the
degree of**

Master of Science

Completed June 27, 1994

Commencement June 1995

APPROVED:

Redacted for Privacy

7/18/94

Professor of Atmospheric Science in charge of major

Redacted for Privacy

7/18/94

Dean of College of Oceanic and Atmospheric Sciences

Redacted for Privacy

Dean of Graduate School

↓

Date thesis is presented June 27, 1994

Typed by researcher for Thomas D. Walsh

ACKNOWLEDGMENTS

“If the gods could build me a ladder to the heavens, I’d climb the ladder and drop a big elbow on the world.”

— Cactus Jack

I would like to thank all of the people who in some way encouraged me in the research, writing, and defense of this thesis. More specifically, . . .

I would like to thank my family, especially Mom, Dad, and Julie, for their support throughout the past three years.

Many thanks go to Andy Kowalski, Cole McCandlish, Dean Vickers, and John Wong for their help with understanding(?) computers and dealing with the O.S.U. bureaucracy (which I must acknowledge for the pain in the rear it is!).

I would like to thank Dr. Jeff Barnes, my major advisor, for his guidance, input, encouragement, editing, and funding for this project. In addition, I would like to thank those scientists at NASA Ames who contributed the data for this research (especially, Dr. Jim Murphy).

I also wish to thank my church family from Grant Avenue Baptist Church for the many prayers, friendships, meals, and housing arrangements which have seen me through the past three years.

A special thank you also goes out to Dennis and Barbara Donivan for their concern and care for me. Their generosity cannot not be described nor could I begin to even repay them for their kindness. May God bless you both in all things!

And, speaking of God, I must not neglect to thank my Savior Jesus Christ who has provided for me every step of the way here in Oregon. You would not

let me quit and for that I thank You. I hope that while this work was being done
I may have honored and glorified You in some way!

Table of Contents

Chapter 1	Introduction	1
Chapter 2	Eddy Diffusion and Tracer Transport Theory	6
2.1	Eddy Diffusion	6
2.2	Tracer Transport	10
2.3	The K Tensor	15
2.4	The Mean Meridional Circulation	17
Chapter 3	Methodology and Procedures	22
3.1	The Mars GCM	23
3.2	The Aerosol Transport Model	25
3.3	Computation of K values	28
Chapter 4	Results	33
4.1	Experiment 1: Northern Spring Equinox	33
4.2	Experiment 2: Northern Winter Solstice (no dust loading)	62
4.3	Experiment 3: Northern Winter Solstice (with dust)	89
4.4	Time Scales for Atmospheric Overturning	117
Chapter 5	Summary and Conclusions	125
5.1	Mean Meridional Circulations	125
5.2	Transport Circulations	127
5.3	Eddy Diffusion Coefficients	127
5.4	Transport Time Scales	129
5.5	Conclusions	130
Bibliography		132

List of Figures

Figure 1	Illustrating the difference between the transport circulation U_T and Lagrangian mean circulation \bar{u}^L in the presence of inhomogeneous diffusion. The reference point B moves with the transport circulation; the center of mass C moves with the Lagrangian mean velocity. If the diffusion about B is inhomogeneous, C moves relative to B and therefore the two velocities differ under such circumstances. [Reproduced from Plumb and Mahlman, 1987.] . . . 21
Figure 2	Time-averaged mean zonal winds for Spring equinox. 35
Figure 3	Time-averaged mean meridional winds for Spring equinox. 36
Figure 4	Time-averaged mean vertical winds for Spring equinox. 37
Figure 5	Initial distribution of the mean mixing ratios for the Spring Equinox horizontally stratified case. 39
Figure 6	Distribution of the mean mixing ratios after day 3 for the Spring Equinox horizontally stratified case. . . . 40
Figure 7	Distribution of the mean mixing ratios after day 6 for the Spring Equinox horizontally stratified case. . . . 41
Figure 8	Distribution of the mean mixing ratios after day 10 for the Spring Equinox horizontally stratified case. . . 42
Figure 9	Initial distribution of the mean mixing ratios for the Spring Equinox vertically stratified case. 43
Figure 10	Distribution of the mean mixing ratios after day 3 for the Spring Equinox vertically stratified case. 44
Figure 11	Distribution of the mean mixing ratios after day 6 for the Spring Equinox vertically stratified case. 45

Figure 12	Distribution of the mean mixing ratios after day 10 for the Spring Equinox vertically stratified case. . .	46
Figure 13	Time-averaged mean mixing ratios and eddy fluxes for the Spring Equinox horizontally stratified case. .	47
Figure 14	Time-averaged mean mixing ratios and eddy fluxes for the Spring Equinox vertically stratified case. . .	48
Figure 15	Mean meridional circulation for the Spring equinox case.	50
Figure 16	Effective transport circulation for the Spring equinox case.	52
Figure 17	Distribution of K_{yy} , the horizontal eddy diffusion coefficient, for the Spring Equinox case.	54
Figure 18	Distribution of K_{zz} , the vertical eddy diffusion coefficient, for the Spring Equinox case.	55
Figure 19	Distribution of the transient eddy horizontal heat fluxes (after low-pass filtering) showing the regions of significant transient eddy activity.	59
Figure 20	Distribution of the transient eddy vertical heat fluxes (after low-pass filtering) showing the regions of significant transient eddy activity.	60
Figure 21	Distribution of the transient rms temperature variance (after high-pass filtering) showing the influence of the thermal tide.	61
Figure 22	Time-averaged mean zonal winds for the northern hemisphere winter solstice case with no dust loading.	63
Figure 23	Time-averaged mean meridional winds for the northern hemisphere winter solstice case with no dust loading.	64
Figure 24	Time-averaged mean vertical winds for the northern hemisphere winter solstice case with no dust loading.	65

Figure 25	Initial distribution of the mean mixing ratios for the horizontally stratified case. (NHWS, $\tau=0$).	68
Figure 26	Distribution of the mean mixing ratios after day 3 for the horizontally stratified case. (NHWS, $\tau=0$). . . .	69
Figure 27	Distribution of the mean mixing ratios after day 6 for the horizontally stratified case. (NHWS, $\tau=0$). . . .	70
Figure 28	Distribution of the mean mixing ratios after day 10 for the horizontally stratified case. (NHWS, $\tau=0$). . .	71
Figure 29	Initial distribution of the mean mixing ratios for the vertically stratified case. (NHWS, $\tau=0$).	72
Figure 30	Distribution of the mean mixing ratios after day 3 for the vertically stratified case. (NHWS, $\tau=0$).	73
Figure 31	Distribution of the mean mixing ratios after day 6 for the vertically stratified case. (NHWS, $\tau=0$).	74
Figure 32	Distribution of the mean mixing ratios after day 10 for the vertically stratified case. (NHWS, $\tau=0$). . . .	75
Figure 33	Time-averaged mean mixing ratios and eddy fluxes for the horizontally stratified case. (NHWS, $\tau=0$). . .	76
Figure 34	Time-averaged mean mixing ratios and eddy fluxes for the vertically stratified case. (NHWS, $\tau=0$). . . .	77
Figure 35	Mean meridional circulation for the northern hemisphere winter solstice case ($\tau=0$).	79
Figure 36	Effective transport circulation for the northern hemisphere winter solstice case ($\tau=0$).	80
Figure 37	Distribution of K_{yy} , the horizontal eddy diffusion coefficient. (NHWS, $\tau=0$).	82
Figure 38	Distribution of K_{zz} , the vertical eddy diffusion coefficient. (NHWS, $\tau=0$).	83

Figure 39	Distribution of the transient rms geopotential height variance indicating regions of significant transient eddy activity.	86
Figure 40	Distribution of the stationary rms temperature variance indicating regions of significant stationary eddy activity.	87
Figure 41	Distribution of the transient rms temperature variance showing influence of the thermal tide.	88
Figure 42	Time-averaged mean zonal winds for northern hemisphere winter solstice (with $\tau=1.0$).	90
Figure 43	Time-averaged mean meridional winds for northern hemisphere winter solstice (with $\tau=1.0$).	91
Figure 44	Time-averaged mean vertical winds for northern hemisphere winter solstice (with $\tau=1.0$).	92
Figure 45	Initial distribution of the mean mixing ratios for the horizontally stratified case. (NHWS, $\tau=1.0$)	95
Figure 46	Distribution of the mean mixing ratios after day 3 for the horizontally stratified case. (NHWS, $\tau=1.0$)	96
Figure 47	Distribution of the mean mixing ratios after day 6 for the horizontally stratified case. (NHWS, $\tau=1.0$)	97
Figure 48	Distribution of the mean mixing ratios after day 10 for the horizontally stratified case. (NHWS, $\tau=1.0$)	98
Figure 49	Initial distribution of the mean mixing ratios for the vertically stratified case. (NHWS, $\tau=1.0$)	99
Figure 50	Distribution of the mean mixing ratios after day 3 for the vertically stratified case. (NHWS, $\tau=1.0$)	100
Figure 51	Distribution of the mean mixing ratios after day 6 for the vertically stratified case. (NHWS, $\tau=1.0$)	101
Figure 52	Distribution of mean mixing ratios after day 10 for the vertically stratified case. (NHWS, $\tau=1.0$)	102

Figure 53	Time-averaged mean mixing ratios and eddy fluxes for the horizontally stratified case. (NHWS, $\tau=1.0$)	103
Figure 54	Time-averaged mean mixing ratios and eddy fluxes for the vertically stratified case. (NHWS, $\tau=1.0$)	104
Figure 55	Mean meridional circulation for the northern hemisphere winter solstice case ($\tau=1.0$)	106
Figure 56	Effective transport circulation for the northern hemisphere winter solstice case ($\tau=1.0$)	108
Figure 57	Distribution of K_{yy} , the horizontal eddy diffusion coefficient. (NHWS, $\tau=1.0$)	109
Figure 58	Distribution of K_{zz} , the vertical eddy diffusion coefficient. (NHWS, $\tau=1.0$)	110
Figure 59	Distribution of the transient eddy horizontal heat fluxes (after low-pass filtering) showing the regions of significant transient eddy activity.	113
Figure 60	Distribution of the transient eddy vertical heat fluxes (after low-pass filtering) showing the regions of significant transient eddy activity.	114
Figure 61	Distribution of the transient rms temperature variance (after high-pass filtering) showing the influence of the thermal tide.	115
Figure 62	Distribution of the stationary rms geopotential height variance showing the influence of stationary eddy activity.	116

List of Tables

Table 1	Results for time scale calculations. t_A is the advective transport time scale (for both horizontal and vertical directions), t_d is the diffusive transport time scale. 120
Table 2	Computed time scales for stratospheric overturning based on the effective transport circulation. 124

Tracer Transport in the Martian Atmosphere as Simulated by a Mars GCM

Chapter 1: Introduction

Transport can have a strong influence on chemical and photochemical processes that take place in an atmosphere. Transport efficiency has often been characterized by eddy diffusion coefficients (K values), which are frequently used by chemists and photochemists who wish to represent the various atmospheric transport processes in terms of diffusion. While work has been done [e.g., Plumb and Mahlman, 1987] to generate values of these coefficients for Earth's atmospheric transport, comparatively little has been done to evaluate them for the Martian atmosphere. The values being used at present (by photochemists) are rough estimates at best. The research presented here seeks to improve upon these estimates.

With the continuing interest in space exploration, Mars has become a focus of increased study. America's Space Exploration Initiative includes a program which hopes to land men on Mars sometime in the next century. However, before this happens there is still much that needs to be learned and understood about Mars and its atmosphere. By making use of data from previous Mars missions and general circulation models (GCM's) our understanding of the Martian atmosphere can be enhanced in advance of these missions.

As a result of spacecraft missions (such as Mariner 9 and Viking) and astronomical observations scientists have a basic understanding of the present day Martian atmosphere and climate system [see Haberle, 1986; Pollack, 1990]. The

Martian atmosphere is composed primarily of carbon dioxide, CO₂, (approximately 95 percent), has an average surface temperature of 218 (Kelvin), and a typical surface pressure of 7 mb. The acceleration of gravity is 3.72 m/s². In contrast, the Earth's atmosphere is composed primarily of nitrogen (N₂) and oxygen (O₂) (approximately 77 percent and 21 percent, respectively), has an average surface temperature of 288 K, surface pressure of 1000 mb, and an acceleration of gravity of 9.81 m/s².

In spite of such differences in comparison to the Earth, Mars shares some basic meteorological and climatological similarities with the Earth. For both planets the motions which drive the transport processes are driven by the temperature difference between the equator and poles of the planets [Leovy, 1982]. (In addition, the two planets share a common astronomical feature, the rate of planetary rotation, which is important in determining their global wind patterns. One Martian day, known as a sol, consists of 24.6 (Earth) hours.) Because of these common features Haberle [1986] notes that Mars, like Earth, has "a global wind system marked by trade winds in the tropics and cyclonic storms in the mid-latitudes."

Although the two global circulations have some similarities their differences are more striking and of interest to researchers. The Earth's global circulation is characterized by a three-cell system having three distinct cells in each hemisphere (northern and southern). These cells are the Hadley cell, the (thermodynamically indirect) Ferrell cell, and the Polar cell and are present, to varying degrees, in each of Earth's four seasons. Mars on the other hand exhibits a Hadley type and Ferrell type circulation which change size, intensity, and location greatly during the seasons. There is one broad, cross-equatorial Hadley cell during summer and

winter seasons while spring and autumn seasons have two Hadley cells, one in each hemisphere. These contrasts in planetary circulation are due primarily to two differences between Mars and Earth, one physical and one astronomical [Haberle, 1986].

Unlike Earth, Mars has no oceans and as Haberle [1986] notes this has several important consequences. First, on Earth the oceans (which respond slowly to changes in the input of solar energy) moderate the surface temperature and keep the warmest places within the tropical regions year round. Thus, the rising branch of the Hadley circulation remains within the tropical regions as it cycles annually back and forth across the equator. On Mars however, the soil responds quickly to changes in the incoming solar radiation and the warmest surface region (and thus the rising branch of the Hadley cell) closely follows the subsolar point. Thus, on Mars, spring and fall are characterized by two separate Hadley cells, one in each hemisphere, while winter and summer display a single cross-equatorial Hadley cell in which the rising branch is located in the summer hemisphere and the descending branch is found in the winter hemisphere.

The second impact of no oceans is that the latitudinal temperature gradient between equator and pole is much greater on Mars than on Earth. The magnitude of this temperature gradient has an influence on the pressure gradient aloft and thus on the intensity of the jet stream (through the thermal wind relationship). Because Mars has no oceans moderating the latitudinal temperature gradient its winter jet stream may be up to four times stronger than that of Earth.

Mars' orbit is a major astronomical parameter having an influence on the Mars circulation. Haberle [1986] discusses the impacts of the eccentricity of Mars' orbit on its seasons, the most important being the variation in insolation between perihelion and aphelion (approximately 40%) and the duration of the seasons, which all differ from each other significantly. The first of these factors has a strong impact on the intensity of the circulation in a given season.

All of these features of the Martian planet help to create its own unique global circulation/climate system. It is this system that leads to the atmospheric transport characteristics which scientists would like to understand better. Because real data on the Martian circulation/transport processes is limited most research is based on sophisticated computer models. Plumb and Mahlman [1987], speaking of such a model for the Earth, say,

“While the three-dimensional transport model undoubtedly provides the most sophisticated and most precise approach it is still relatively expensive—especially if the chemistry is complex—and demanding in terms of computer facilities and modeling expertise.”

The same is true for GCM and transport models of Mars.

By reducing such models to two or one dimensions many benefits can be derived. Models are smaller and less complex, which reduces the time and cost spent on computing facilities. This dimension reduction can be achieved by several techniques, including averaging (in one or two dimensions) and parameterizing bulk atmospheric processes. Atmospheric mixing is one such process that can be parameterized by use of eddy diffusion coefficients.

This research seeks to accomplish two things in this regard. First, to obtain better values of the eddy diffusion coefficients from sophisticated models already in use at NASA Ames Research Center and second, to obtain a better picture of the basic transport properties of the Mars circulation. This should provide added insight to scientists studying the interacting seasonal cycles of carbon dioxide, water, and dust on Mars [Haberle, 1986; Murphy et al., 1990]. Better estimates of the mixing coefficients will help chemists and photochemists in representing the role of transport in chemical processes in the Martian atmosphere. A primary chemical problem is the basic stability of the CO₂ Mars atmosphere to photodissociation. Transport processes are crucial to the "reformation" of CO₂ [e.g., Kong and McElroy, 1977].

The necessary tools (computers) and procedures for generating better eddy diffusion coefficient values for Mars are available. Eddy diffusion and tracer transport theory and concepts will be presented in chapter 2. Chapter 3 will discuss the computer models, methodology and procedures for calculating the eddy diffusion coefficients from the beginning to the end of an experiment. Chapter 4 will contain the results of this research, followed by a final chapter summarizing the results and drawing conclusions based on the research.

Chapter 2: Eddy Diffusion and Tracer Transport Theory

In this section the theoretical and conceptual background for determining eddy diffusion coefficients will be presented. This will entail a discussion of eddy diffusion theory and tracer transport in an atmosphere. Following this chapter will be a separate chapter discussing the methodology and computer models used to incorporate the theories and calculate the K values.

2.1 Eddy Diffusion

Traditional eddy diffusion theory has been based on a flux-gradient relation analogous to that of molecular diffusion [Plumb and Mahlman, 1987; Lettau, 1951; Houghton, 1986; Sutton, 1953]. The analogy with molecular motion in the kinetic theory of gases

“is given a mechanistic basis in the classical mixing length theory, in which a discrete mass of fluid is supposed to leave some level, bearing the mean property [s] at that level and retaining it for some characteristic vertical distance, before mixing and becoming once again indistinguishable from its mean surroundings [Pasquill and Smith, 1983].”

Further, based on the mixing length theory, eddy diffusion has a characteristic length scale (of turbulent displacement) and a characteristic eddy velocity [Lettau, 1951]. It has been shown that the flux-gradient relation for tracer transport is justified for small-amplitude eddies [Plumb and Mahlman, 1987]. However, Plumb and

Mahlman [1987] also find the relation "to be a practical description of large-scale transport by finite-amplitude eddies."

The derivation of the flux-gradient relation which follows is based on the work of Sutton [1953] who begins with "a fundamental expression for the turbulent flux, independent of any theory of the structure of eddy motion." Sutton's derivation is for a vertical diffusion coefficient and assumes a conservative, transferable entity. For the purposes of this paper the following derivation will be for a vertical diffusion coefficient for a conservative, transferable tracer species X , where X is given as a mass mixing ratio of tracer species to air.

Let u , v , and w be the variables of motion (zonal, meridional, and vertical, respectively) and ρ be the density of the atmosphere. Each variable may now be partitioned into a mean part and an eddy part such as

$$X = \bar{X} + X' \quad (1)$$

where the overbar denotes mean values and the prime denotes eddy quantities (deviations from the mean). Sutton assumes that \bar{X} is constant over any x, y plane and that the motion is such that $\bar{v} = \bar{w} = 0$. (The latter assumption is made because Sutton is only interested in the turbulent (eddy) flux in the derivation of the (mean eddy) flux-gradient relation.)

Using Cartesian coordinates, Sutton's fundamental expression for the turbulent flux is

$$\Phi = k \frac{dX}{dz} - \rho X w' \quad (2)$$

where Φ is the instantaneous (turbulent) flux, $k dX/dz$ is the contribution due to molecular diffusion (k being the appropriate molecular diffusion coefficient and dX/dz the vertical gradient of the tracer species), and $-\rho X w'$ the contribution due to eddy diffusion (that is, the amount of X transported in unit time through unit cross section of a plane parallel to $z = 0$). The negative sign in the eddy flux term indicates that the flux is in the direction of increasing z when X decreases with z .

Expanding equation (2) by using the mean and eddy parts of the instantaneous values gives

$$\bar{\Phi} + \Phi' = k \frac{d}{dz} (\bar{X} + X') - (\bar{\rho} + \rho') (\bar{X} + X') w' \quad (3)$$

Taking the mean of this equation (and noting that the mean of an eddy quantity is zero, i.e. $\bar{\Phi}' = 0$) gives,

$$\bar{\Phi} = k \frac{d\bar{X}}{dz} - \bar{\rho} \overline{w'X'} - \bar{X} \overline{\rho'w'} - \overline{\rho'w'X'} \quad (4)$$

The equation for mean flux can be further simplified by neglecting fluctuations in density. Thus, $\rho' = 0$ and $\bar{\rho} = \rho$.

$$\bar{\Phi} = k \frac{d\bar{X}}{dz} - \rho \overline{w'X'} \quad (5)$$

(This approximation is reasonable for the Martian atmosphere considered in Cartesian coordinates. This approximation is only considered here for the purposes of deriving the flux-gradient relation. In section 2.2 and the remainder of the study log-pressure coordinates will be used and no assumptions about the density will be necessary since, in these coordinates, it is only dependent on height and does not appear explicitly in the remaining derivations/calculations.)

At this point another simplification can be made to the mean flux equation. It is known that for Earth molecular diffusion is the dominant transport process above approximately 100 km, and that below this level eddy diffusion is the dominant process (except in the surface layer) [Levine, 1985; Houghton, 1986]. (As Houghton [1986] explains, this “is because the molecular diffusion coefficient is proportional to the mean free path and hence inversely proportional to density. . .”) Similarly, for Mars, Levine [1985] states that “vertical mixing occurs throughout the Mars atmosphere” and concludes that a good assumption is that eddy diffusion is the dominant vertical mixing process in the middle atmosphere (10–70 km) of Mars. This being the case, the molecular diffusion term can be neglected in the mean flux equation leaving

$$\bar{\Phi} = -\overline{\rho w'X'} \quad (6)$$

The next step (and the basic problem in eddy mixing analysis) is to express equation (6) in terms of the mean tracer quantity \bar{X} and its derivatives. The underlying hypothesis is that (6) can be expressed as the product of a coefficient of mixing and the (vertical) gradient of the mean tracer species. (The physical hypothesis is analogous to that of the kinetic-theory of gases. In the kinetic-theory of gases random molecular motions act to diffuse a tracer constituent down its gradient of distribution. Thus, the analogous physical hypothesis for eddy diffusion is that for large scale turbulence random eddy motions act to transport a tracer constituent down its gradient of distribution.) Letting A be this coefficient gives

$$\bar{\Phi} = -\overline{\rho w'X'} = A \frac{d\bar{X}}{dz} \quad (7)$$

The eddy diffusion coefficient K_z (z indicating the vertical coefficient) is defined by the flux-gradient relation of equation (7) and is given by

$$K_z = \frac{A}{\rho} = -\frac{\overline{w'X'}}{d\overline{X}/dz} \quad (8)$$

This is the flux-gradient relationship which forms the basis for computing eddy diffusion coefficient values. Following the same steps, it is straightforward to obtain a horizontal flux-gradient relationship using this derivation. The actual relationship which will be used to obtain the K values will involve a matrix equation which allows a two-dimensional analysis of the K values. The following section will develop the tracer continuity equation and then make use of a two-dimensional flux-gradient relationship to solve for the eddy transport tensor.

2.2 Tracer Transport

In order to determine eddy diffusion coefficients from the flux-gradient relation, it is necessary to have a tracer distribution (in addition to the atmospheric motions) as seen by equation (8). A tracer is "any quantity that 'labels' fluid parcels" and "may be dynamical or chemical, conservative or nonconservative, passive or active" [Andrews et al., 1987]. The remainder of this section will show how the flux-gradient relation is applied (mathematically) to tracer transport concepts and is based on the work of Andrews et al. [1987] and Plumb and Mahlman [1987].

Consider a continuity equation for a tracer species, X , where X is given as a mixing ratio,

$$\frac{DX}{Dt} = s \quad (9)$$

where s is due to sources and sinks. The net source is a combination of “chemical” production and loss terms (e.g., for water, evaporation and condensation; for dust, sedimentation) and “the effects of turbulent diffusion by the unresolved scales of motion.” In addition, for Mars, s may have a sink/source term due to the condensation flow in the Martian atmosphere. (This condensation flow is a result of the nature of CO_2 which condenses in the high latitudes of the winter hemisphere where temperatures drop to 150 K. This condensation causes the atmospheric pressure to drop over the winter polar cap which in turn drives a strong planetwide circulation that transports mass, momentum, and heat toward the growing polar cap. Model simulations have shown that the condensation flow has little effect on the simulated zonal mean flow and that its primary influence is on the strength of the polar cap surface winds.) Thus, s may be represented as follows,

$$s = \sum (\text{Prod} + \text{Loss})_{chem} + \text{unresolved scales of turbulent diffusion} \quad (10)$$

+ condensation flow term

Because of the inability to effectively resolve all scales of turbulent motion Andrews et al. [1987] note that “tracers are never exactly conserved in observational analysis of atmospheric data. However, if the resolved scales include most of the tracer variance, the diffusive source can in many cases be neglected.” (This assumption is made in this study but it must be noted that the Mars GCM does have some regions of significant mixing due to local convection at both the lowest and highest model levels. Thus, the calculations for the eddy diffusion coefficients will actually represent a lower bound on their values.)

Two further simplifications are also used in this study. First, the tracer is chemically inert and thus there are no chemical production or loss terms. Second,

it is assumed that there is no loss of tracer due to the condensation flow. (The condensation flow has been turned off in the transport model for these experiments.) Thus, the tracer has no chemical sources or sinks and no loss due to condensation flow and the tracer continuity equation becomes,

$$\frac{DX}{Dt} = 0 \quad (11)$$

After expanding the material derivative on the left hand side of (11), separating the dependent variables into mean and eddy parts, and zonally averaging equation (11), the tracer budget equation becomes, in the "local Cartesian" form of spherical coordinates,

$$\frac{\partial \bar{X}}{\partial t} + \bar{v} \frac{\partial \bar{X}}{\partial y} + \bar{w} \frac{\partial \bar{X}}{\partial z} = -\frac{1}{p} \nabla \cdot \vec{F} \quad (12)$$

where p is pressure and z is the vertical log-pressure coordinate given as

$$z = -H \ln \left[\frac{p}{p_s} \right] \quad (13)$$

where H is a constant scale height and p_s is a (globally-averaged) reference surface pressure (both are calculated from the model data for the individual data sets).

Furthermore,

$$\vec{F} = (F_y, F_z) = (p \overline{v'X'}, p \overline{w'X'}) \quad (14)$$

is the eddy flux (in units of g/s^3), where the prime denotes eddy quantities (deviations from the zonal means). (The flux is in units of g/s^3 because pressure was used in place of density in the form of the continuity equation used to derive equation (12).) The flux divergence is,

$$\vec{\nabla} \cdot \vec{F} = \frac{1}{\cos \phi} \frac{\partial}{\partial y} (\cos \phi F_y) + \frac{\partial F_z}{\partial z} \quad (15)$$

where ϕ is latitude.

Following Plumb and Mahlman [1987] a zonally-averaged closure of equation (12) is obtained by parameterizing the eddy flux in terms of zonally averaged quantities. This is done by using the flux-gradient relationship of the previous section and applying it in the following form

$$(F_y, F_z) = -p[K] \cdot \nabla \bar{X} \quad (16)$$

where the transport tensor is,

$$[K] = \begin{bmatrix} K_{yy} & K_{yz} \\ K_{zy} & K_{zz} \end{bmatrix} \quad (17)$$

Plumb [1979] and Matsuno [1980] have shown that this flux-gradient relation is justified for the case of small amplitude (but otherwise general) eddy motions on a purely zonal flow. In addition, the results of the Plumb and Mahlman [1987] study show that the relation is still relevant even when the small amplitude eddy assumption is not satisfied. (They found that when their calculated K values (for Earth were used in a 2-D model, the model was able to reproduce well the zonally averaged evolution of the tracer species.) Substituting (14) and (17) into (16) and rearranging yields the following set of equations,

$$K_{yy} \frac{\partial \bar{X}}{\partial y} + K_{yz} \frac{\partial \bar{X}}{\partial z} = -\overline{v'X'} \quad (18)$$

$$K_{zy} \frac{\partial \bar{X}}{\partial y} + K_{zz} \frac{\partial \bar{X}}{\partial z} = -\overline{w'X'} \quad (19)$$

Using computer generated data one may obtain the mean tracer gradients and the eddy tracer fluxes and solve for the unknown eddy diffusion coefficients.

However, (18) and (19) form a system of two equations in four unknown variables. It is therefore necessary to use two differing sets of GCM/transport data to yield a set of four equations with four unknowns, as given below. (That is, two transport simulations are associated with each GCM simulation. By using two different initial tracer distributions (one horizontally stratified and the other vertically stratified) with the same dynamics data from the GCM a closed set of equations for the four unknown coefficients is obtained. A 1 indicates data set 1 (the horizontally stratified case) while a 2 indicates data set 2 (the vertically stratified case).)

$$K_{yy} \left(\frac{\partial \bar{X}}{\partial y} \right)_1 + K_{yz} \left(\frac{\partial \bar{X}}{\partial z} \right)_1 = -(\overline{v'X'})_1 \quad (20)$$

$$K_{zy} \left(\frac{\partial \bar{X}}{\partial y} \right)_1 + K_{zz} \left(\frac{\partial \bar{X}}{\partial z} \right)_1 = -(\overline{w'X'})_1 \quad (21)$$

$$K_{yy} \left(\frac{\partial \bar{X}}{\partial y} \right)_2 + K_{yz} \left(\frac{\partial \bar{X}}{\partial z} \right)_2 = -(\overline{v'X'})_2 \quad (22)$$

$$K_{zy} \left(\frac{\partial \bar{X}}{\partial y} \right)_2 + K_{zz} \left(\frac{\partial \bar{X}}{\partial z} \right)_2 = -(\overline{w'X'})_2 \quad (23)$$

It is now straightforward to solve for the K values using matrix algebra. However, the possibility for trouble in calculating the coefficients does exist in the case where the mean concentration gradient(s) of the tracer(s) is (are) zero, near-zero or where the mean gradients of the two tracers become parallel. This situation can be avoided by incorporating weak source/sink terms for the tracer(s) [Plumb and Mahlman, 1987] in the aerosol model. (None of these problems was encountered in this study.) Before proceeding into a discussion of the computer models and procedure for obtaining the K values, a more detailed discussion of the K tensor and atmospheric circulation is presented.

2.3 The K Tensor

Plumb and Mahlman [1987] (following the work of Plumb [1979] and Matsuno [1980]) have shown that the transport tensor [K] may be regarded as comprised of two parts

$$[K] = [L] + [D] \quad (24)$$

where [L] and [D] are respectively antisymmetric and symmetric tensors whose components may be expressed in terms of the parcel displacement (ξ, η, ζ) defined in the generalized Lagrangian-mean theory of Andrews and McIntyre [1978].

Specifically

$$[L] = \begin{bmatrix} 0 & \frac{1}{2}(\overline{v'\zeta} - \overline{w'\eta}) \\ \frac{1}{2}(\overline{w'\eta} - \overline{v'\zeta}) & 0 \end{bmatrix} \quad (25)$$

and, for a conserved tracer ($s = 0$),

$$[D] = \begin{bmatrix} \frac{\partial}{\partial t} \left(\frac{1}{2} \overline{\eta^2} \right) & \frac{\partial}{\partial t} \left(\frac{1}{2} \overline{\eta\zeta} \right) \\ \frac{\partial}{\partial t} \left(\frac{1}{2} \overline{\eta\zeta} \right) & \frac{\partial}{\partial t} \left(\frac{1}{2} \overline{\zeta^2} \right) \end{bmatrix} \quad (26)$$

If X were not conserved as it is in this study it would be necessary to add terms to [D] to account for the roles of any sources and/or sinks.

The components of [L] and [D] can be calculated once the components of [K] are known. It is straightforward to show the following:

$$[L] = \begin{bmatrix} 0 & \frac{1}{2}(K_{yz} - K_{zy}) \\ \frac{1}{2}(K_{zy} - K_{yz}) & 0 \end{bmatrix} \quad (27)$$

and

$$[D] = \begin{bmatrix} K_{yy} & \frac{1}{2}(K_{yz} + K_{zy}) \\ \frac{1}{2}(K_{yz} + K_{zy}) & K_{zz} \end{bmatrix} \quad (28)$$

For the case of a conserved tracer the components of [D] represent diffusive transport due to dispersion of air parcels. Although this study does not consider

the case of a nonconservative tracer it is of interest to note the consequences of such a case. As previously mentioned this case would add additional term(s) to (26). The additional nonconservative contribution would effectively add a component representing a relaxation rate to the terms in [D]. This relaxation rate would obviously differ for different constituents and thus so would the transport coefficients. This leads Plumb and Mahlman [1987] to conclude that

“this apparently undermines any attempt to derive a universal parameterization of eddy transport . . . Any hope of recovering a universal transport parameterization hinges on the diffusion being dominated by kinematic dispersion.”

The antisymmetric tensor [L] is the component of [K] representing the advective contribution to the eddy transport. Clark and Rogers [1978] have shown that for the case of a conservative tracer the eddy flux due to the advective portion is directed normal to the \bar{X} gradient. The diffusive contribution to [K] is not necessarily directed parallel to the \bar{X} gradient. However, following Plumb and Mahlman [1987] and using the symmetry of the diffusive tensor, [D]

“can be made purely diagonal via a local coordinate rotation to its principal axes. If we rotate the coordinates through an angle α where

$$\tan 2\alpha = \frac{2D_{yz}}{D_{yy} - D_{zz}} \quad (29)$$

then, in the new coordinates,

$$[D'] = \begin{bmatrix} D'_{yy} & 0 \\ 0 & D'_{zz} \end{bmatrix} \quad (30)$$

where

$$D'_{yy} = \cos^2 \alpha D_{yy} + \sin^2 \alpha D_{zz} + 2 \sin \alpha \cos \alpha D_{yz} \quad (31)$$

$$D'_{zz} = \sin^2 \alpha D_{yy} + \cos^2 \alpha D_{zz} - 2 \sin \alpha \cos \alpha D_{yz} \quad (32)$$

Provided $D_{yy} \geq 0$, $D_{zz} \geq 0$ and $D_{yz}^2 \leq D_{yy}D_{zz}$, then $D'_{yy} \geq 0$ and $D'_{zz} \geq 0$ and the component of the eddy flux associated with [D] is purely diffusive (Matsuno, 1980)."

Using (28), equations (29), (31) and (32) may be written in terms of the computed eddy coefficients as

$$\tan 2\alpha = \frac{K_{yz} + K_{zy}}{K_{yy} - K_{zz}} \quad (33)$$

$$D'_{yy} = \cos^2 \alpha K_{yy} + \sin^2 \alpha K_{zz} + 2 \sin \alpha \cos \alpha \frac{1}{2}(K_{yz} + K_{zy}) \quad (34)$$

and

$$D'_{zz} = \sin^2 \alpha K_{yy} + \cos^2 \alpha K_{zz} - 2 \sin \alpha \cos \alpha \frac{1}{2}(K_{yz} + K_{zy}) \quad (35)$$

where the conditions for a purely diffusive tensor are now $K_{yy} \geq 0$, $K_{zz} \geq 0$ and $\frac{1}{4}(K_{yz} + K_{zy})^2 \leq K_{yy}K_{zz}$.

This section has shown that the eddy transport tensor [K], which is actually a function of Lagrangian statistics, can be represented as the sum of a diffusive tensor [D] and an advective tensor [L] and may be estimated using the flux-gradient relation and Eulerian statistics. It has also shown that [D] can be made a purely diffusive transport tensor via a local coordinate rotation and that the eddy flux contribution due to [L] is directed normal to the \bar{X} gradient. In addition, the components of [D] and [L] may be easily calculated from the components of [K].

2.4 The Mean Meridional Circulation

This section follows the procedures of Plumb and Mahlman [1987] in order to obtain the mean meridional circulation in terms of a stream function, Ψ , and an effective transport circulation in terms of a stream function, Ψ_T .

Using the continuity equation

$$\frac{1}{\cos \phi} \frac{\partial(p\bar{v} \cos \phi)}{\partial y} + \frac{\partial(p\bar{w})}{\partial z} = 0 \quad (36)$$

the mean meridional stream function may be written as

$$p\bar{v} = -\frac{\partial(p\Psi)}{\partial z}; \quad \bar{w} = \frac{1}{\cos \phi} \frac{\partial(\Psi \cos \phi)}{\partial y} \quad (37)$$

Ψ may be obtained by integrating the first part of (37) vertically using the \bar{v} values computed from GCM data and assuming that $\Psi = 0$ when $p = 0$ (or when z corresponds to the top of the model) or by integrating numerically in latitude using the \bar{w} values with the conditions that $\Psi = 0$ at both poles for all z .

By using (24) in (16), (12) may be written in the following form

$$\frac{\partial\bar{X}}{\partial t} + V_T \frac{\partial\bar{X}}{\partial y} + W_T \frac{\partial\bar{X}}{\partial z} = \frac{1}{p} \nabla \cdot (p[D] \cdot \nabla\bar{X}) \quad (38)$$

where $\vec{U}_T = (V_T, W_T)$ is an effective transport circulation defined by

$$V_T = -\frac{1}{p} \frac{\partial(p\Psi_T)}{\partial z}; \quad W_T = \frac{1}{\cos \phi} \frac{\partial(\Psi_T \cos \phi)}{\partial y} \quad (39)$$

where Ψ_T is given by

$$\Psi_T = \Psi - \frac{1}{2} (\overline{v'\zeta} - \overline{w'\eta}) \quad (40)$$

Using (25) and (27) the transport stream function may be written as

$$\Psi_T = \Psi + \frac{1}{2} (K_{zy} - K_{yz}) \quad (41)$$

and may be computed once Ψ has been determined (as noted above) and the K values have been calculated. Once Ψ_T is known the transport velocity of (39) may also be computed. More directly,

$$V_T = \bar{v} - \frac{1}{p} \frac{\partial}{\partial z} \left\{ \frac{1}{2} p (K_{zy} - K_{yz}) \right\} \quad (42)$$

and

$$W_T = \bar{w} + \frac{1}{\cos \phi} \frac{\partial}{\partial y} \left\{ \frac{1}{2} \cos \phi (K_{zy} - K_{yz}) \right\} \quad (43)$$

Plumb and Mahlman demonstrate that the effective transport velocity, \vec{U}_T , is in general not the same as the Lagrangian-mean velocity \bar{u}^L (which follows the center of mass of the tracer distribution) of Andrews and McIntyre [1978]. The difference arises due to the nature of [D], the diffusive tensor. Fig. 1 (reproduced from Plumb and Mahlman [1987]) shows an initial distribution of \bar{X} located at a reference point A (which also locates the center of mass of the mean tracer distribution). After some short time δt , the distribution of \bar{X} occupies the stippled region. A new reference point B may be located using the effective transport velocity scheme of (38). The location of B relative to A is now given by $\vec{U}_T \delta t$. Now, if [D] is spatially inhomogeneous there will be a nonuniform diffusion of tracer about the point B as shown in Fig. 1. Since the \bar{X} distribution is no longer uniform about the reference point the center of mass no longer coincides with it but is now located at point C whose position relative to A is $\bar{u}^L \delta t$. Thus, one sees that in general $\bar{u}^L \neq \vec{U}_T$ and the two will only be equal when the diffusion is spatially homogenous.

Plumb and Mahlman believe this transport circulation to be identical to the "advective mass flux" identified by Kida [1983]. Kida speaks of this "advective mass flux" "as a basic flow of air mass on which diffusion of air parcels is superimposed." As noted above this mean movement of parcels is not necessarily identical to the Lagrangian-mean motion since diffusion is not taken into account but superimposed on the basic advective motion.

This section has developed the ideas of Plumb and Mahlman [1987] for looking at a zonal mean meridional circulation and an effective transport circulation for the Martian atmosphere. These can be computed from the GCM wind data and the K values calculated in this study. Plots of these circulations may provide further insight to the transport characteristics of the Martian atmosphere.

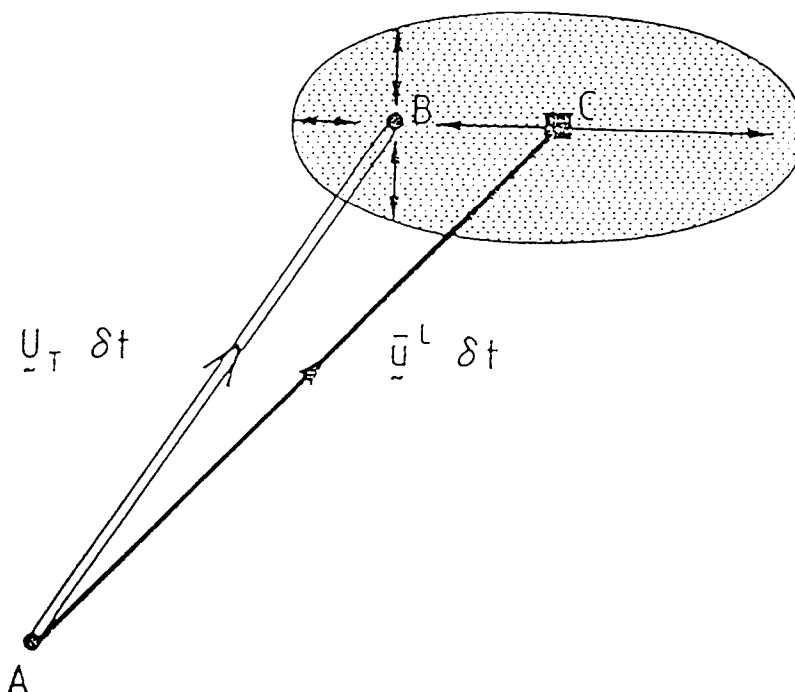


Fig. 1 Illustrating the difference between the transport circulation \underline{U}_T and Lagrangian mean circulation \bar{u}^L in the presence of inhomogeneous diffusion. The reference point B moves with the transport circulation; the center of mass C moves with the Lagrangian mean velocity. If the diffusion about B is inhomogeneous, C moves relative to B and therefore the two velocities differ under such circumstances. [Reproduced from Plumb and Mahlman, 1987.]

Chapter 3: Methodology and Procedures

An experiment to derive a set of eddy diffusion coefficients consists of two sets of GCM/transport data, in order that all 4 coefficients can be determined. Each experiment is for a particular set of meteorological conditions. Experiment 1 is a vernal equinox case with no dust loading in the atmosphere. Experiment 2 is a Northern Hemisphere winter case with no dust loading. Experiment 3 is the same as Experiment 2 but with a dust loading giving a visible optical depth of $\tau=1$. To get the two sets of data needed to compute all four K values, each experiment consists of two transport model runs using the same GCM data (so that the dynamics remain the same) but different initial tracer distributions. In each experiment tracer distribution 1 is purely horizontally stratified and tracer distribution 2 is purely vertically stratified at time equal to zero. The aerosol transport model is run to simulate 10 sols of atmospheric transport. (A sol is one Martian day.)

After the data sets for each experiment were generated they were stored and sent to Oregon State University for the remainder of the computations. The data were input to a series of computer programs which performed a coordinate transformation, calculated K values, and produced plots of various features of the Martian circulation. This section will discuss the models (the Mars GCM and the aerosol transport model) used to generate the needed data for calculating the K values as well as the steps followed to compute them.

3.1 The Mars GCM

The process began by running the Mars GCM at NASA Ames Research Center to obtain the dynamical data for a ten-sol transport simulation. The general circulation model includes wind speeds, surface pressure and temperature as part of its output. The data was output every nine simulated Martian minutes (or 160 times per sol) for a total of 40 sols and stored on a history tape. I was given the data once every twenty time steps (for the last 10 sols of the 40 sol simulation) so there were eight time steps (in three hour increments) per sol.

The Mars GCM is a general circulation model which was created by modifying an Earth GCM developed at the University of California, Los Angeles (UCLA), by Y. Mintz and A. Arakawa. Pollack et al. [1990] have made various modifications over the past few years in order to adapt the model to conditions on Mars. The remainder of this section will provide a limited description of the model configuration and physical processes. For a more thorough description the reader is referred to Pollack et al. [1990] and Haberle et al. [1993].

“The NASA Ames Mars GCM is a finite difference model based on the primitive equations of meteorology cast in spherical sigma coordinates [Haberle et al., 1993].” The horizontal grid resolution is 7.5° in latitude by 9.0° in longitude while the vertical spacing is gridded in thirteen layers from the surface to a height of approximately 47 km. The layers increase in thickness from about 500 m at the surface to 5 km at the top of the model. This gives a $40 \times 24 \times 13$ point grid for the winds.

The recent improvements made by Pollack et al. [1990]

“include incorporating the radiative effects of atmospheric dust, improving the treatment of the radiative effects of carbon dioxide gas, allowing for the condensation of carbon dioxide in the atmosphere, permitting the use of an arbitrary number of vertical layers of arbitrary thickness, using improved parameterizations for subgrid scale processes, incorporating spatially varying thermal inertia and surface albedo, and using an improved data set for the large-scale topography.”

Of these, the radiative effects of dust and CO₂, the treatment of CO₂, and the improved topography set are the most important.

The topography was improved with data from the Mars Consortium and is important in modeling and understanding the low-level mean circulation over a large portion of the planet. The primary physical process of concern was the role of dust in the Martian atmosphere, especially during times of intense dust loadings. Dust has a very strong influence on the radiative processes in the Martian atmosphere which ultimately affect the winds thereby influencing the circulation and transport. Haberle et al. [1993] run a series of experiments to observe the effects of various dust loadings on the general circulation of Mars. These show a general deepening and strong intensification of the mean circulation.

The dust has an impact on atmospheric emissivity and temperature thereby influencing the behavior of CO₂ phase changes, both in the atmosphere and on the surface. The carbon dioxide condensation flow considered by itself has little impact on the mean circulation except for determining the intensity of surface winds at the polar caps [Haberle et al., 1993]. However, the condensation flow could have an impact on this study if the CO₂ were allowed to remove the tracer species from

the atmosphere as it condenses. For the purposes of this study the condensation flow has been turned off in the transport model.

After implementing the improvements to the Mars GCM, Pollack et al. [1990] “verified the fidelity of this new code” through various experiments while Haberle et al. [1993] analyzed experiments and found good agreement with existing data from spacecraft. However, Haberle cautions that the “models can be validated only in a very limited sense and that we must not become too confident of their predictions” since the available Mars data is temporally and spatially sparse. Some further limitations of the Mars GCM include the coarse horizontal grid resolution (which may miss features of the true circulation) and the handling of dust particles which are fixed in space and time and are not transported by the winds. In addition, the treatment of CO₂ could be more explicit both radiatively and dynamically. The radiative properties of CO₂ ice clouds are not modeled nor are the effects of ice particle growth and removal.

The last 10 sols of output from each run of the GCM was stored and then used as the dynamical input to the transport model. In addition, an initial tracer distribution must be specified as input (both the spatial distribution as well as a particle size distribution). The aerosol transport model is the focus of the next subsection.

3.2 The Aerosol Transport Model

The transport model used for this study was developed by O. B. Toon and others and is documented in a paper by Toon et al., [1988]. It models the physics

and chemistry of aerosols and gases using as input the data from dynamical models such as the Mars GCM. The output is the mixing ratio of the tracer species as it mixes throughout the atmosphere.

The transport model is based on a generalized form of the tracer continuity equation,

$$\begin{aligned} \frac{\partial C}{\partial t} + \frac{\partial UC}{\partial X_1} + \frac{\partial VC}{\partial X_2} + \frac{\partial WC}{\partial X_3} - \frac{\partial \rho^*}{\partial X_1} K_1 \frac{\partial C/\rho^*}{\partial X_1} \\ - \frac{\partial \rho^*}{\partial X_2} K_2 \frac{\partial C/\rho^*}{\partial X_2} - \frac{\partial \rho^*}{\partial X_3} K_3 \frac{\partial C/\rho^*}{\partial X_3} \end{aligned} \quad (44)$$

$$= (P - L)V_m H_{m1} H_{m2}$$

This is equation (1) from Toon et al., [1988] and is

“the flux form of the continuity equation for the tracer concentration C , at time t , being advected by scaled winds U , V and W , mixed by scaled diffusion coefficients K_1 , K_2 and K_3 , in an atmosphere with scaled density ρ^* , scaled coordinates X_1 , X_2 and X_3 , and with production rates P and loss rates L .”

The terms V_m , H_{m1} and H_{m2} are scaling factors which appear implicitly in the dependent variables and allow the model to be run for a variety of coordinate systems by choosing the appropriate scaling factors for a given system.

Toon et al. replace (44) with three one-dimensional equations (two horizontal and one vertical) and use a time-splitting technique in order to facilitate the computational processes and reduce the computer time required to solve (44). In dealing with the horizontal advection they apply “a Galerkin technique with chapeau functions as finite elements, and a Crank-Nicolson time step (Pepper et al. 1979; Chock and Dunker 1983; Carmichael et al. 1980, 1986).” This technique results in less memory requirements, computationally stable forms of the advection equations, and code which exactly conserves mass and saves computer time. They also use a

smoothing scheme to handle negative mixing ratios which may occur as the result of "noise" generated in the presence of large concentration gradients.

Vertical transport is treated differently than the horizontal transport. Because diffusion is often the dominant method of transport in the vertical and numerical diffusion can be a problem in the presence of large oscillating vertical velocities the coupled advective-diffusive equation is precisely solved. By removing numerical diffusion (from the upstream advection) the treatment of advection is accurate and large artificial diffusion (due to the oscillating vertical velocities) is avoided. (For this study the diffusion coefficients in the model have been set to zero so that the values computed here are not based on a previously assumed set of values. However, the smoothing algorithm for (the few) instances when negative concentrations occur does invoke some diffusion coefficients in order to model the mixing necessary to correct these situations.) In addition, many of the chemical and microphysical processes of aerosols and gases are linked to vertical transport. The authors checked their coupled algorithms (horizontal and vertical) against analytic test cases and found that

"advection is treated very accurately even when sharp gradients occur, diffusion is treated accurately, and advective-diffusive equilibrium is treated without error. The expressions exactly conserve mass and the fluxes are easily identified for diagnostic purposes. . . negative concentrations never occur. . . and numerical stability is guaranteed."

Aerosol microphysical processes are treated in the model by using a linearized form of the production and loss terms in equation (44). The aerosols have specified size ranges and are classed into four types based on composition. The first type

is allowed to grow by coagulation only, the second by condensational growth, the third by coagulation and condensation, and the fourth type is the volume fraction of the third type which is composed of the first type. The code handling the microphysical processes is also written to conserve mass as well as particle number and has proved adequate in testing.

The transport model is capable of simulating transport "with advection, diffusion, sedimentation, coagulation, rainout, surface deposition, and transport across the lateral boundaries all occurring in a temporally varying wind field" with a negligible loss of mass [Toon et al., 1988]. However, for this study the model was run under greatly simplified conditions. Basically, all microphysical/chemical processes were turned off, as was the convective mixing and condensation deposition/removal. Thus, the transport is solely that by the resolved winds produced by the GCM—there is no subgrid scale mixing in these transport simulations, and the transport is conservative.

The tracer mixing ratio output from the transport model was stored on tape and then transferred along with the GCM dynamical data to the Atmospheric Science Computers at Oregon State University where the remainder of this research was performed.

3.3 Computation of K values

The data were input to several computer programs in order to calculate the K values and to generate plots to look at transport features and circulation characteristics of the Martian atmosphere. First, the pressure associated with each

grid point was calculated and then the transport model output (tracer mixing ratios) and the GCM dynamical data were converted to convenient units. (Mixing ratios are now in grams of tracer per kilogram of CO₂, horizontal wind speeds in meters per second, vertical wind speeds in centimeters per second, and all pressure fields in millibars.) Next, all the data had to be converted from the sigma coordinate system used by the NASA models to a log-pressure coordinate system so that the calculated eddy diffusion coefficients would have meaningful units and be more accessible to other scientists.

The initial step was to transform the data from the thirteen sigma levels of the GCM's vertical grid to a grid of thirteen constant pressure levels. (These constant pressure levels are not equally spaced by virtue of the choices of the sigma levels.) In the Mars GCM the relation between the sigma coordinate and pressure is given by

$$\sigma = \frac{p - p_t}{p_s - p_t} \quad (45)$$

where p is the pressure at a point, p_s is the surface pressure below the point, and p_t is a constant. This constant is defined to be the pressure at the top of the model and has been assigned a value of 0.06699 mb. The thirteen "standard" pressure levels were then obtained by solving (45) for p , using a global and time averaged surface pressure for p_s , and substituting the given sigma level values for σ , as shown by the following equation.

$$p_i = \sigma_i \times (\bar{p}_s - p_t) + p_t \quad (46)$$

where $i = 1, 2, \dots, 13$. Following this the data were transformed to the pressure levels using a log-linear interpolation. This was readily done because the pressure

at each grid point had been previously calculated. The log-linear interpolation was performed (using the mixing ratio X for example) according to the following equation.

$$X_{p_i} = \frac{(X_{p_2} - X_{p_1})}{(\ln(p_2) - \ln(p_1))} \times (\ln(p_i) - \ln(p_2)) + X_2 \quad (47)$$

where the constant pressure level p_i lies between p_1 and p_2 .

The final step in transforming the coordinate system was to interpolate from the thirteen "standard" pressure levels to an evenly spaced log-pressure vertical coordinate, z , as defined by equation (48). This was accomplished by converting the thirteen uneven pressure levels to uneven log-pressure levels using equation (48). Again, the global and time averaged surface pressure for the data set was used for p_s . Thus, the new uneven z coordinates were given by

$$z_i = -H \ln \left(\frac{p_i}{p_s} \right) \quad (48)$$

where $i = 1, 2, \dots, 13$. Then the even z -scale was chosen by looking at the limits of the uneven scale (z_1 and z_2) and choosing whole numbers near these and then dividing the difference between them by twelve. This gave an increment which created thirteen evenly spaced log-pressure levels for the z -coordinate. Instead of using another linear interpolation scheme to transform the data to the new coordinate system a cubic spline routine was utilized.

Once all of the data were converted to the log-pressure coordinates several computer programs performed the necessary calculations to obtain the terms necessary to solve for the eddy diffusion coefficients in equations (20) thru (23). These programs calculated the mean mixing ratio gradients $\frac{\partial \bar{X}}{\partial y}$ and $\frac{\partial \bar{X}}{\partial z}$ as well as the mean eddy flux quantities $\overline{v'X'}$ and $\overline{w'X'}$ for each time step. This was accomplished by

first zonally-averaging each of the necessary variables (winds and mixing ratios) for each time step. It should be noted that some of the zonal averages calculated at the lower levels of the atmosphere are not true zonal averages. This is due to the very large nature of the Martian topography in certain areas, particularly near the equator, and the nature of the initial transformation between sigma coordinates and the constant pressure levels. The high regions (up to ~ 10 km) of the Martian planet have low surface pressures. Thus when the constant pressure levels were calculated using a global average surface pressure some of these levels would have pressures larger than the actual surface pressures in regions of high topography. This created a situation in which data values would have to be extrapolated to grid points that were below the ground (often far below the ground). To avoid this problem all such points were flagged and ignored in future calculations. So, in some instances the zonal averages are not based on an average of 40 zonal data points, but substantially fewer. Extrapolations (and thus missing points) were necessary for the lowest five levels of the atmosphere, with approximately 50% of the points extrapolated (missing) at the lowest level (1) and 1% at the fifth level.

After the zonal averages were calculated for each time step the eddy values v' , w' , and X' were calculated by subtracting the zonal mean from the instantaneous values,

$$v' = v - \bar{v} \quad (49)$$

$$w' = w - \bar{w} \quad (50)$$

$$X' = X - \bar{X} \quad (51)$$

(Again, these only represent the large scale resolved eddies from breaking transient and standing waves as well as those resulting from the thermal tides.) The mean eddy flux quantities were obtained by multiplying the eddy winds by the eddy tracer mixing ratios and zonally averaging (again ignoring below-ground points).

The gradients of the mean tracer fields were calculated using finite-differencing techniques. At the boundaries one-sided finite-differencing was used, while a centered finite-differencing approach was used for grid points with an adjacent point on both sides.

To obtain the K values the eddy flux quantities and the mixing ratio gradients were time-averaged and then the two-dimensional flux-gradient relation was solved (as opposed to obtaining the K values for each time step and then time-averaging). This method was chosen since the necessary conditions for the flux-gradient relation to be satisfied (small-amplitude eddies on a purely zonal flow) are not met. Because these conditions are not satisfied one cannot expect an instantaneous look at the K's to be very accurate. What one hopes is that in a statistical time-average sense the flux-gradient relation will still provide an adequate description of eddy transport and an appropriate set of K's. Thus, I chose to time-average the components needed to solve for the K values and then obtain them.

Chapter 4: Results

In this chapter I look at the results of the three experiments. I examine the time-averaged, zonal-mean winds, the time evolution of the mean tracer fields, the time-averaged mean eddy fluxes and mean tracer fields, the mean meridional and transport circulations, and the distribution of the calculated mixing coefficients. Following these results will be a separate section discussing the time scales associated with the overturning of the atmospheric circulation by the mean meridional circulation and by vertical mixing.

4.1 Experiment 1: Northern Spring Equinox

The equinox case spans $L_s = 356^\circ$ – 358° and is for an optical depth of $\tau = 0$. (L_s is an angular measure of the planet's orbital position. $L_s = 0^\circ$ corresponds to northern spring equinox; $L_s = 90^\circ$, 180° , and 270° correspond to northern summer solstice, fall equinox, and winter solstice, respectively. τ is the visible dust opacity.) Mars GCM experiments generally begin from a resting state and are run for 50 sols; the code allows for the advancement of the planet along its orbit according to Kepler's laws. Because the radiative relaxation time of the Martian atmosphere is short (2–4 sols) the circulation spins up quickly and it is expected that averaging the last 30 sols of each simulation should produce results similar to steady state values which is the case [Haberle et al., 1993]. For this study all three GCM simulations were run for 40 sols. The first 30 sols allowed sufficient time

for spin up of the circulation and the last 10 sols of the GCM runs were used to run 10 sol transport simulations using the aerosol model.

Figs. 2–4 show the zonal-mean circulation for the equinox case. There is good agreement with the results of Haberle et al. [1993] who used the same GCM to look at various seasonal circulation patterns. The zonal, meridional, and vertical winds exhibit the same general structure and magnitude as those in the aforementioned study. This adds to the confidence that a 10-day time average is representative of zonal-mean conditions near spring equinox.

The mean zonal winds are characterized by predominately westerly winds throughout both hemispheres with similar magnitudes (up to 45 m/s), while there exist two pockets of weak easterlies in the tropical latitudes and extending from the ground to 15 km and from about 25 km to the top of the model. There is also a thin band of easterlies found at the North pole. This symmetrical structure of the zonal-mean circulation about the equator is a feature of both equinoxes [Haberle et al., 1993].

The mean meridional winds are strongest at low levels corresponding to the low level branches of a two-cell Hadley circulation system (see Fig. 15). A strong southerly flow ($\sim 2\text{m/s}$) from the southern hemisphere meets a strong northerly flow ($\sim 2\text{m/s}$) from the northern hemisphere at about 15S where the rising branches of the Hadley cells are found. Above the strong low level winds the meridional motions are directed poleward in each hemisphere with the northern hemisphere showing stronger winds. These winds correspond to the upper level, poleward flow of the Hadley cell system.

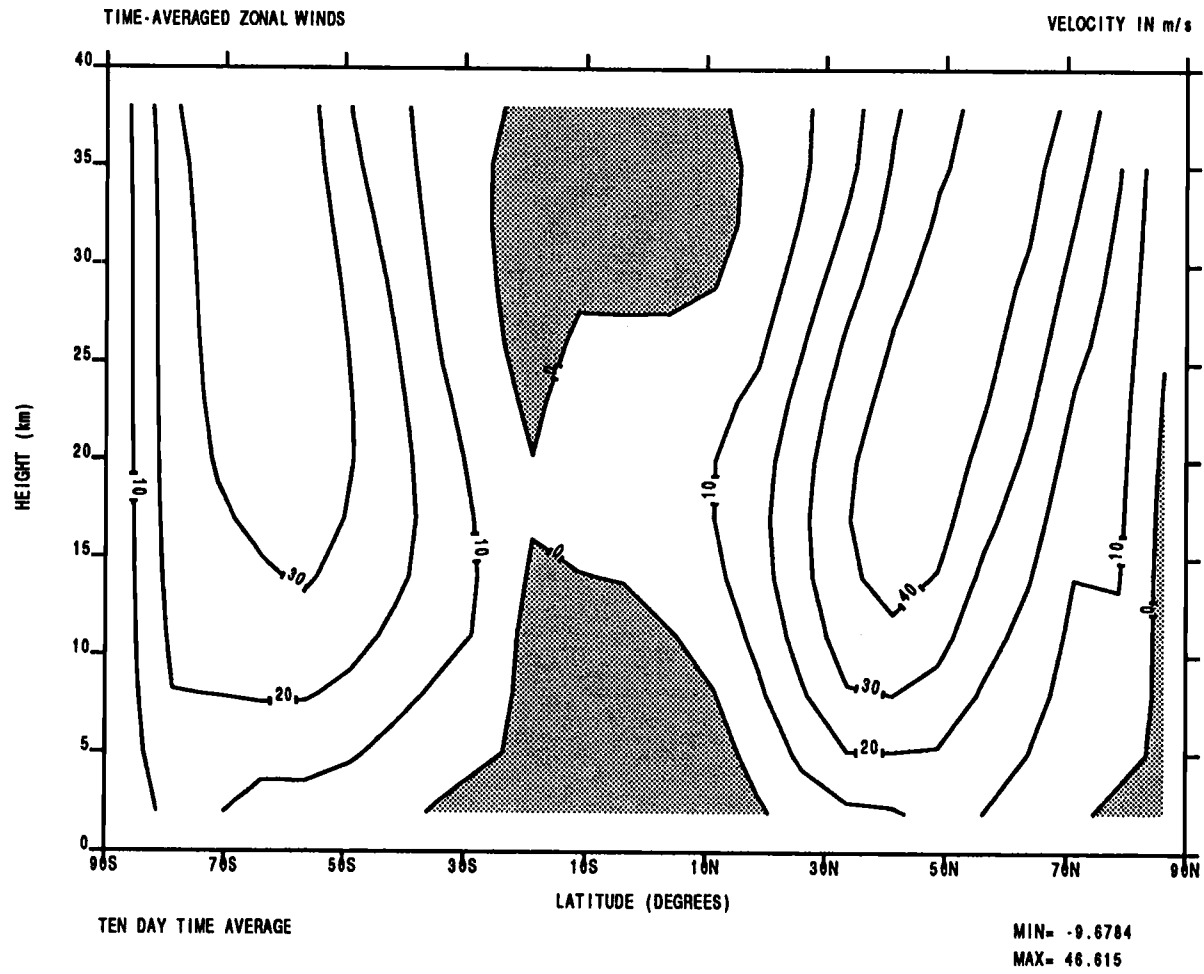


Fig. 2 Time-averaged mean zonal winds for Spring equinox.

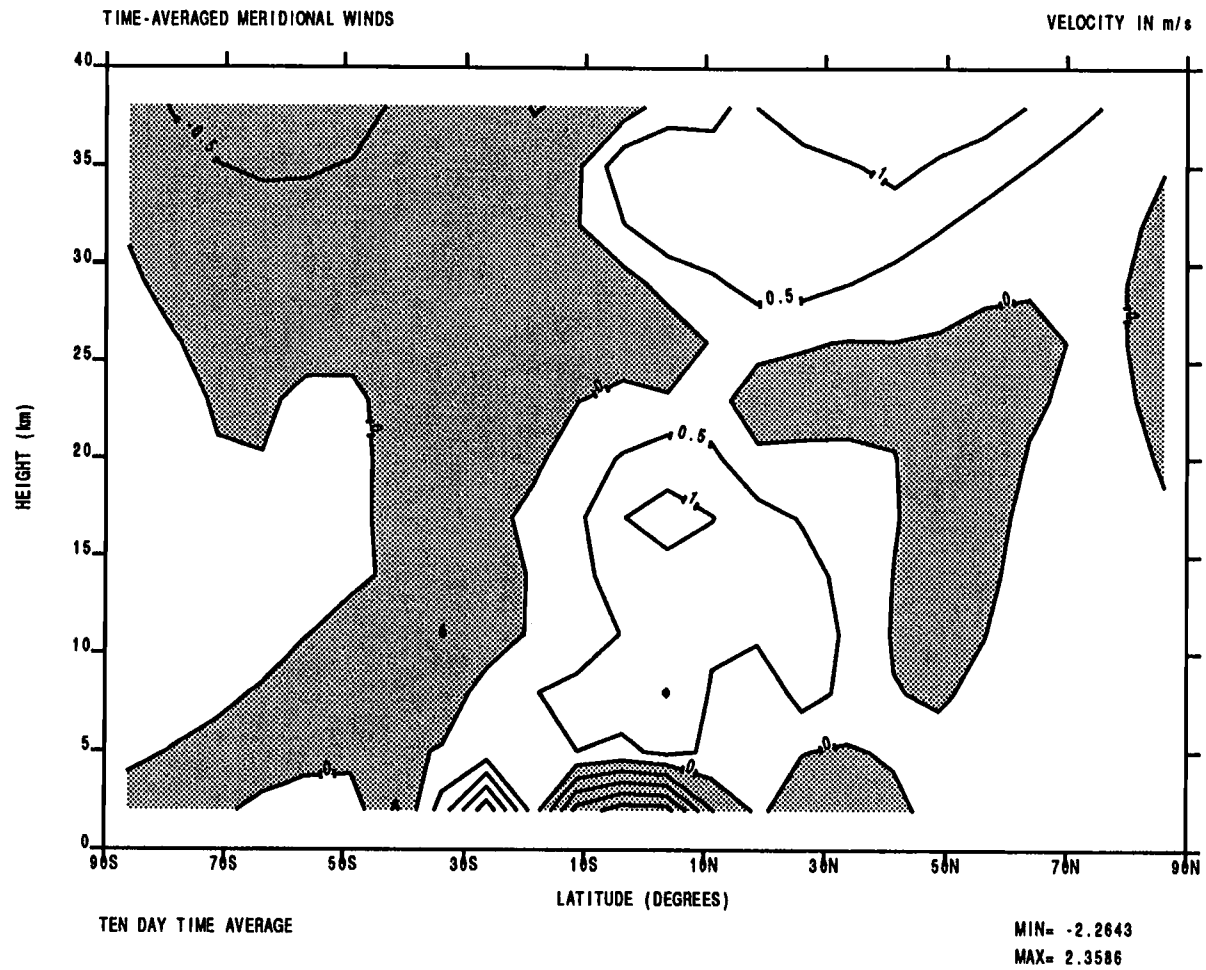


Fig. 3 Time-averaged mean meridional winds for Spring equinox.

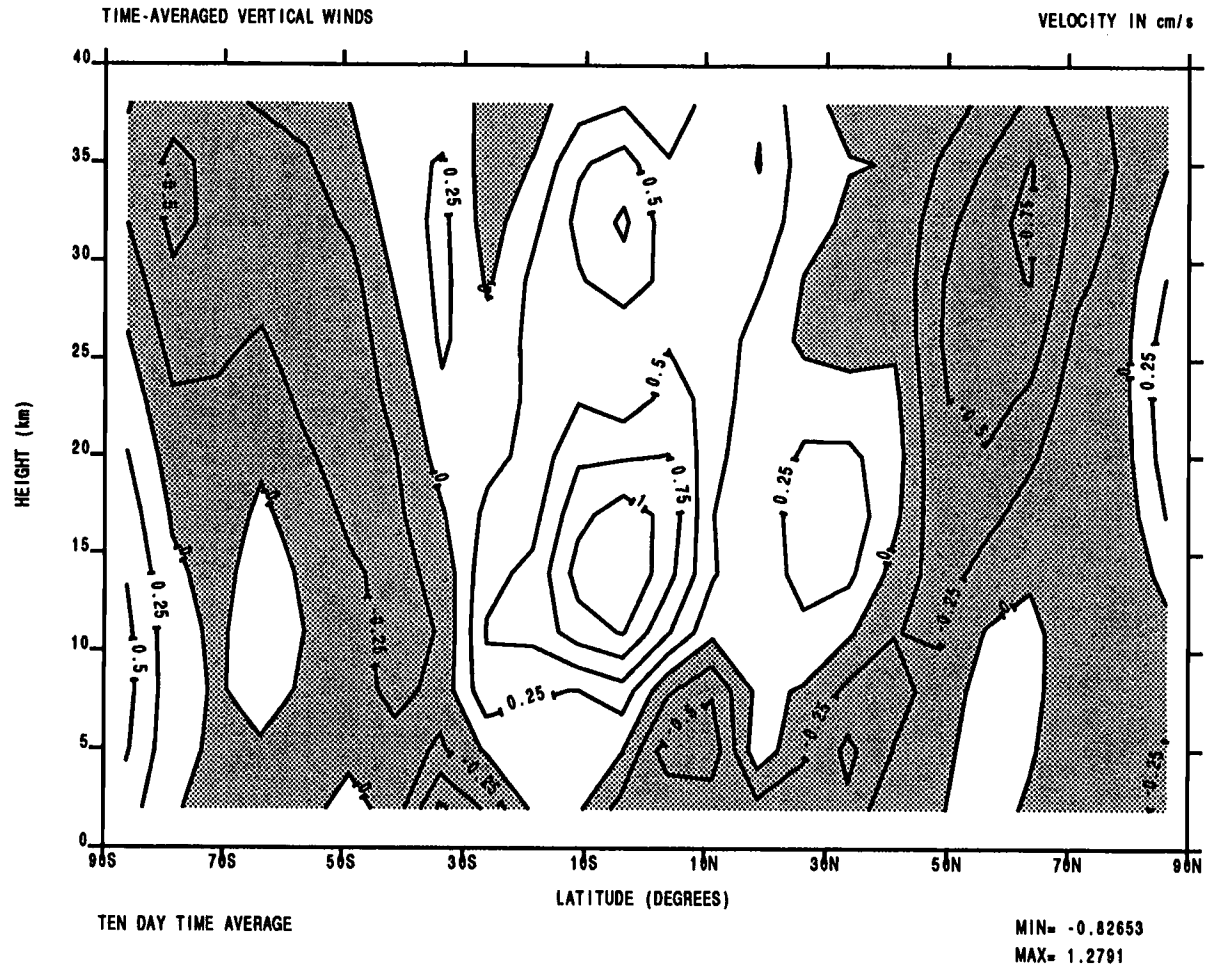


Fig. 4 Time-averaged mean vertical winds for Spring equinox.

The structure of the mean vertical winds shows lifting near the ground at 15S (where the meridional winds meet) and throughout the region from 30S to 30N above 10 km. The strongest upward motion ($\sim 1\text{cm/s}$) is found above the equatorial region from 10 to 20 km. This upward motion corresponds to the rising branches of the Hadley circulation. (It is interesting to note that the strongest rising motion is found closer to the equator rather than 15S where it is expected. This is likely the result of the variable terrain in this latitude belt creating situations where low level winds are suppressed by very stably stratified atmospheres associated with regions where lowlands meet high terrain.) The mid- and high latitudes are dominated by sinking motion which characterizes the descending branches of the two-cell Hadley system at higher latitudes.

The time evolution of the tracer fields from the aerosol model are shown in Figs. 5–12. Figs. 5–8 show the horizontally stratified case with the initial distribution as shown in Fig. 5. Following the time steps it can be seen that the horizontal transport is strongest from about 50S to 20N over the entire vertical extent of the model (as evidenced by the decreasing mean tracer gradient) while the horizontal tracer gradient actually increases towards both poles. The same is true for the vertically stratified case in Figs. 9–12. The strongest mixing again occurs across a region spanning the equator and extending the vertical extent of the model, while the higher latitudes again show an increasing tracer gradient.

Figs. 13 and 14 combine the time-averaged mean mixing ratios with the corresponding eddy fluxes to further highlight the horizontal and vertical eddy transport processes. Fig. 13 shows that the reduction of horizontal gradient

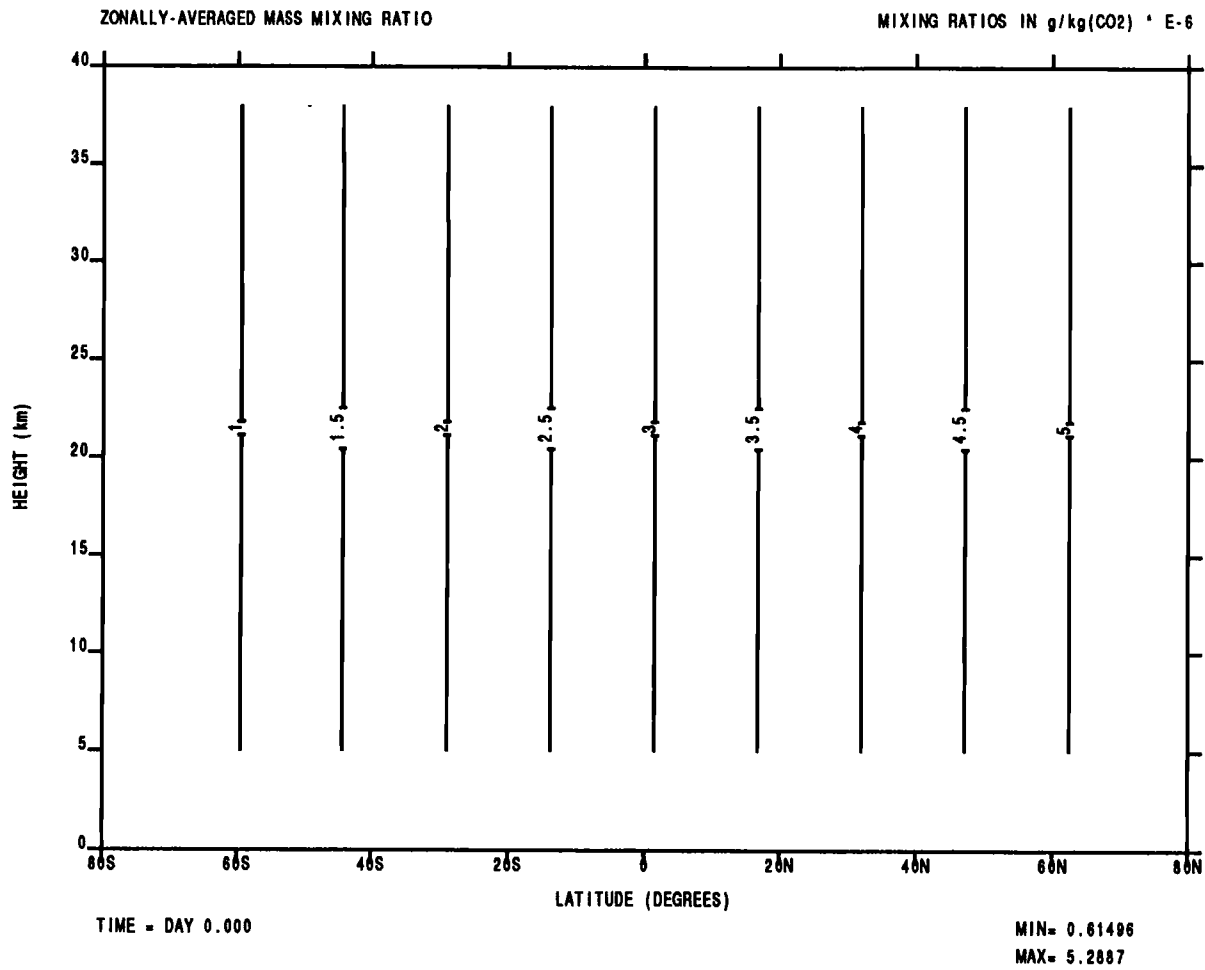


Fig. 5 Initial distribution of the mean mixing ratios for the Spring Equinox horizontally stratified case.

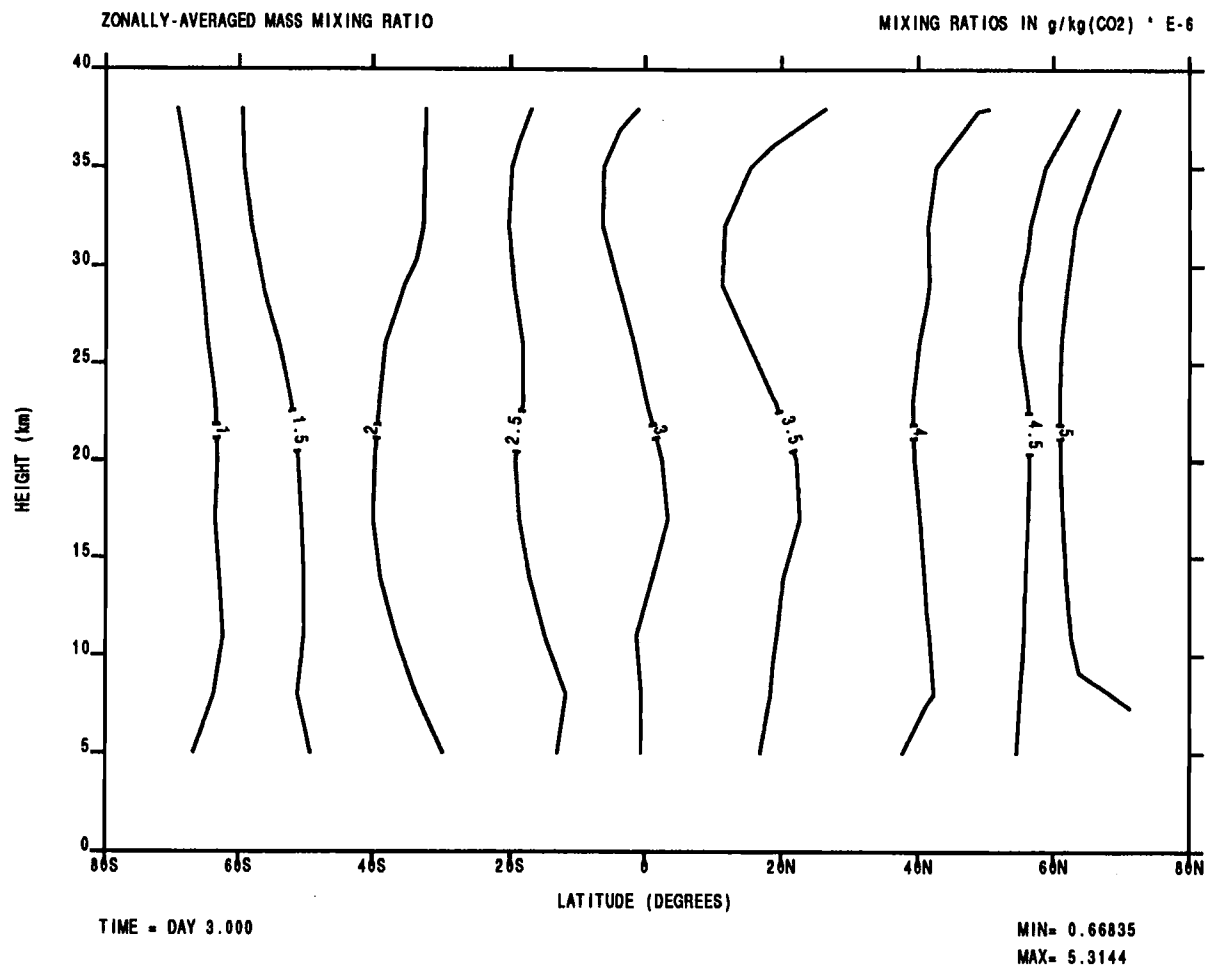


Fig. 6 Distribution of the mean mixing ratios after day 3 for the Spring Equinox horizontally stratified case.

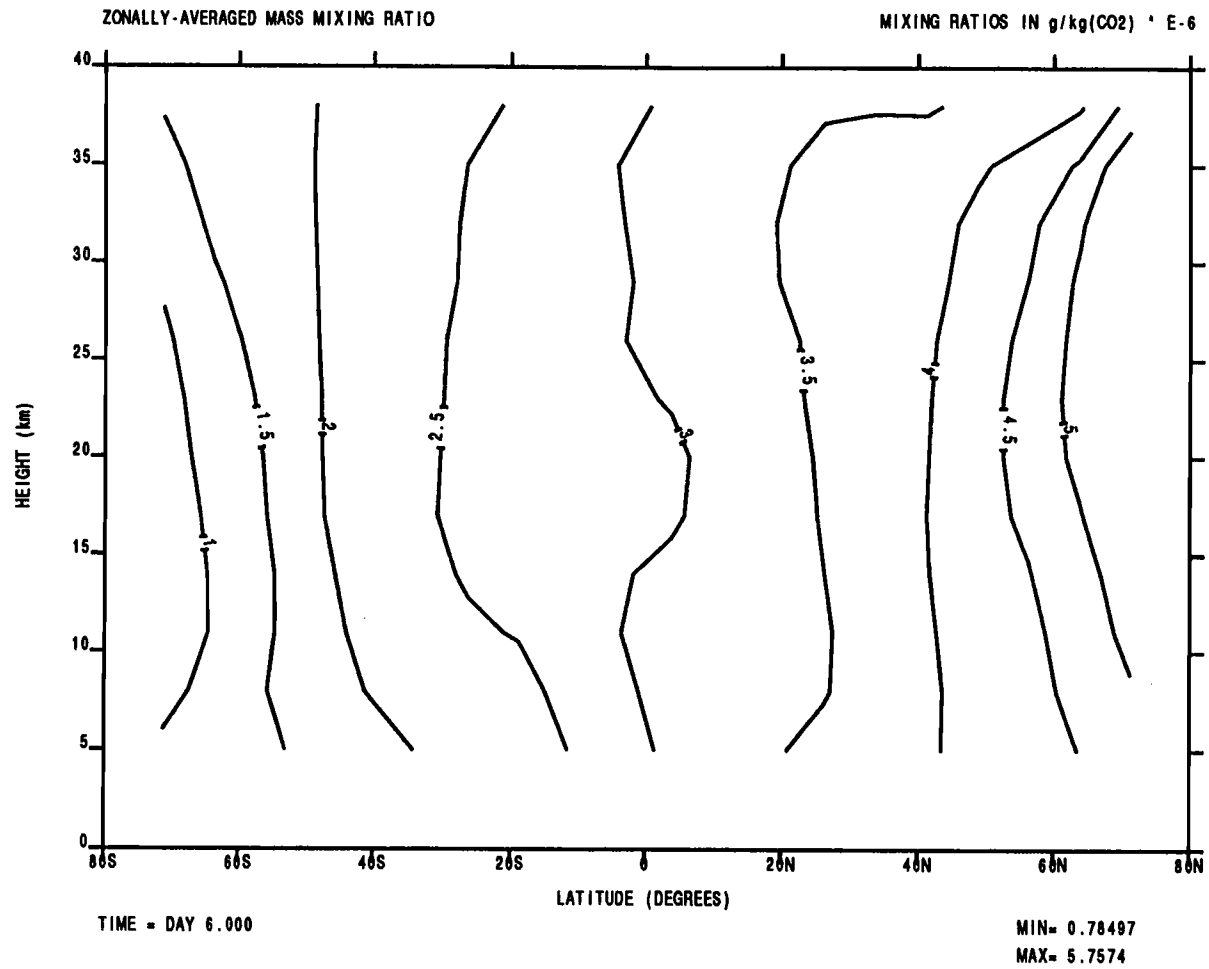


Fig. 7 Distribution of the mean mixing ratios after day 6 for the Spring Equinox horizontally stratified case.

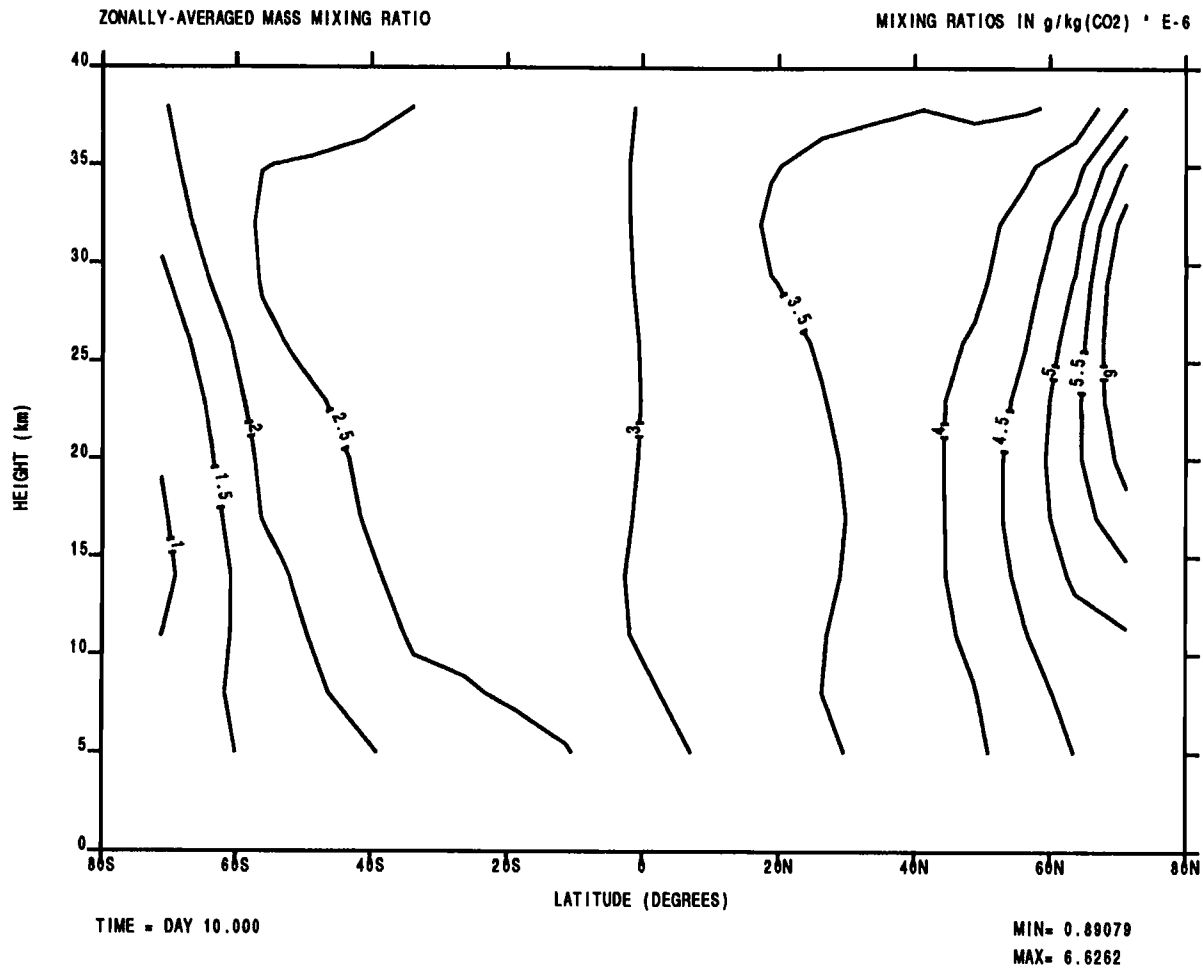


Fig. 8 Distribution of the mean mixing ratios after day 10 for the Spring Equinox horizontally stratified case.

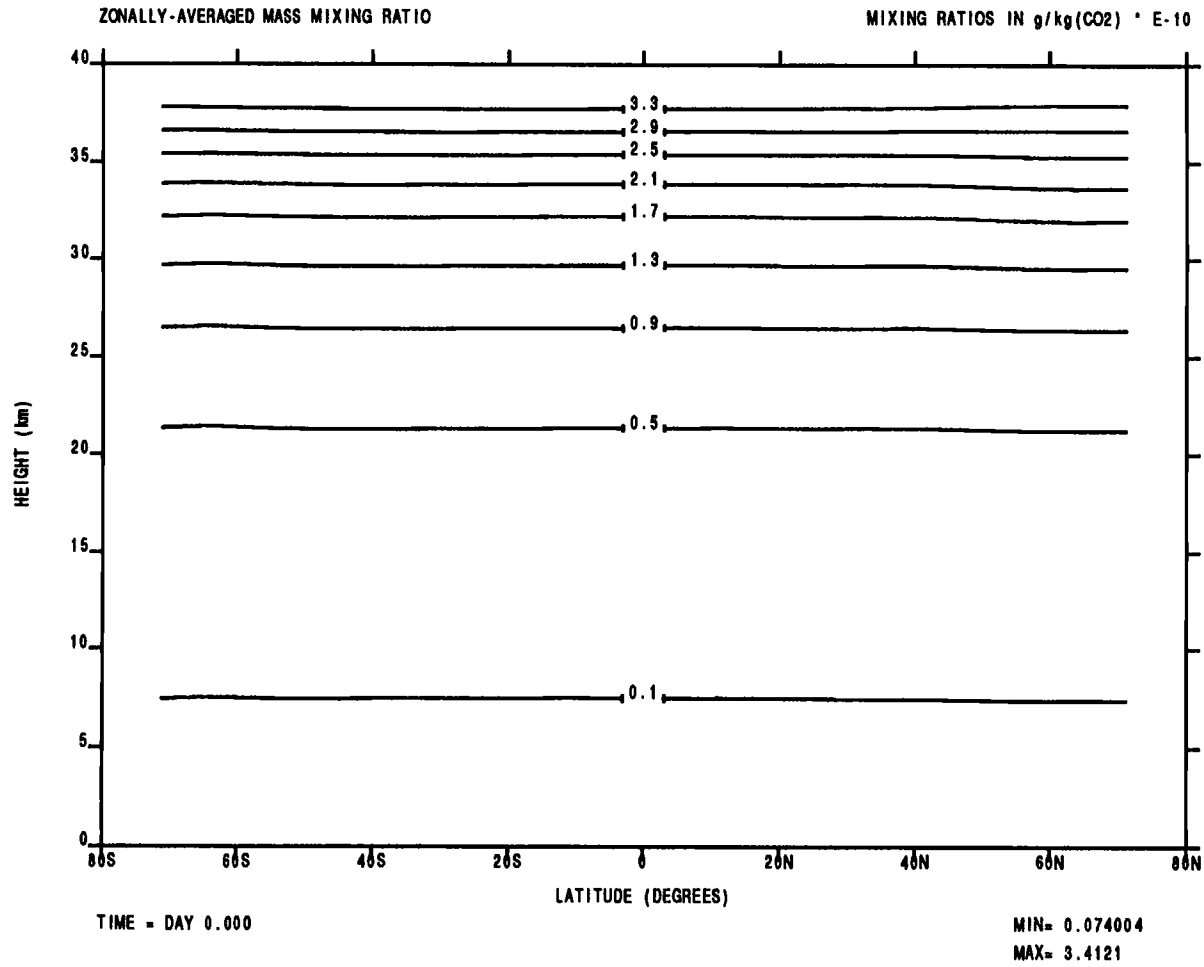


Fig. 9 Initial distribution of the mean mixing ratios for the Spring Equinox vertically stratified case.

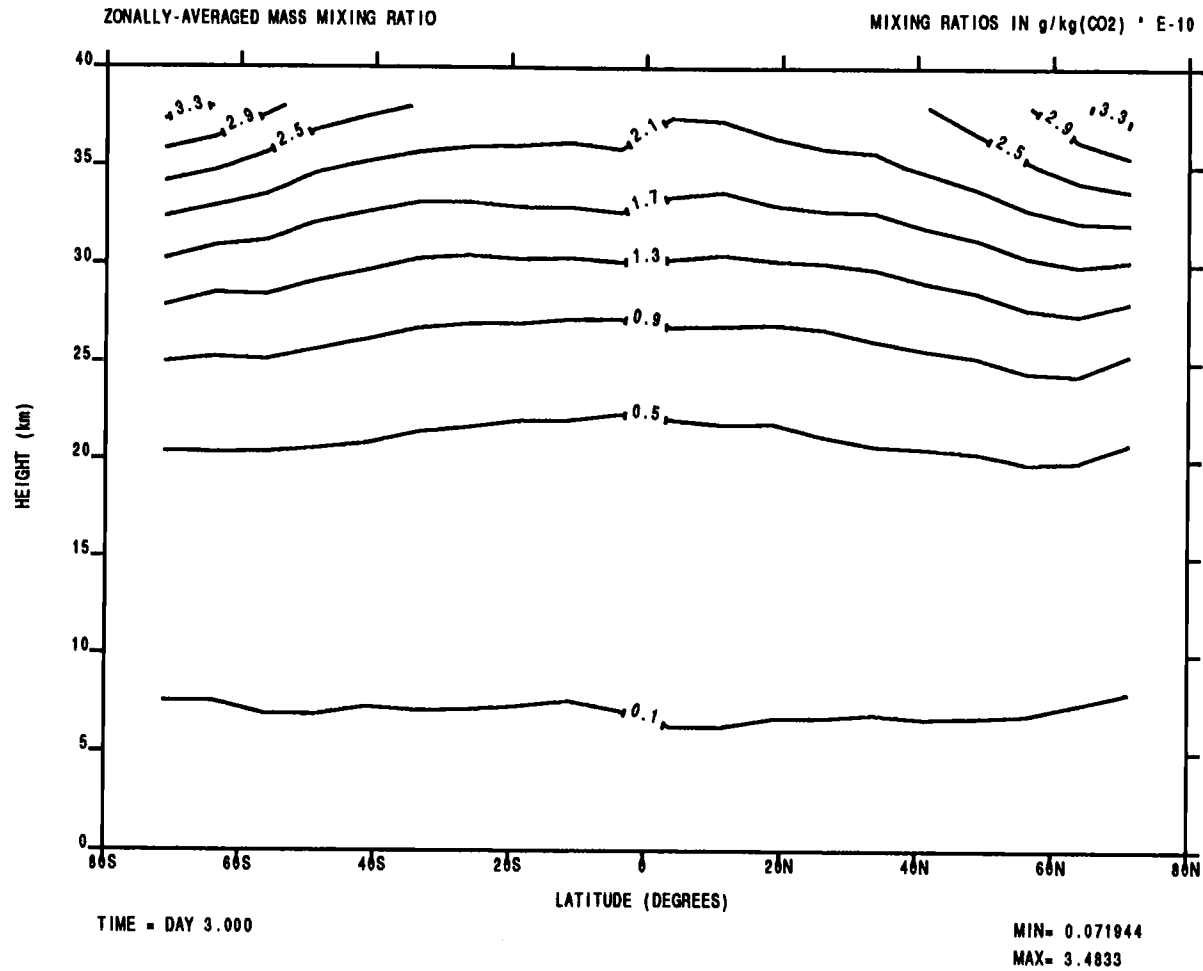


Fig. 10 Distribution of the mean mixing ratios after day 3 for the Spring Equinox vertically stratified case.

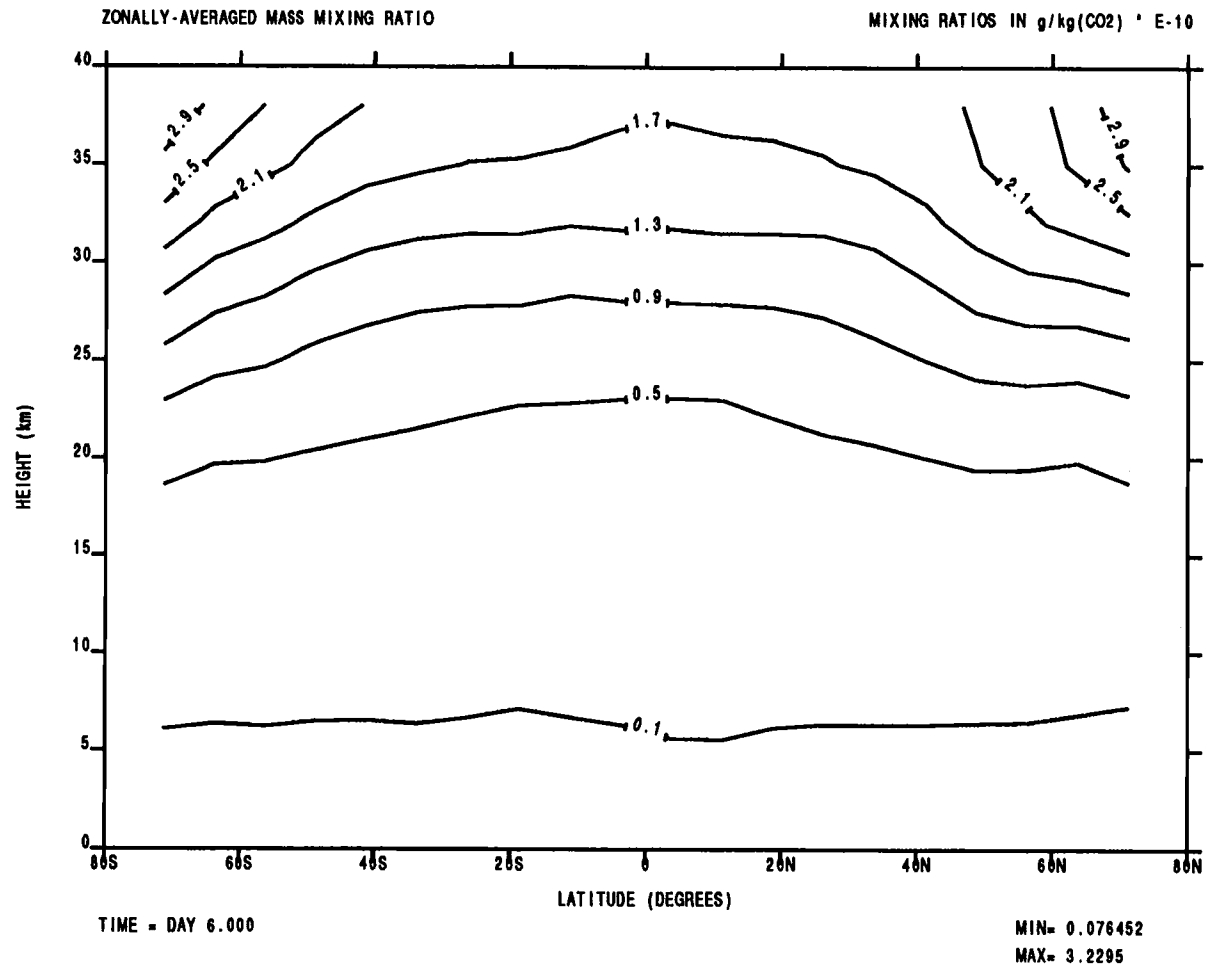


Fig. 11 Distribution of the mean mixing ratios after day 6 for the Spring Equinox vertically stratified case.

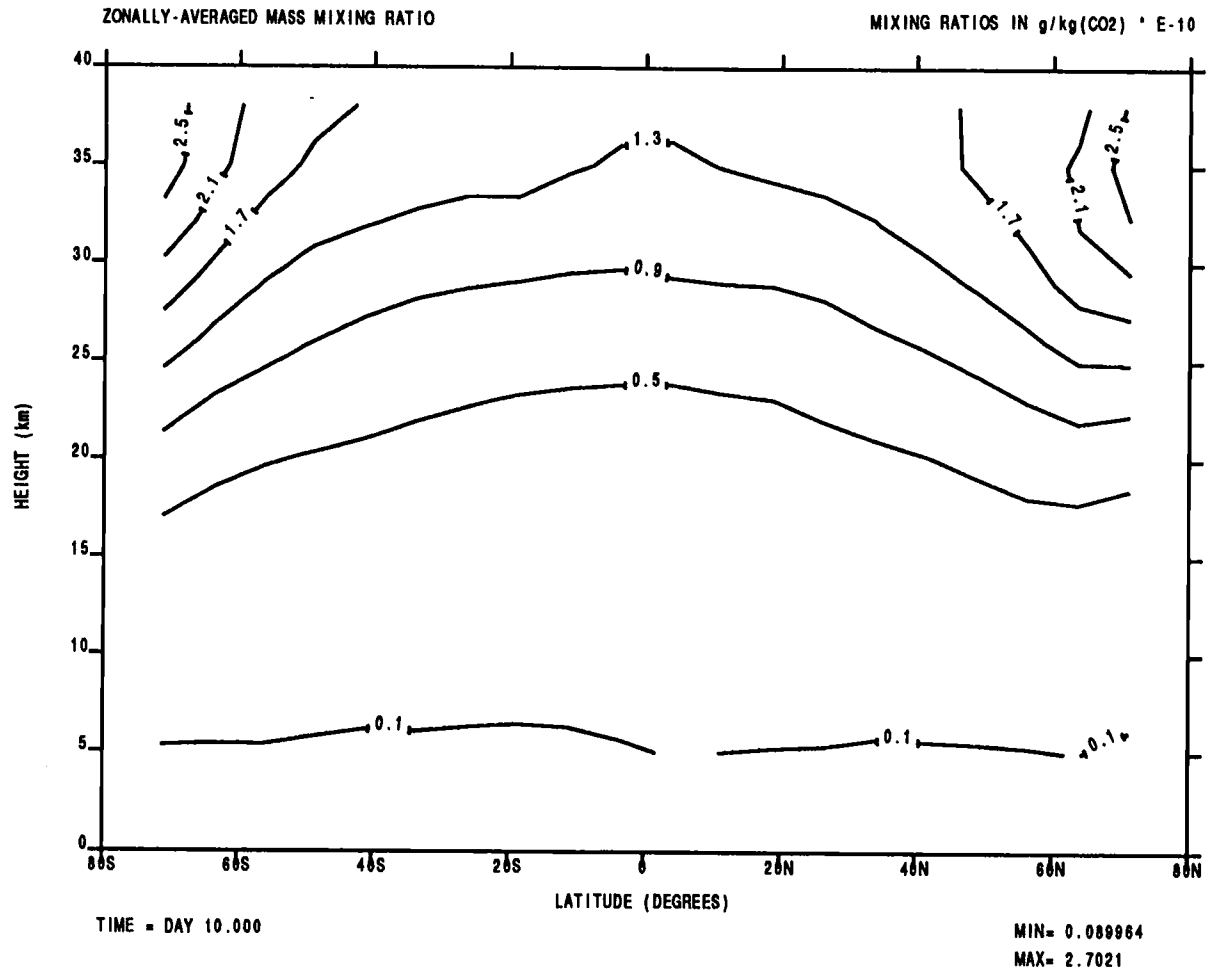


Fig. 12 Distribution of the mean mixing ratios after day 10 for the Spring Equinox vertically stratified case.

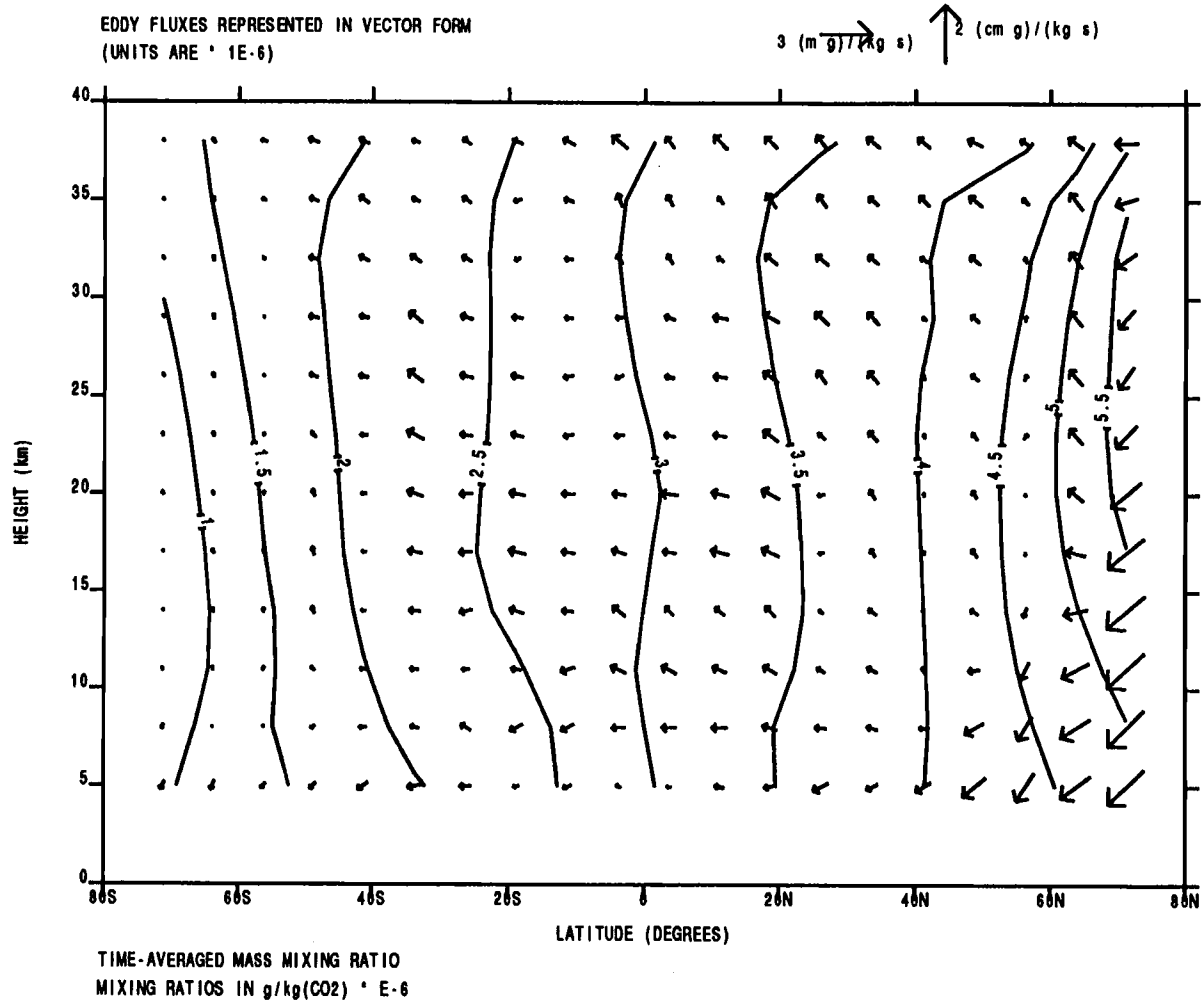


Fig. 13 Time-averaged mean mixing ratios and eddy fluxes for the Spring Equinox horizontally stratified case.

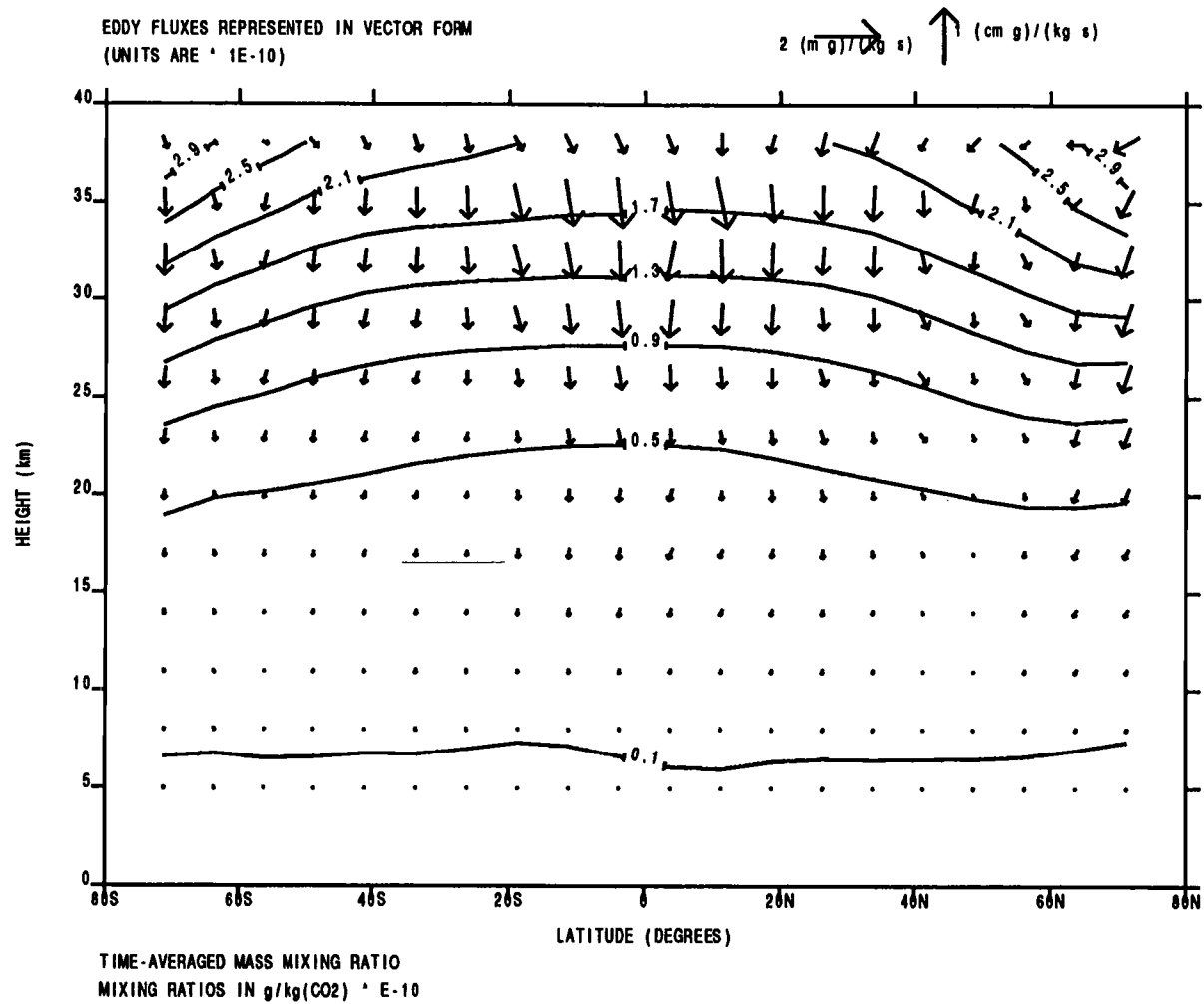


Fig. 14 Time-averaged mean mixing ratios and eddy fluxes for the Spring Equinox vertically stratified case.

is greatest in the Southern tropics and mid-latitudes in agreement with Fig. 3. Likewise, Fig. 14 shows that the strongest vertical transport occurs over the equator in the highest altitudes of the model as expected from Fig. 4. The vertical case exhibits a poleward-downward slope of the contours at mid- to high latitudes. This sloping of the isopleths is a result of the strong lifting motion of the mean meridional circulation over the equator and the strong descending motion over the high latitudes at the top of the model (see Fig. 15). The mean transport circulation (to be examined below) also has this basic character. Such a slope is observed for vertically stratified tracers (e.g., water, ozone, radioactive debris) in the Earth's stratosphere and the model results of Plumb and Mahlman [1987] show this feature very clearly.

The eddy flux plots display the direction of the eddy transport. The horizontally stratified case shows that the eddy fluxes at mid-latitudes are directed much less "cross-contour" than those at low latitudes. As Plumb and Mahlman [1987] note,

"this is indicative of advective-type eddy fluxes (antisymmetric [K]) in these regions; indeed this is a characteristic signature of eddy fluxes of conserved tracers in the absence of parcel dispersion (Clark and Rogers, 1978; Plumb, 1979; Matsuno, 1980)."

The downgradient direction of the eddy fluxes in the lower latitudes is indicative of diffusive-type eddy transport in these regions. The vertical case shows that nearly all of the eddy fluxes are directed downgradient at all latitudes. This indicates that diffusive type transport is the dominate type for a vertically stratified tracer. Thus, it is not surprising to find that the strongest fluxes are located at high altitudes where the mixing ratios are largest.

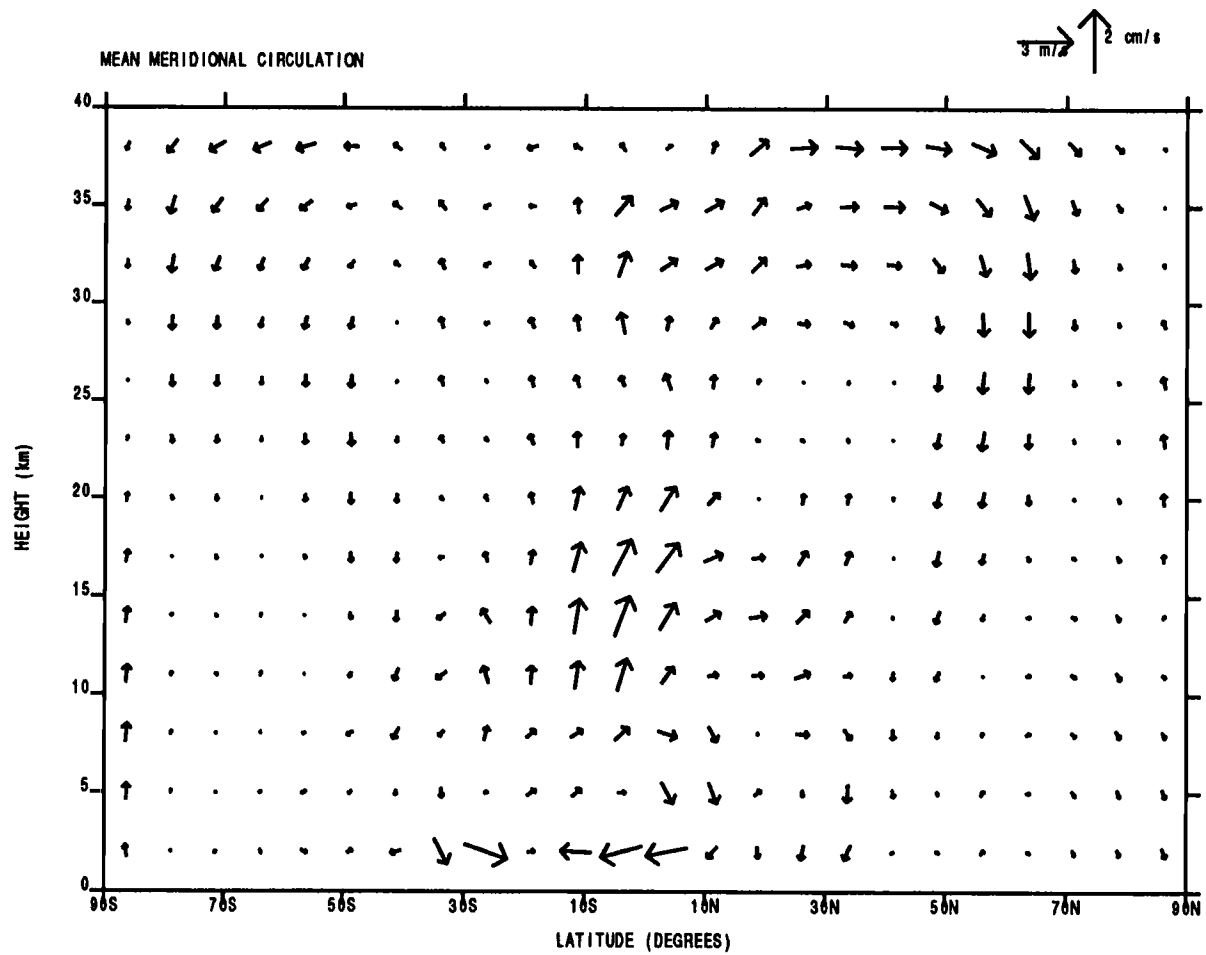


Fig. 15 Mean meridional circulation for the Spring equinox case.

Fig. 15 combines the mean vertical and meridional winds into a vector plot displaying the mean meridional circulation (\bar{v} , \bar{w}). In accordance with the previous plots of \bar{v} and \bar{w} the plot shows a circulation system consisting of two Hadley cells. In the southern hemisphere the cell is slightly smaller and spans the mid- to low latitudes (60S-10S) where it meets the second cell which crosses the equator and extends to the middle latitudes of the northern hemisphere. The circulation is most vigorous over the equator (where the air is rising and subsequently branching off to the north and south at higher altitudes) and at high altitudes above the mid-latitudes in the Northern hemisphere. The mean circulation continues towards higher latitudes where it begins to descend and return back to the equatorial regions at low altitudes. Also observable in Fig. 15 is a small cross-equatorial cell located in the lowest levels between 15S and 10N. The cause of this feature is not precisely known but again may be attributable to the effects of the variable terrain as mentioned in the discussion of the mean winds.

Fig. 16 shows the effective transport circulation, \vec{U}_T , which exhibits the same general dual Hadley cell structure as the mean meridional circulation. The cells in both Figures are similar in location and extent but, the magnitudes of the vectors composing the Hadley cells differ in some regions. In general, the transport circulation has larger magnitudes than the mean meridional circulation. This is especially noticeable at low levels where the transport circulation magnitude is significantly larger than that of the mean meridional circulation.

It should be noted here that in this plot and those for K_{yy} and K_{zz} that the lowest level of the atmosphere and the highest two latitudes in each hemisphere have been omitted. The lowest level was omitted for the reason mentioned earlier; the

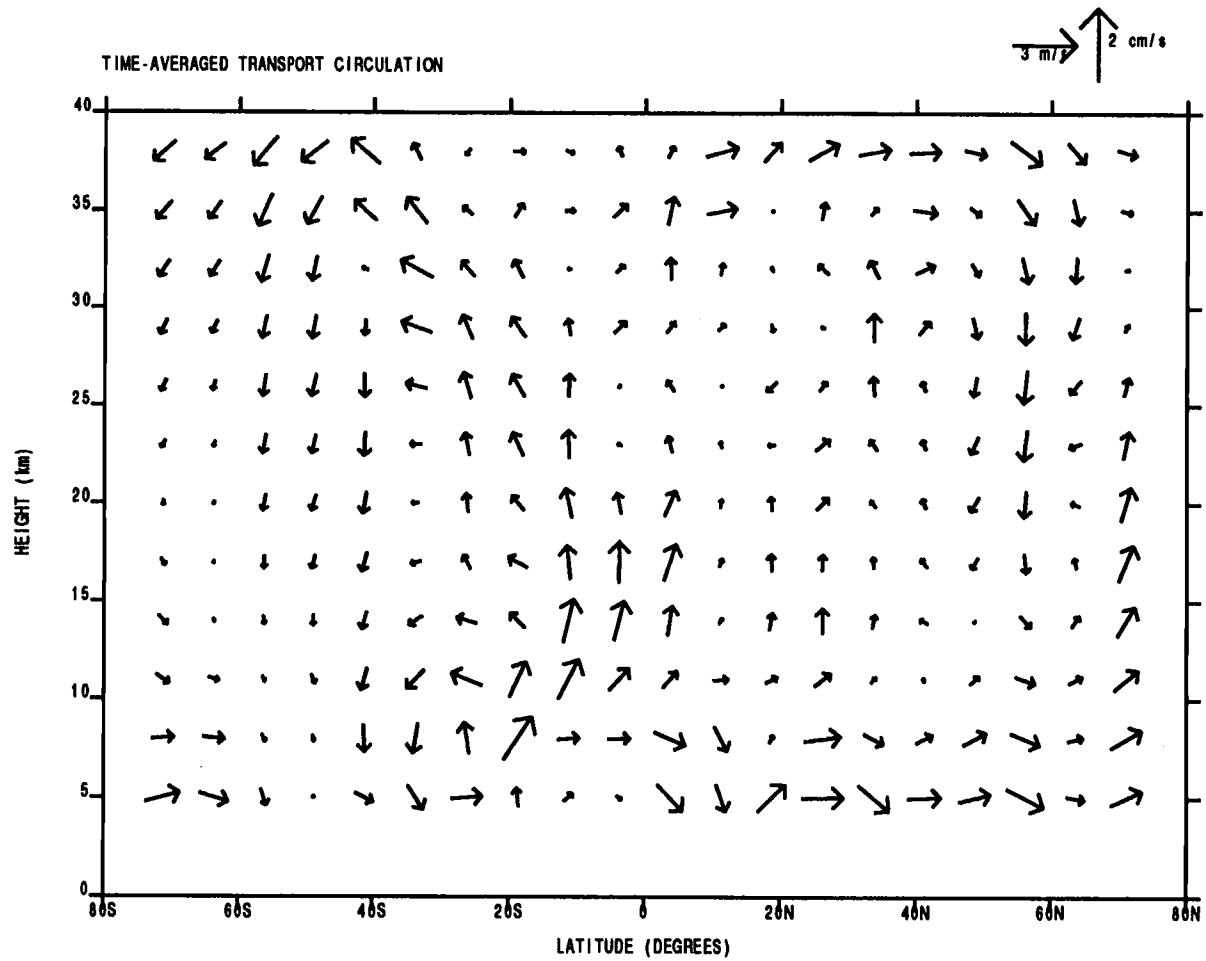


Fig. 16 Effective transport circulation for the Spring equinox case.

effect of the terrain on calculating a true zonal-average of winds and mixing ratios would also effect the accuracy of determining K values (and thus the transport circulation) at this level. The highest two latitudes in each hemisphere were neglected because the mixing ratio evolution near the poles appeared suspect. There was some question as to the GCM's performance near the poles for these particular experiments. The transport code is designed to model the transport by redistributing the air parcels while conserving mass. However, in some of the experiments it appeared to be adding mass to some of the parcels in the polar regions as evidenced by mean tracer mixing ratios well outside of the initial values of the mean mixing ratios. It is suspected that the error is at least partly due to the conversion from the geometric scale of the GCM to that of the transport model at polar latitudes. This problem only appears at the poles and only for certain cases and thus does not have any effects on the results for the region of the atmosphere considered.

The vectors representing \vec{U}_T show the direction of the basic flow of air mass and represent the "advective mass flux" of Kida [1983]. The diffusion of the tracer may be thought of as superimposed on this basic flow. Comparing the transport circulation with the calculated diffusivities in Figs. 17 and 18 it is seen that there is a tendency for the strongest part of this circulation to be directed towards regions of strong diffusive mixing (especially over the equator and poles).

The calculated horizontal and vertical eddy diffusivities are shown in Figs. 17 and 18, respectively. The values were found to be positive at almost all points with the exception of a few negative values usually located near the smallest positive values and towards the poles. (This was true for all three experiments.) Following

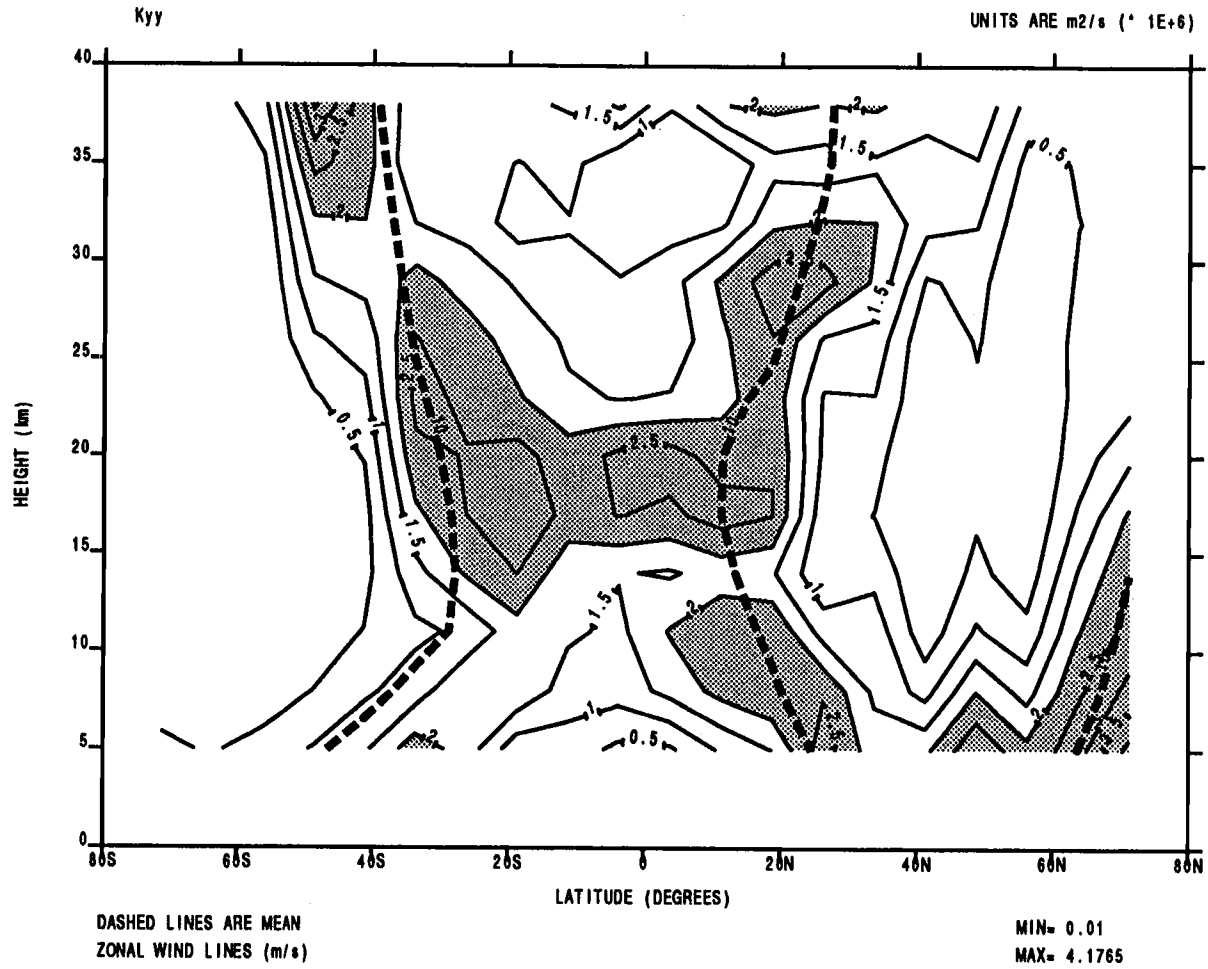


Fig. 17 Distribution of K_{yy} , the horizontal eddy diffusion coefficient, for the Spring Equinox case.

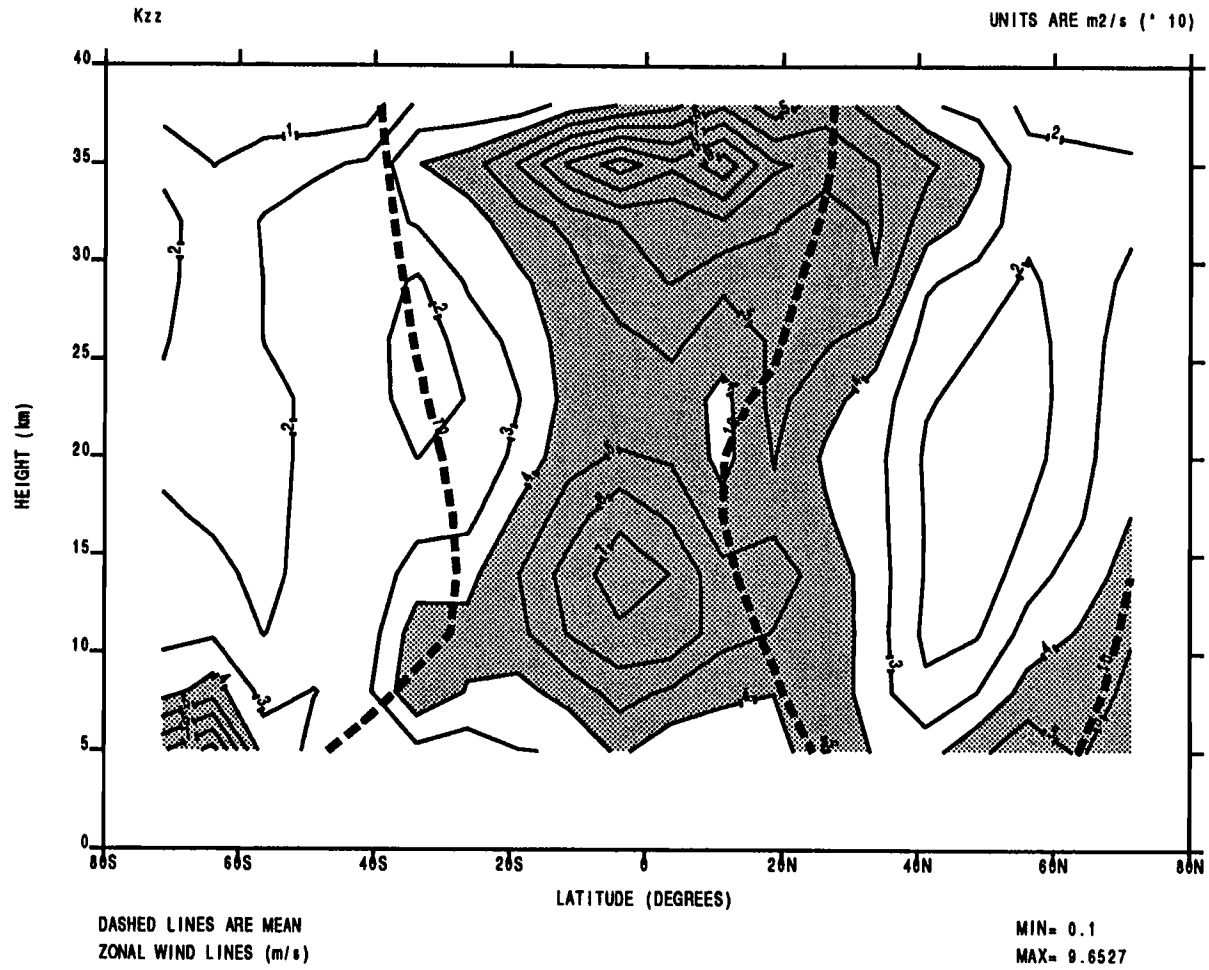


Fig. 18 Distribution of K_{zz} , the vertical eddy diffusion coefficient, for the Spring Equinox case.

Plumb and Mahlman [1987], some "quality control" was exercised on K_{yy} (D_{yy}) and K_{zz} (D_{zz}) by setting K_{yy} and K_{zz} to minimum values wherever the calculated values were less than these. (The minimum values adopted were approximately two orders of magnitude below the typical values calculated. The minimum values chosen were 10^4 m²/s for K_{yy} and 1 m²/s for K_{zz} .) After this, the criterion $D_{yz}^2 \leq D_{yy}D_{zz}$ was applied and if any grid points did not satisfy this condition then D_{zz} was set equal to D_{yz}^2/D_{yy} . This criterion was applied to make sure the component of eddy flux associated with [D] (see equation 28) was purely diffusive [Matsuno, 1980]. In all three experiments this criterion was met and no further modification of the D_{zz} values was necessary.

Fig. 17 shows that the largest values of K_{yy} ($1.5-4 \times 10^6$ m²/s) are located in three main regions: mid and high northern latitudes at low altitudes (5–10 km), from 30S to 30N at altitudes of 15–30 km, and at mid-latitudes at the top of the model. The high altitude bands of strong mixing are most likely the result of diffusive mixing produced by planetary waves. The correlation of these regions with the 10 m/s zonal wind line suggests that the most likely source of this strong horizontal mixing is the breaking of transient and/or quasistationary planetary waves propagating equatorwards in both hemispheres. The bands of strong mixing at lower altitudes, especially in mid- to high latitudes, are likely due to transient eddies which are very vigorous in these regions.

Fig. 18 shows strong vertical mixing (K_{zz} from 50–90 m²/s) in three main regions: at mid- to high latitudes in both hemispheres between 5–10 km, and above the equatorial latitudes between 8–20 km and 25–38 km. The strong vertical mixing

in the mid- to high latitudes may be due to transient eddies associated with mid-latitude Martian storm systems, while the mixing in equatorial regions is probably due to the thermal tides discussed by Zurek [1976]. The strongest mixing is at the top of the model over the equatorial region. This is not surprising since Zurek [1976] found that the strongest diurnal response of the Martian atmosphere was over the areas of large topography in the tropics and subtropics.

Zurek also noted "that vertically propagating tidal components, growing exponentially as density decreases with height, will dominate the dynamics of the middle Martian atmosphere (30–80 km)." It is in this same region of the atmosphere that Zurek expects the tidal fields to degenerate into turbulence due to large wind shears or unstable temperature distributions embedded within the fields. Thus, strong vertical mixing would be expected in such regions and the diurnal tides are believed to be the dominant contributor to the strong vertical mixing over the equatorial region (especially near the top of the model). It is likely that the band of strong vertical mixing at low altitudes above the equator is also due to the tides, but it could also be associated with planetary waves.

Figs. 19–21 support the suggestions above as to the likely sources responsible for the strong diffusive mixing in both the horizontal and vertical. (These figures have been provided by J. Barnes, 1994, personal communication, and correspond to roughly the same season.) Figs. 19 and 20 show the transient eddy horizontal and vertical heat fluxes for lower frequency motions (> 2 days), respectively. What is seen is that for the time scales appropriate to mid-latitude transient eddies the regions of maximum activity are found in mid- to high latitudes at low levels. This

supports the assertion that the horizontal mixing at mid- to high latitudes is due to the transient eddies.

Fig. 21 is the transient rms temperature variance after high-pass filtering to isolate the tidal motions. This plot shows that the largest thermal tides are in the equatorial regions near the ground and at the top of the model (~ 40 km). Thus one expects the tides to have their strongest influence over the equatorial region at equinox, especially at upper levels where they may be tending to break. There is convective adjustment occurring in the Mars GCM in this upper region, which may be associated with tidal breaking, but convective mixing of tracer mass does not occur in the present transport simulations.

30A4 TRANS. EDDY HORIZ. HEAT FLUX: LOW ($^{\circ}\text{K m/s}$)

RUN 87.55
TAUTOT = 0.3
MAX = $1.24 \cdot 10^4$ $^{\circ}\text{K m/s}$

SEASONAL DATES: 10.15 - 24.28

TIME AVERAGE 480.0HRS
TO 1200.0HRS
MIN = $-8.10 \cdot 10^0$ $^{\circ}\text{K m/s}$

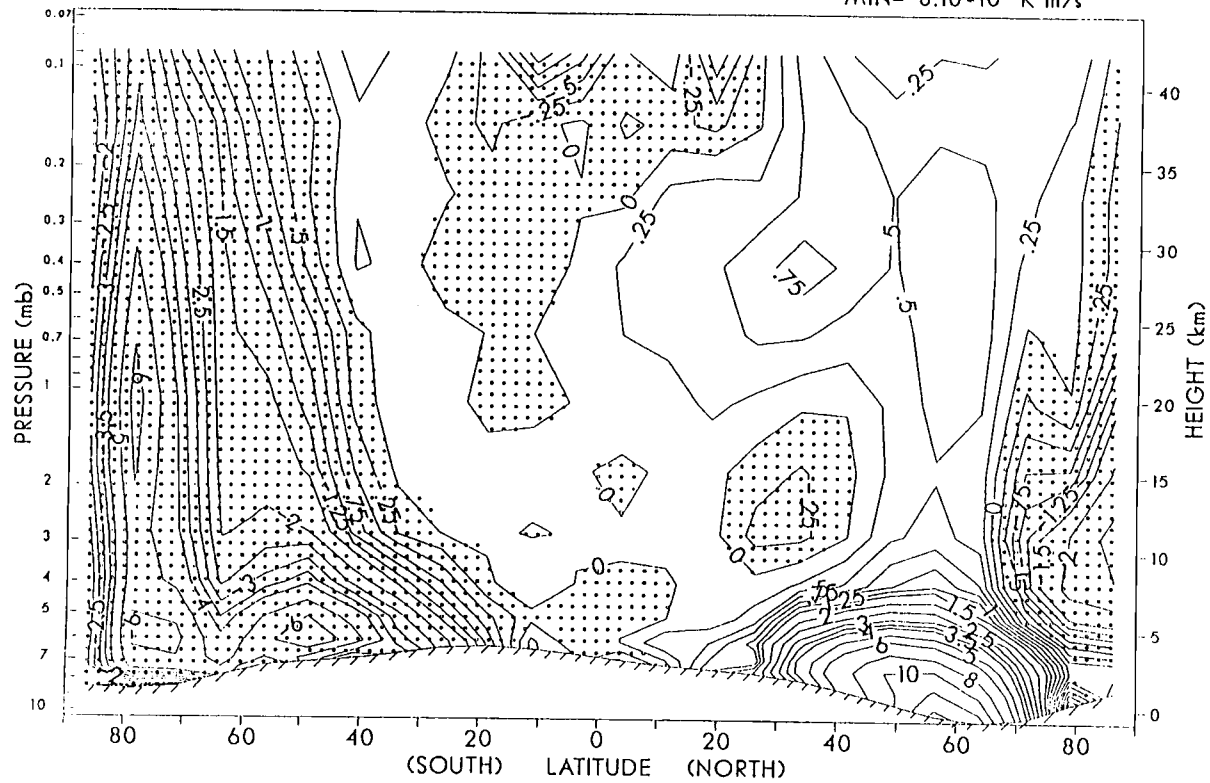


Fig. 19 Distribution of the transient eddy horizontal heat fluxes (after low-pass filtering) showing the regions of significant transient eddy activity.

30A6 TRANS. EDDY VERT. HEAT FLUX: LOW ($10^{-6} \text{ }^\circ\text{K m/s}$)

RUN 87.55
TAUTOT = 0.3
MAX = $5.62 \cdot 10^{-1} \text{ }^\circ\text{K m/s}$

SEASONAL DATES: 10.15 - 24.28

TIME AVERAGE 480.0HRS
TO 1200.0HRS
MIN = $-1.66 \cdot 10^0 \text{ }^\circ\text{K m/s}$

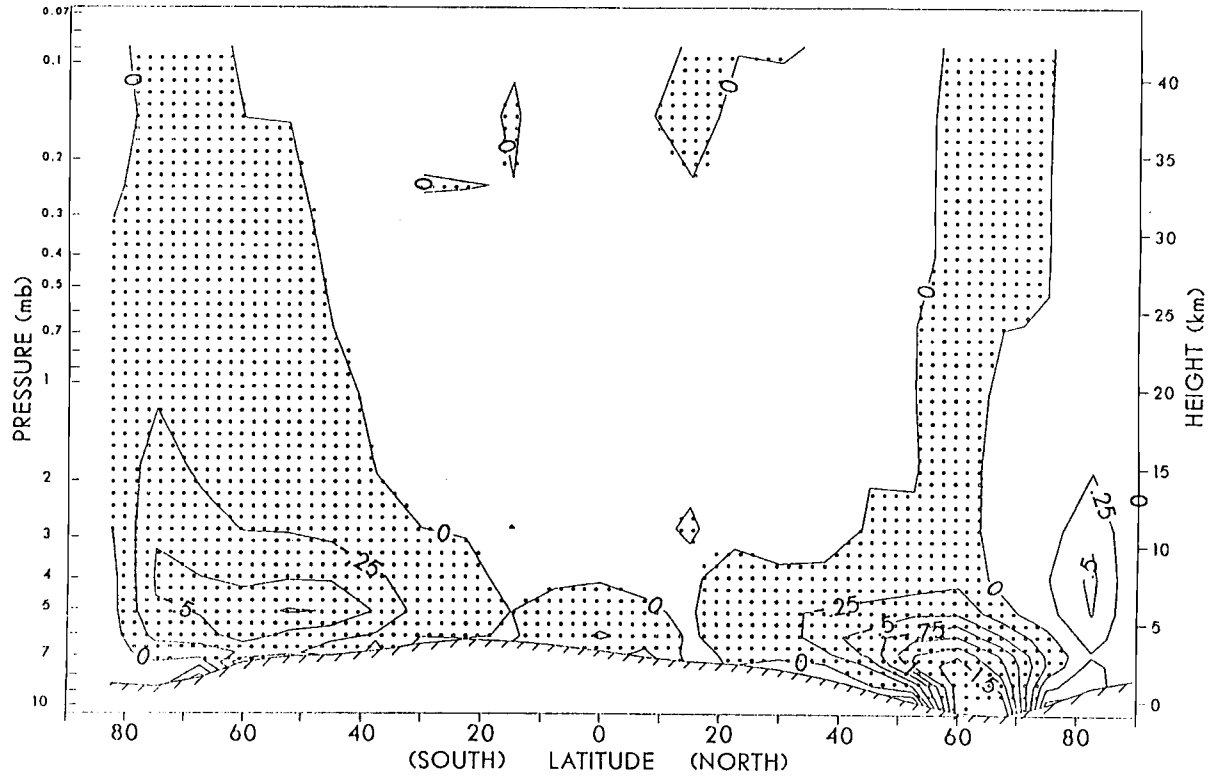


Fig. 20 Distribution of the transient eddy vertical heat fluxes (after low-pass filtering) showing the regions of significant transient eddy activity.

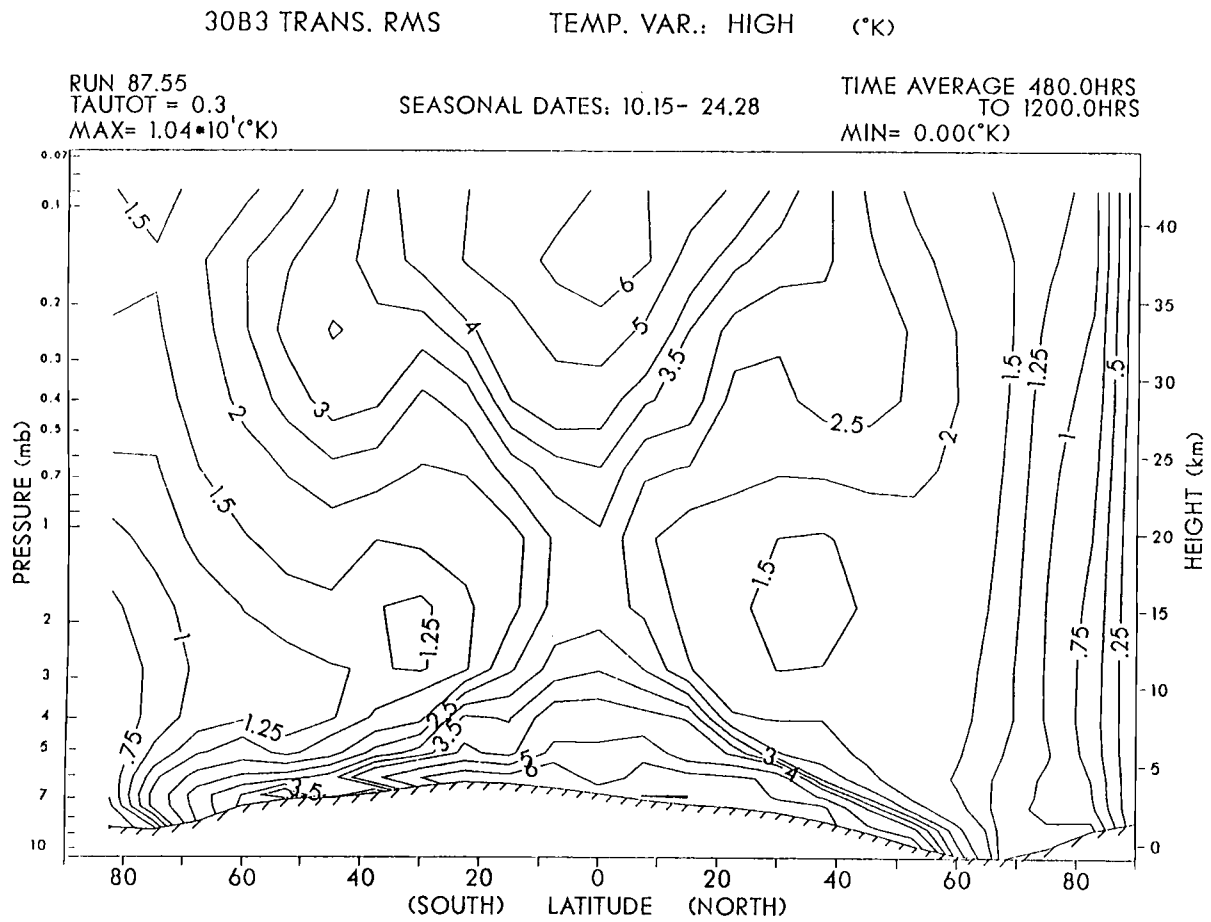


Fig. 21 Distribution of the transient rms temperature variance (after high-pass filtering) showing the influence of the thermal tide.

4.2 Experiment 2: Northern Winter Solstice (no dust loading)

The winter solstice case spans $L_s = 255^\circ$ – 286° and is for an optical depth of $\tau = 0$. It was run for 30 sols with the last ten used as the input to the aerosol model. This same season (L_s span) will be used in the third experiment but the dust loading (as simulated by τ) will be changed in order to analyze the effects of dust on circulation and transport.

Figs. 22–24 show the mean zonal, meridional, and vertical winds respectively. Again, excellent agreement exists with the results of Haberle et al. [1993] who run a similar northern winter solstice experiment. The structure of each component of the circulation is nearly identical to those pictured in Haberle et al.'s work. However, the magnitudes of the winds are slightly less than their results. (This is due to the fact that they used $\tau = 0.3$. As will be seen later, a dusty atmosphere increases the intensity of the Martian circulation.)

The mean zonal winds are predominately westerly in the northern hemisphere and easterly in the southern hemisphere (from the equator to 60S) with both increasing in magnitude with height (as expected from the thermal wind balance). Weak westerlies dominate the winds of the high southern latitudes. The winds in the northern hemisphere are much more intense than those in the southern hemisphere. For example, the winter jet (~ 95 m/s) is approximately three times stronger than the summer jet (~ 35 m/s).

Another interesting feature of the mean zonal circulation is the surface westerly jet found in the southern subtropics. This was also observed by Haberle et al. [1993] who noted that

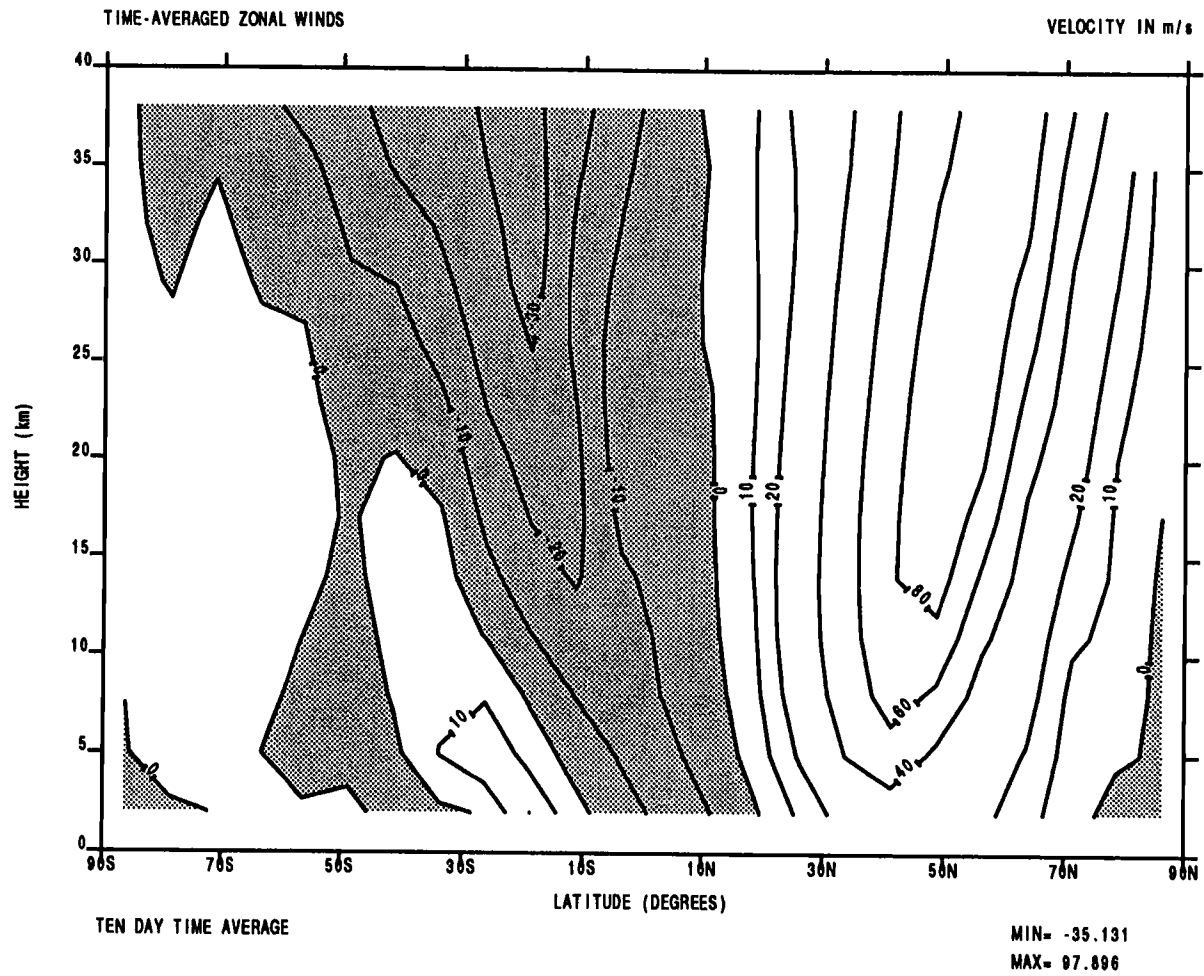


Fig. 22 Time-averaged mean zonal winds for the northern hemisphere winter solstice case with no dust loading.

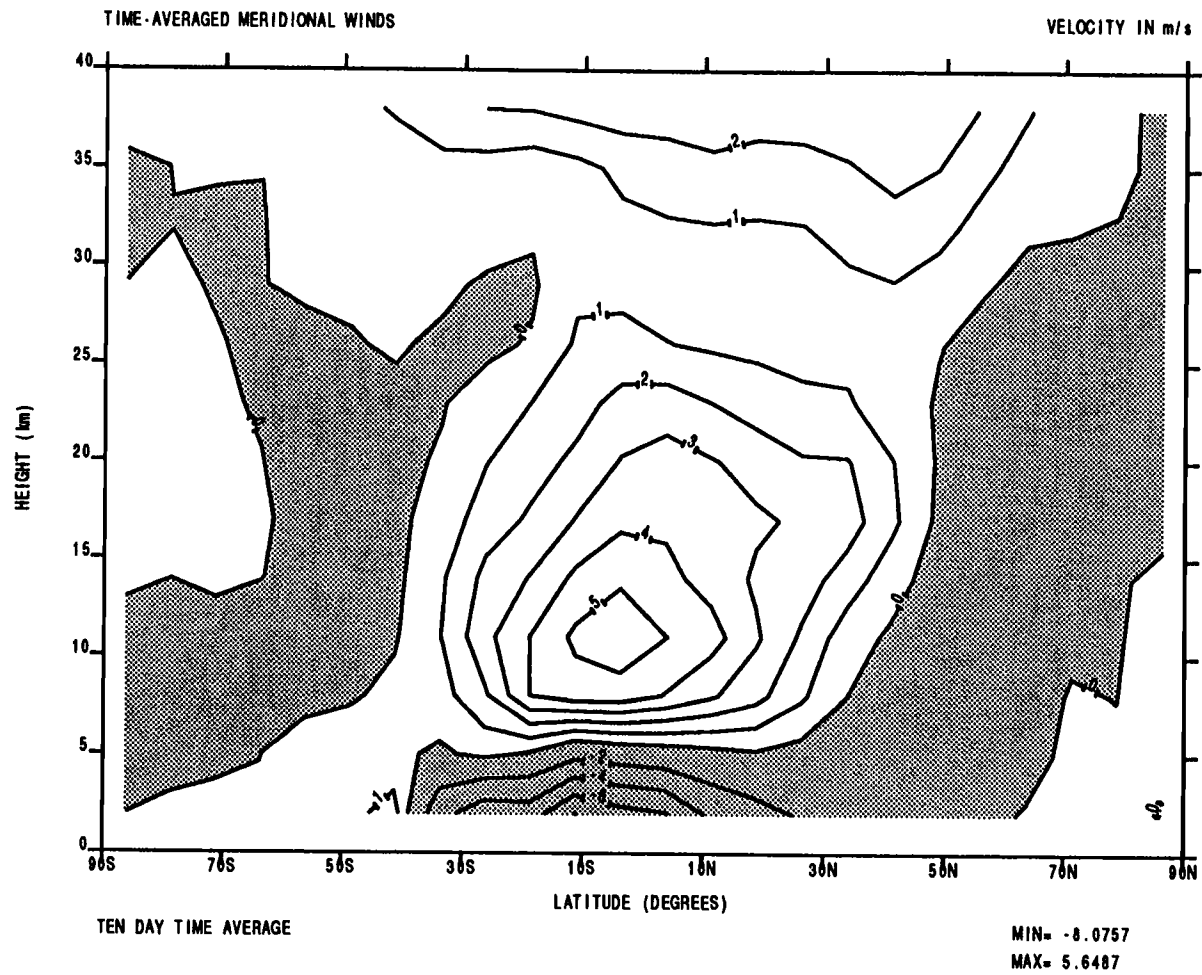


Fig. 23 Time-averaged mean meridional winds for the northern hemisphere winter solstice case with no dust loading.

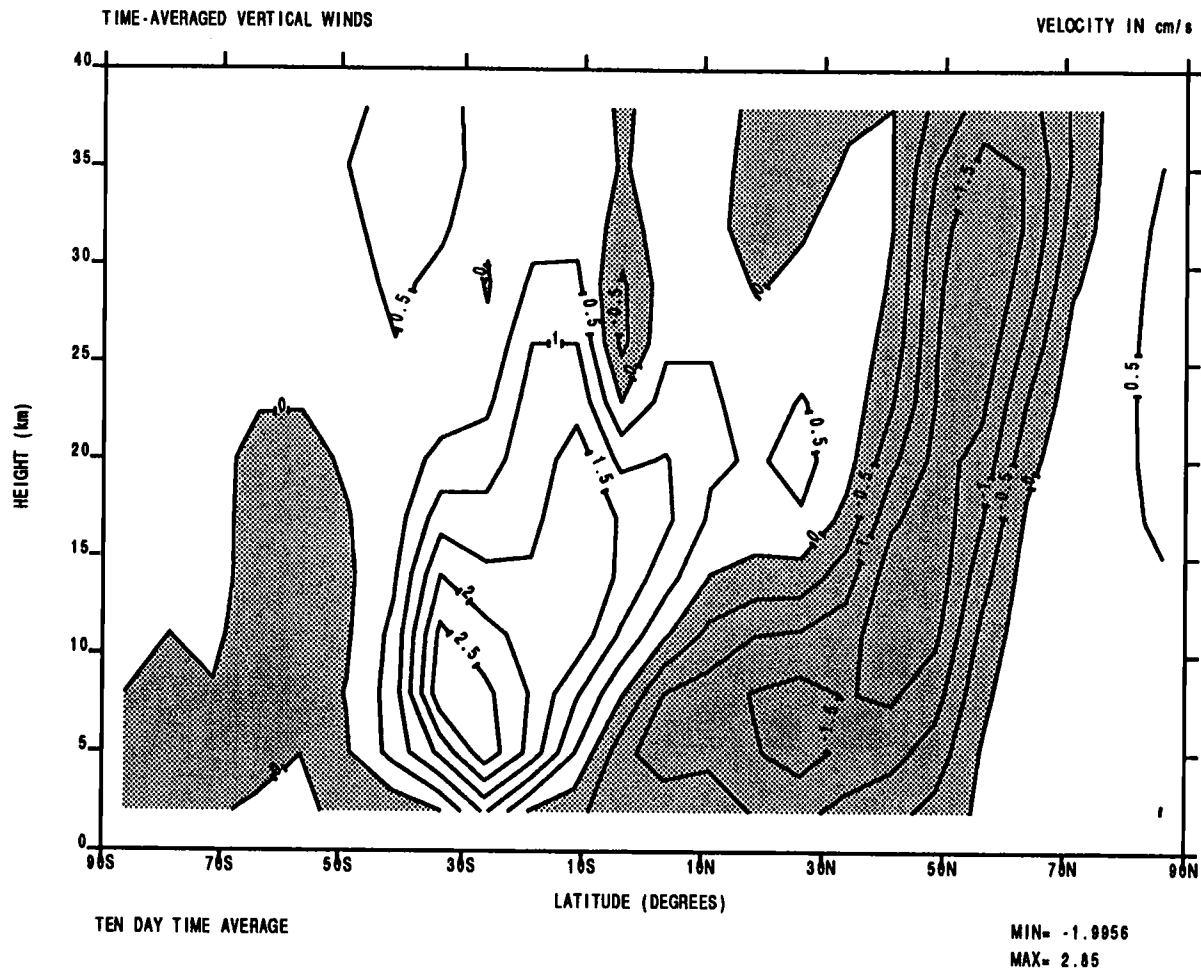


Fig. 24 Time-averaged mean vertical winds for the northern hemisphere winter solstice case with no dust loading.

“there is no analogous feature in Earth’s general circulation. The surface jet is a consequence of the meridional scale and thermal structure of the Hadley circulation. Low level air flowing toward the rising branch of the Hadley circulation from the northern hemisphere is accelerated towards the east by the Coriolis force as it crosses the equator. The farther from the equator it travels, the greater its westerly component becomes. The surface jet is closed because temperatures increase poleward in the southern hemisphere which, from the thermal wind relationship, requires an easterly shear in the zonal wind. It is worth noting that the latitudes at which this jet maximizes coincide with those from which planet-encircling storms have been observed to develop [Zurek, 1982].”

The mean meridional winds are most interesting from about 40S to 40N. This region contains strong northerly flow (~ 6 m/s) which decreases from the surface to about 5km where the winds change direction, becoming southerly, and increase with height to a maximum speed of about 5 m/s at 10 km. The winds then decrease with height again up to about 30 km where they begin to increase again. These strong meridional winds will be important contributors to the low-level equatorward flow and upper-level poleward flow of the winter Hadley cell (see Fig. 35). The remainder of the two hemispheres are characterized by weak meridional winds; predominately northerly above 5 km and southerly near the surface at mid- to high latitudes.

Examining the mean vertical winds it is seen that the strongest upward motion (~ 2.5 cm/s) is above the southern subtropics (which corresponds approximately to the subsolar point). The strongest downward motion (~ 1.5 cm/s) is found between 10N and 50N. These two bands of rising and sinking motion correspond to the rising and sinking branches of the Hadley cell as can be seen in Fig. 35. At high

latitudes in both hemispheres vertical motions are relatively weak although some rising motion is present near the north pole.

The time evolution of the tracer fields are shown in Figs. 25–32. The horizontally stratified case shown in Figs. 25–28 shows rapid mixing from about 40S to 60N. The horizontal gradient of the mean tracer field decreases quickly in this region but increases sharply in high northern latitudes at high altitudes. The vertically stratified case, seen in Figs. 29–32, also shows rapid mixing over the 40S to 60N region. The isopleths are seen to be “moving up” from 40S to 25N (indicating an expulsion of tracer) and “moving down” from 25N to 75N (indicating an intake of tracer). In general the vertical mean tracer gradient decreased over tropical and subtropical latitudes and increased over mid- and high latitudes (especially in the northern hemisphere).

These features are further brought out by considering the time-averaged mean mixing ratios in Figs. 33 and 34. The horizontal case again highlights the strong mixing in the horizontal (especially in the tropics and subtropics) while the vertical case shows the characteristic poleward-downward slope of the isopleths mentioned previously. This slope is no longer symmetric about the equator as in the equinox case but follows the rising and sinking motions of the Hadley circulation which has been displaced with the changing seasons. (At high northern latitudes of the vertically stratified case the isopleths show a poleward-upward slope which is likely the result of a Ferrell cell circulation in this region. The Mars GCM does produce a Ferrell cell in this region [Haberle et al., 1993].)

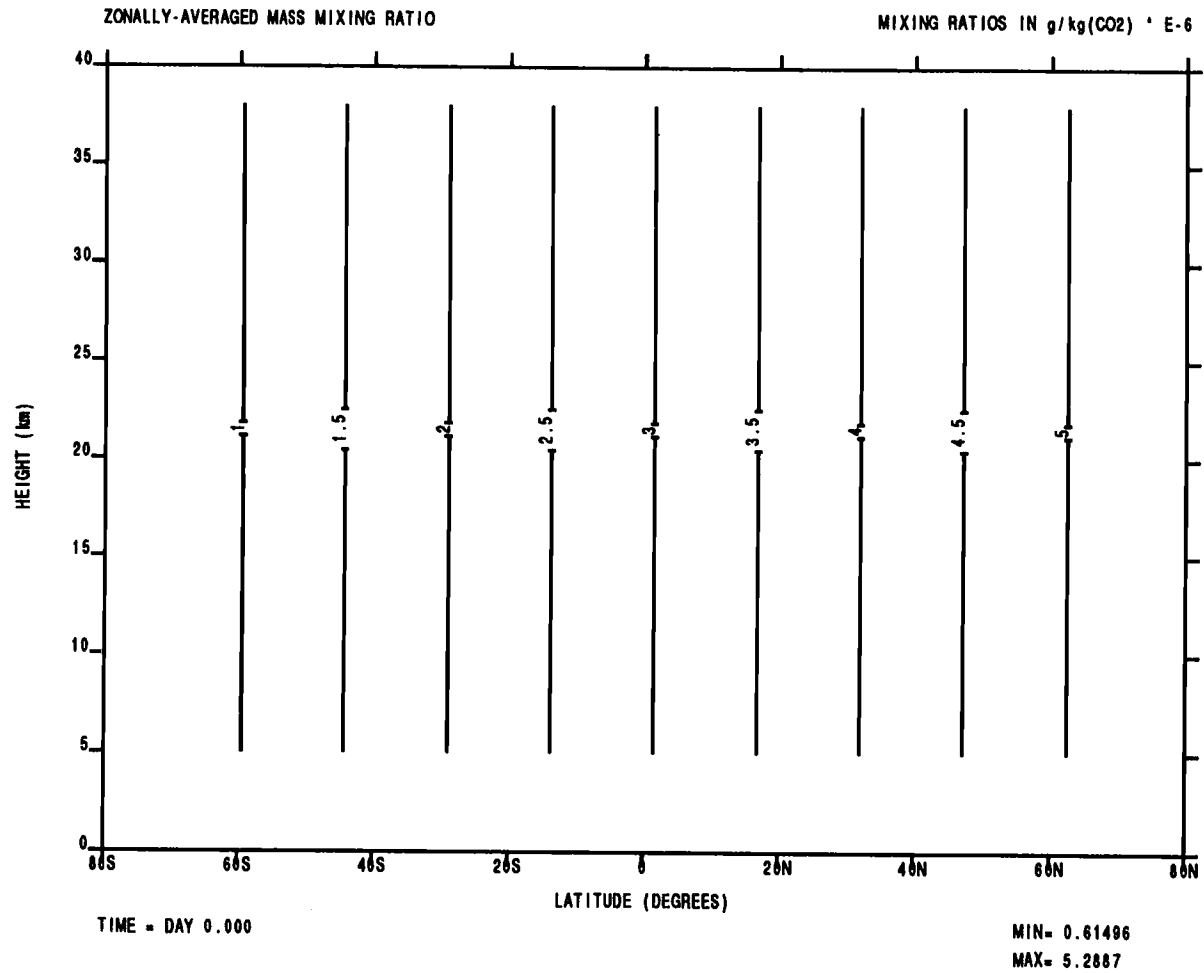


Fig. 25 Initial distribution of the mean mixing ratios for the horizontally stratified case. (NHWS, $\tau=0$)

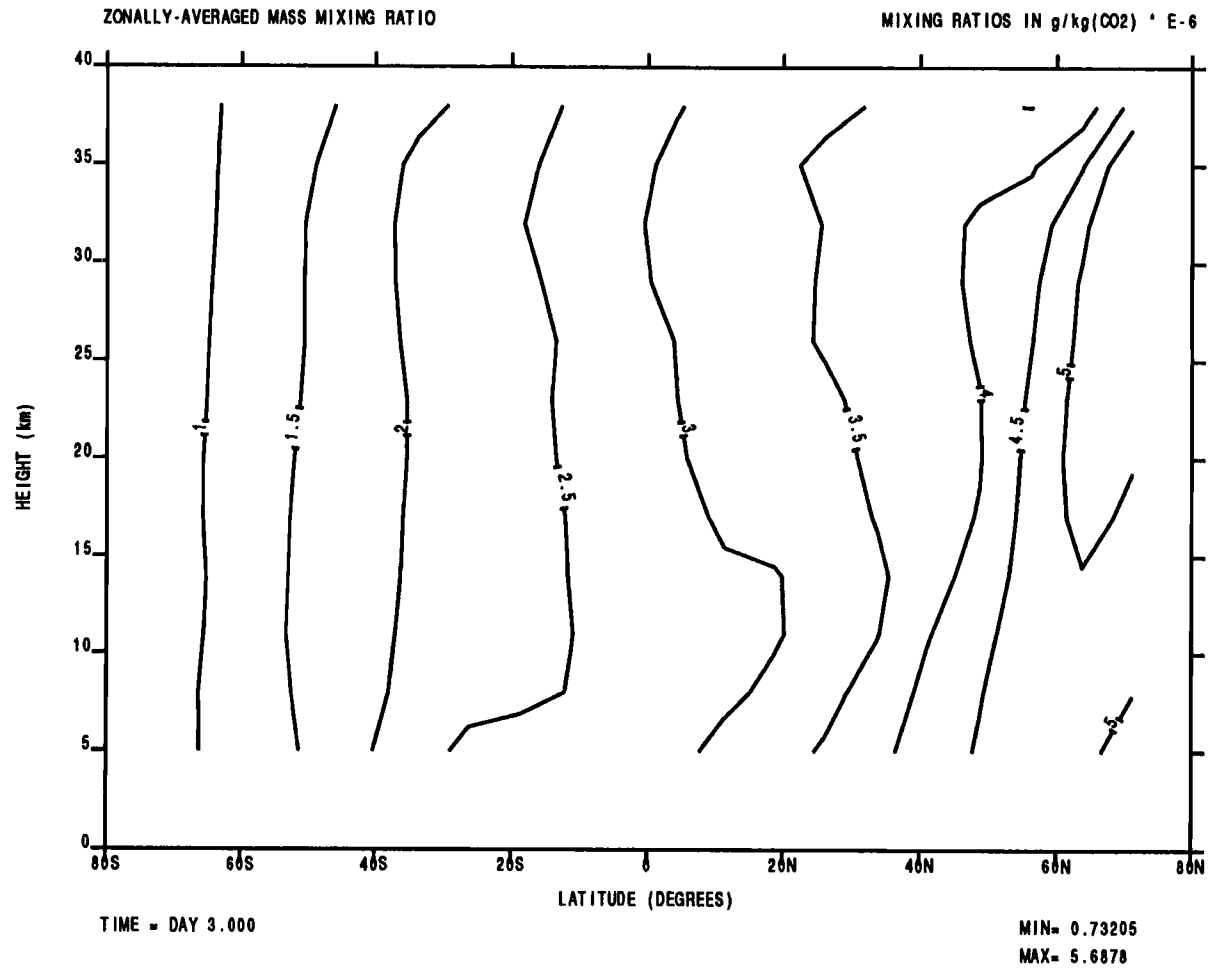


Fig. 26 Distribution of the mean mixing ratios after day 3 for the horizontally stratified case. (NHWS, $\tau=0$)

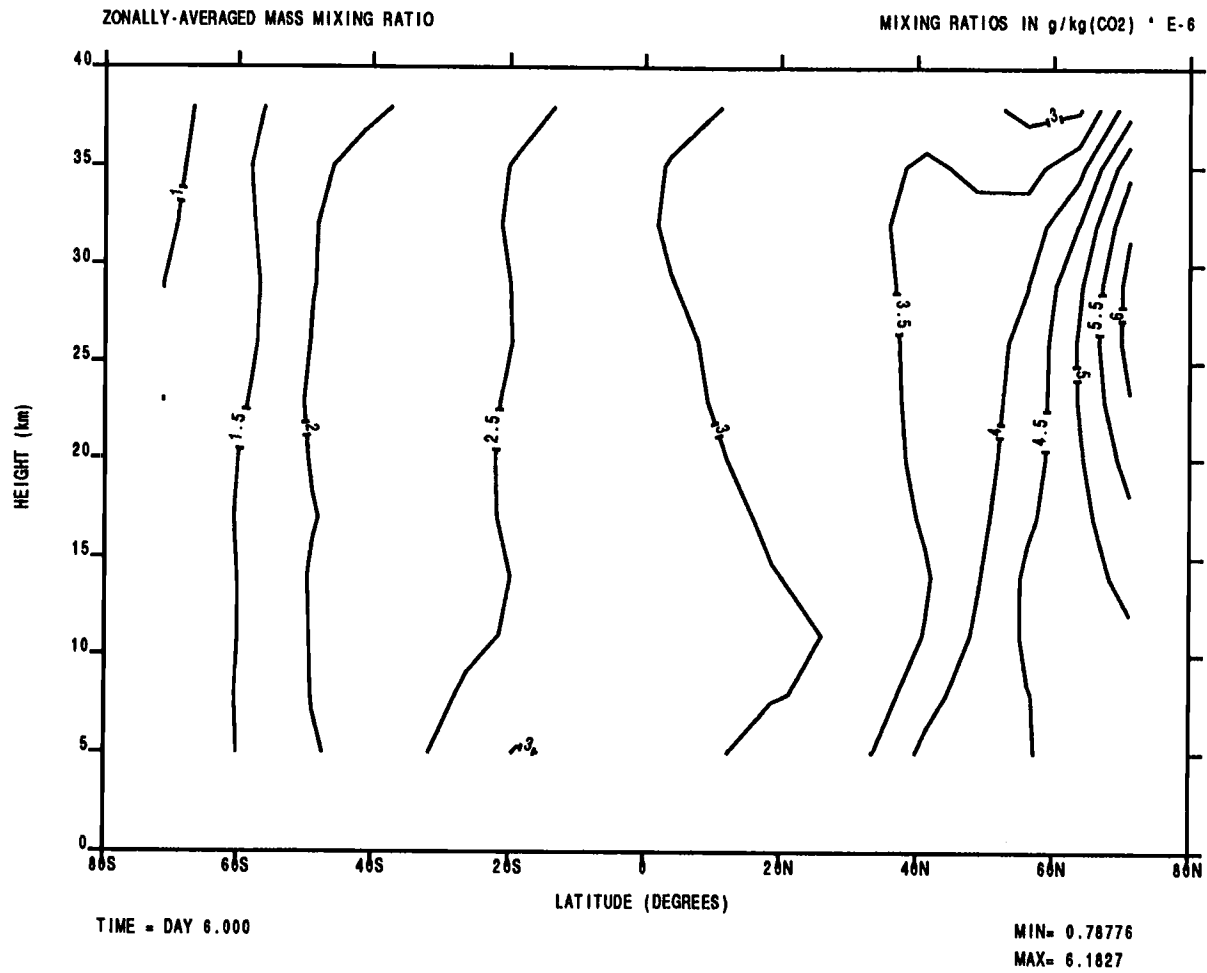


Fig. 27 Distribution of the mean mixing ratios after day 6 for the horizontally stratified case. (NHWS, $\tau=0$)

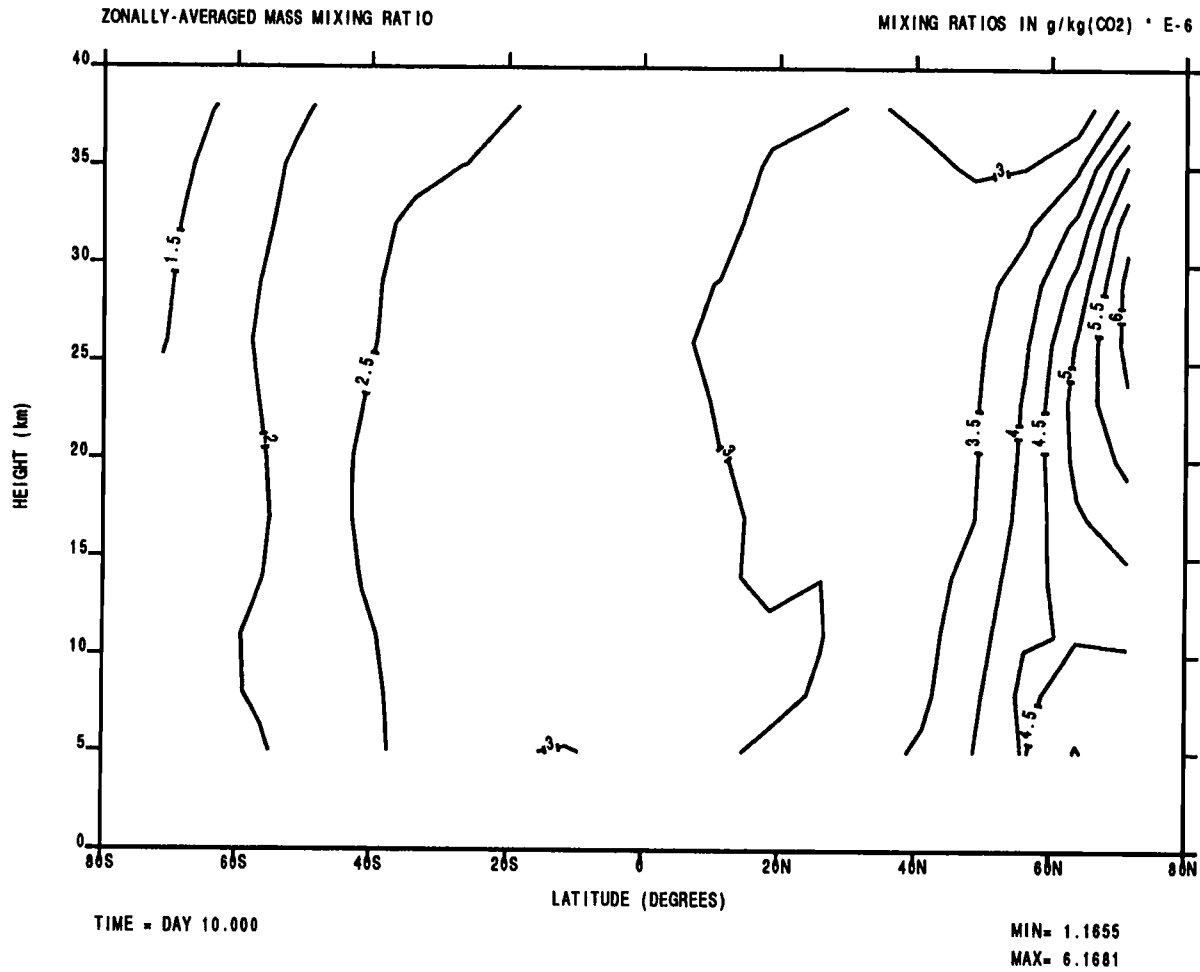


Fig. 28 Distribution of the mean mixing ratios after day 10 for the horizontally stratified case. (NHWS, $\tau=0$)

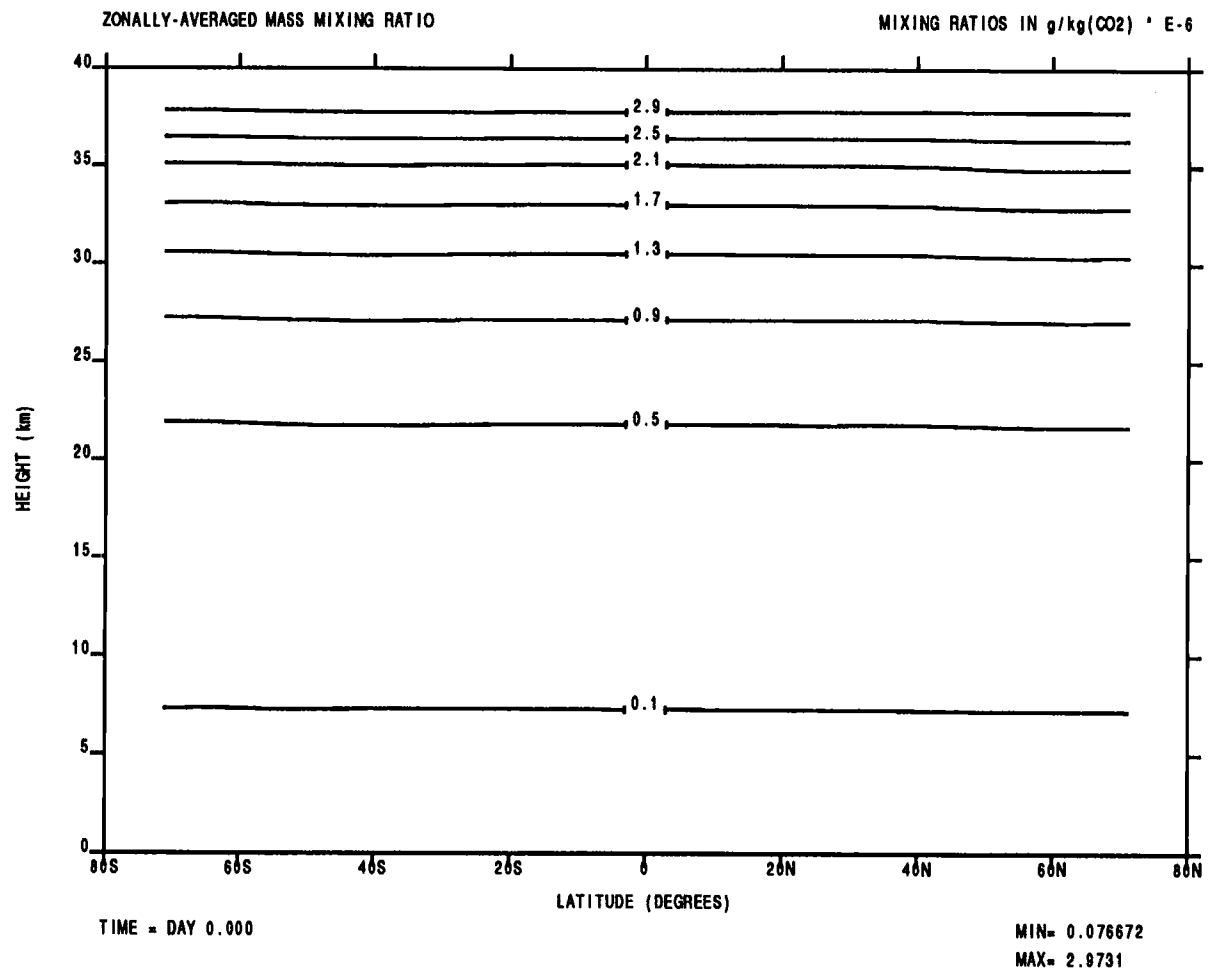


Fig. 29 Initial distribution of the mean mixing ratios for the vertically stratified case. (NHWS, $\tau=0$)

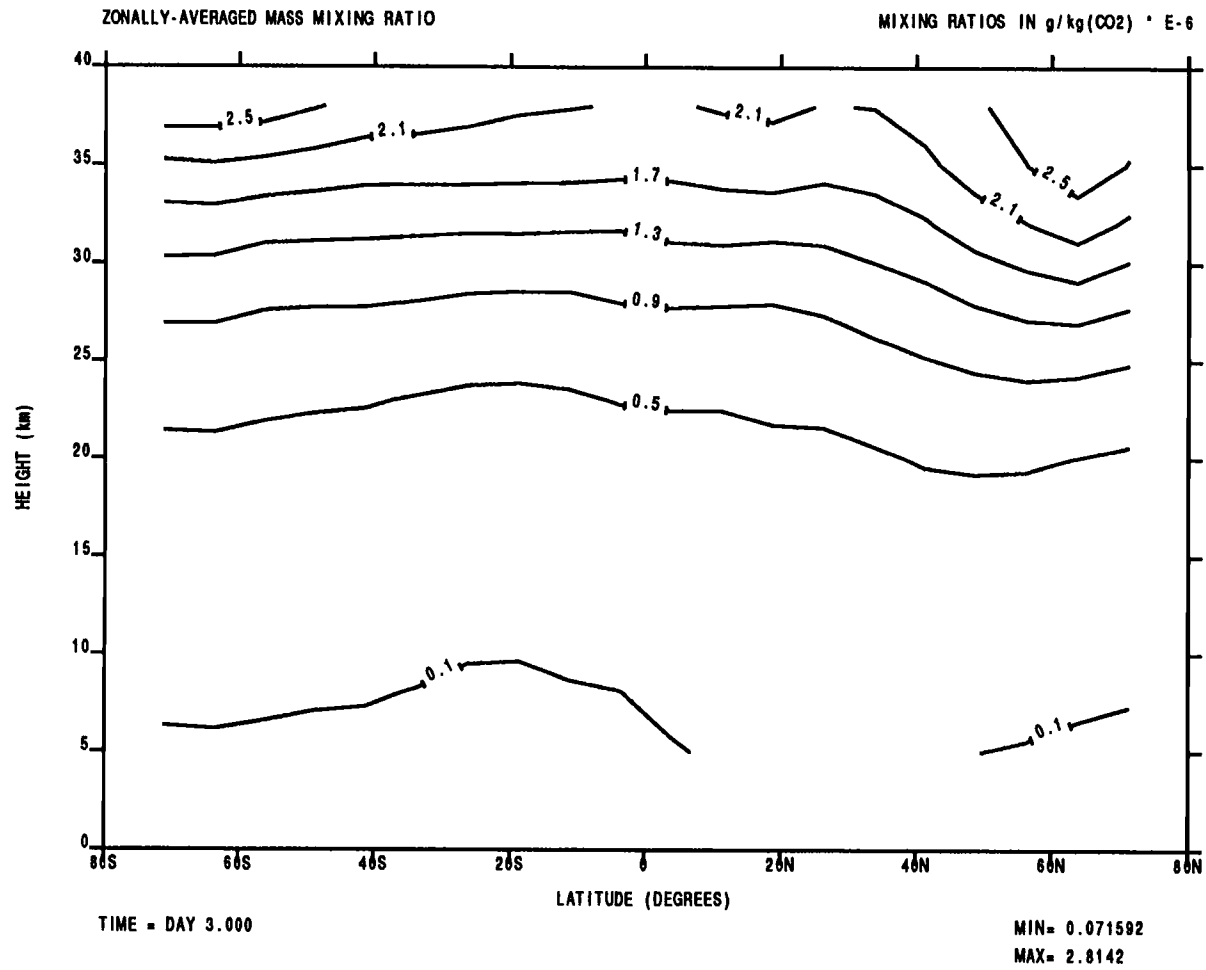


Fig. 30 Distribution of the mean mixing ratios after day 3 for the vertically stratified case. (NHWS, $\tau=0$)

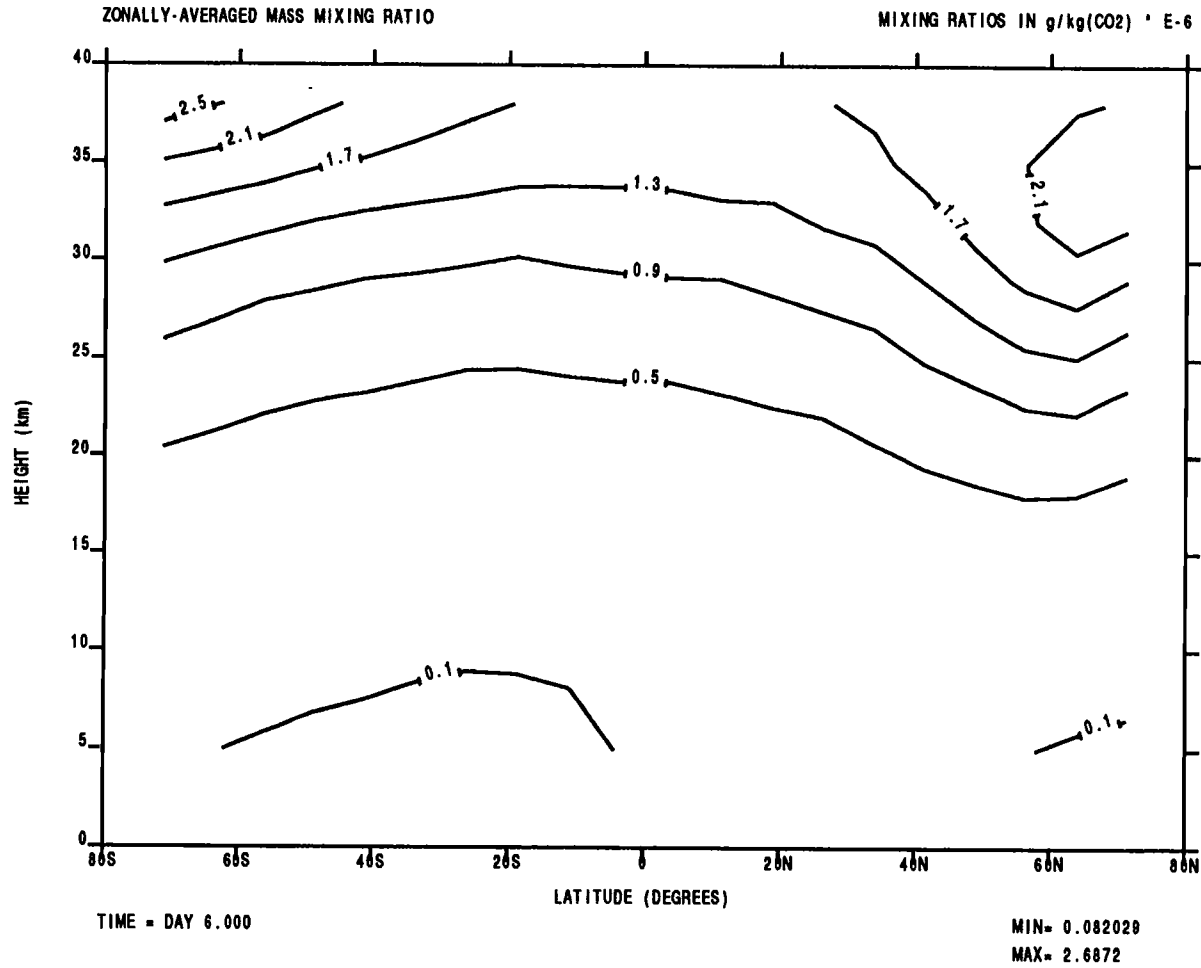


Fig. 31 Distribution of the mean mixing ratios after day 6 for the vertically stratified case. (NHWS, $\tau=0$)

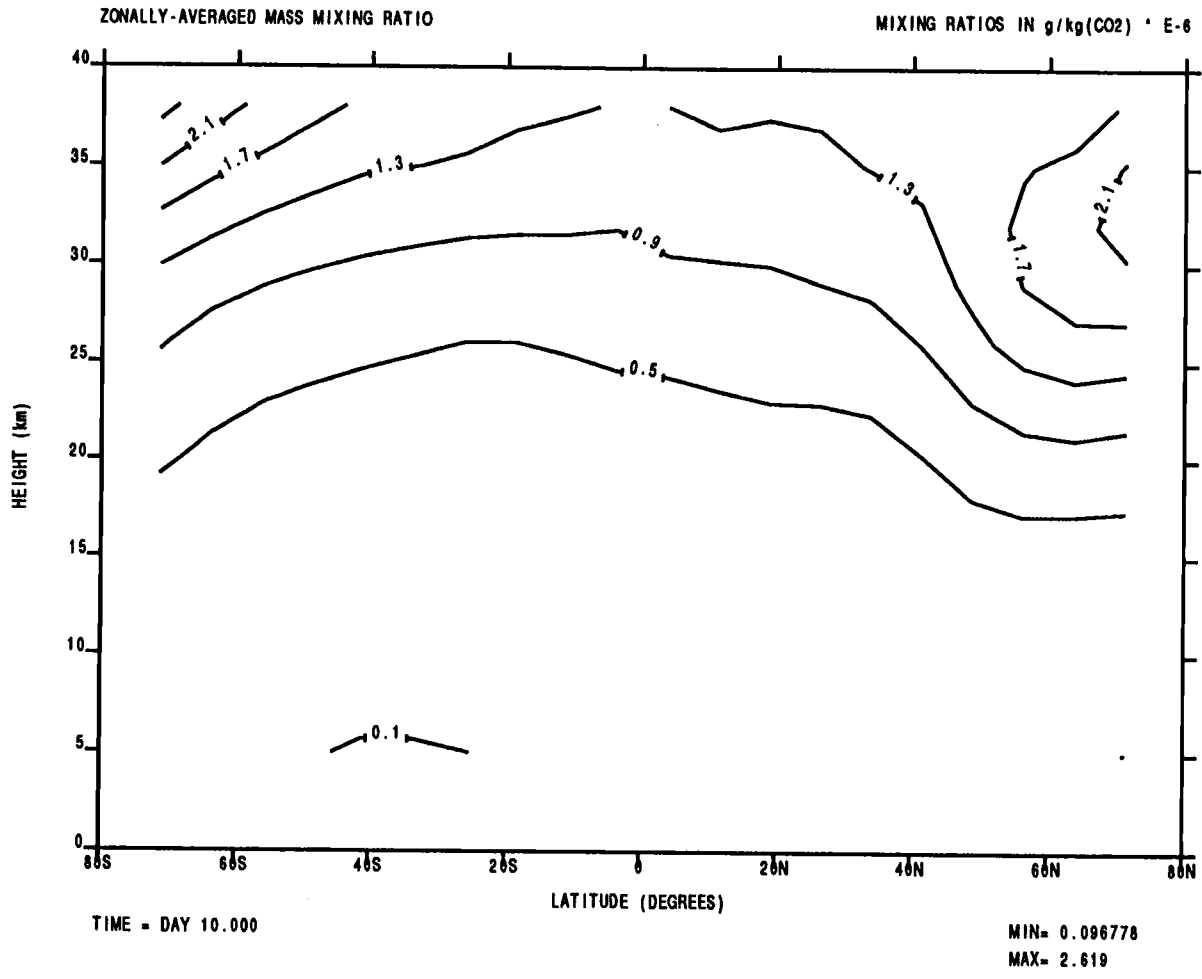


Fig. 32 Distribution of the mean mixing ratios after day 10 for the vertically stratified case. (NHWS, $\tau=0$)

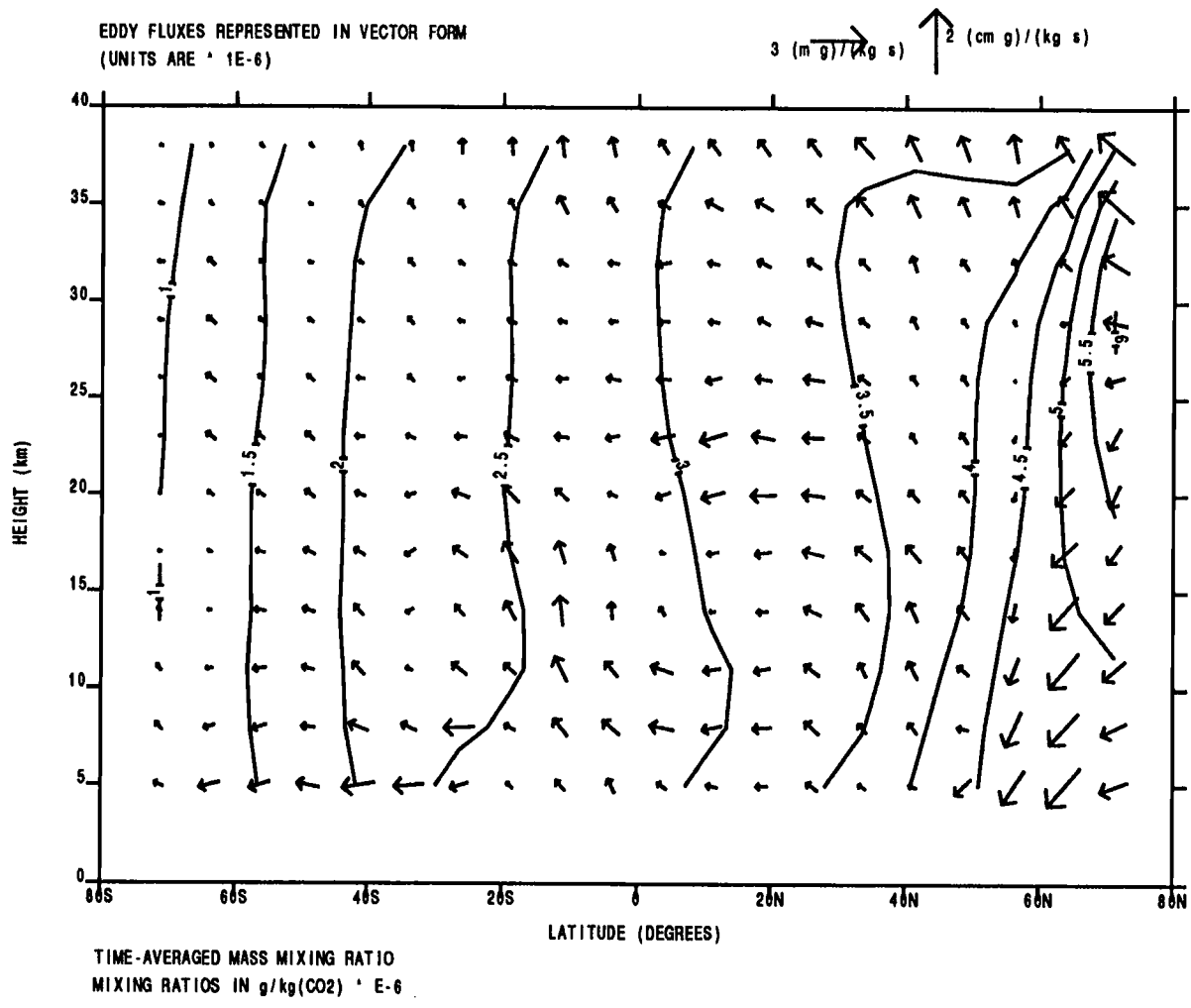


Fig. 33 Time-averaged mean mixing ratios and eddy fluxes for the horizontally stratified case. (NHWS, $\tau=0$)

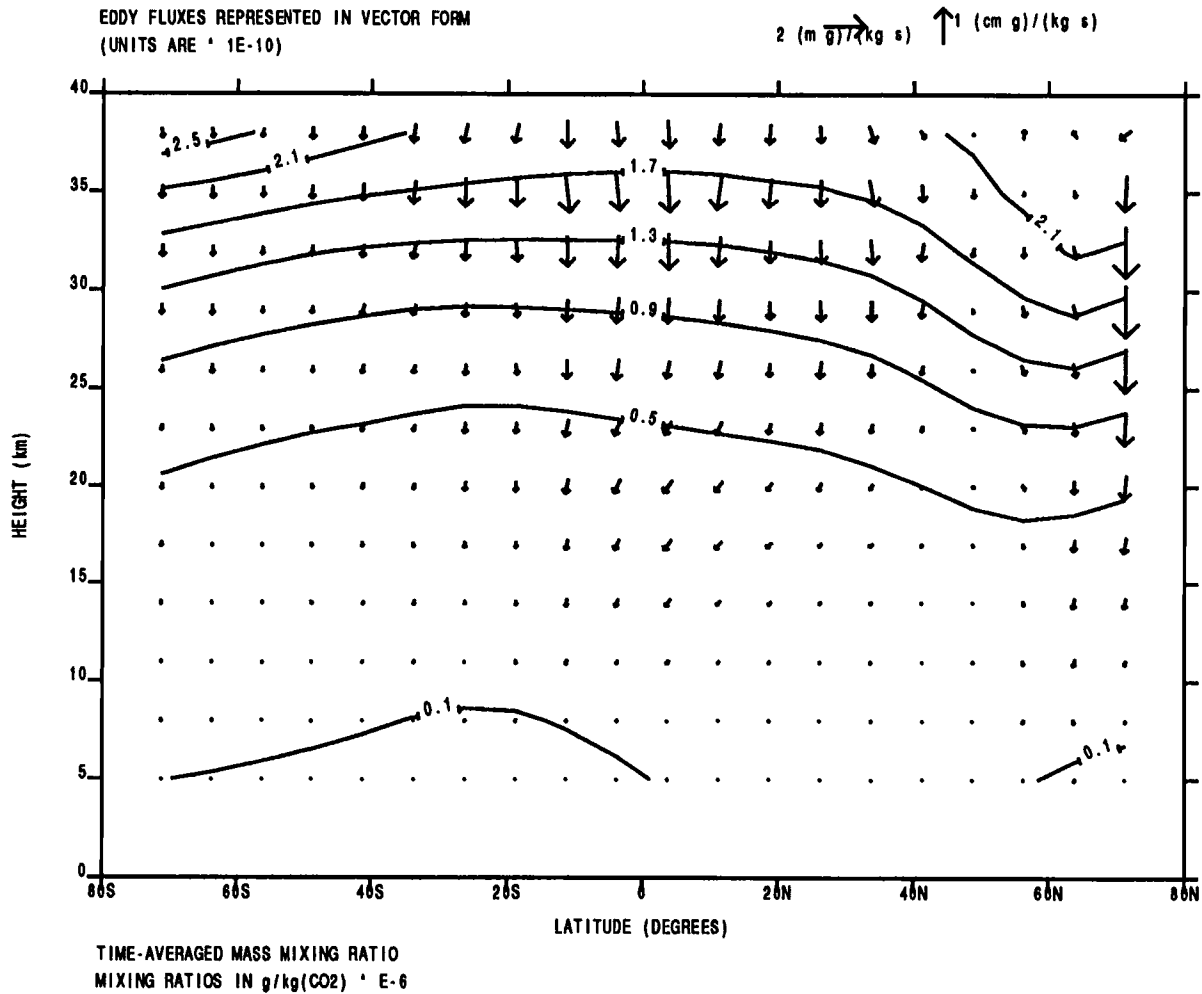


Fig. 34 Time-averaged mean mixing ratios and eddy fluxes for the vertically stratified case. (NHWS, $\tau=0$)

Concentrating on the eddy fluxes shown in Figs. 33 and 34, it is again observed that most of the fluxes are directed downgradient as expected for diffusive-type eddy transport. This is especially true for the vertically stratified case with the exception of a few regions above northern low to mid- latitudes where the fluxes are less cross-contour. The horizontally stratified case has a small region in northern mid- to high latitudes and a small region at low altitudes above the southern tropics where the fluxes are much less cross-contour indicating advective-type eddy diffusion.

The structure of the mean meridional circulation is shown in Fig. 35. The most identifiable feature is the large, strong, cross-equatorial Hadley cell with rising and sinking branches centered at 30S and 40N, respectively. The cell extends from the surface to the top of the model and is most intense between 5 and 20 km. Barely observable (due to its small size and strength) is another Hadley cell at high southern latitudes. Haberle et al. [1993] also observed this feature noting that

“the profound asymmetry in the size, strength, and position of the two Hadley cells is due to the fact that the peak heating is located well off the equator [Lindzen and Hou, 1988]. Indeed much of the rising motion occurs poleward of the subsolar point ($\sim 25^\circ$ S). This asymmetry is much more pronounced than it is for Earth’s Hadley circulation because of the small heat capacity of Martian soil. On Earth, the oceans act as large thermal reservoirs that buffer the seasonal swing in the latitude of the rising branch.”

Also identifiable in the results is a thermally indirect Ferrell cell at high northern latitudes (from 50N poleward).

The Ferrell cell observed in the mean meridional circulation is not observed in the transport circulation shown in Fig. 36. The transport circulation is essentially

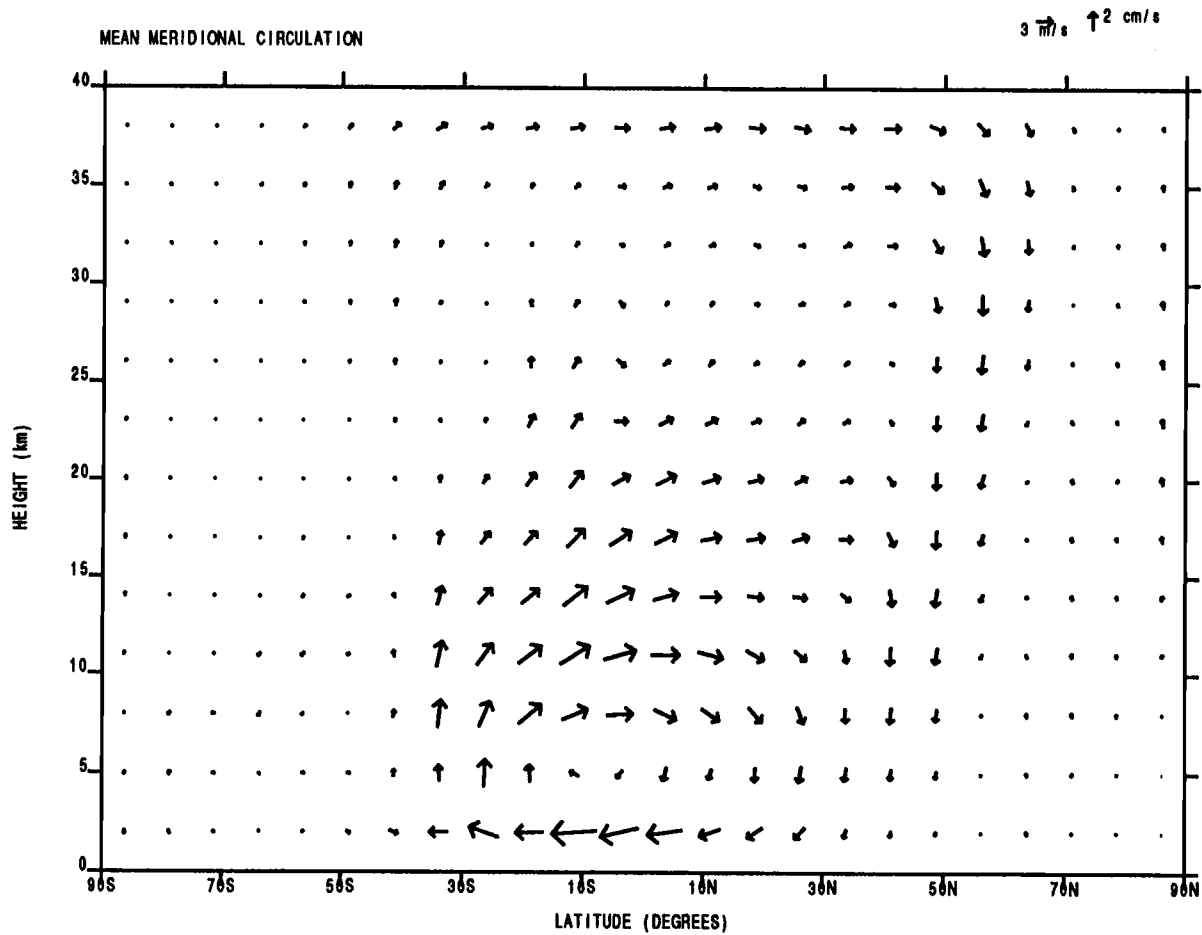


Fig. 35 Mean meridional circulation for the northern hemisphere winter solstice case ($\tau=0$).

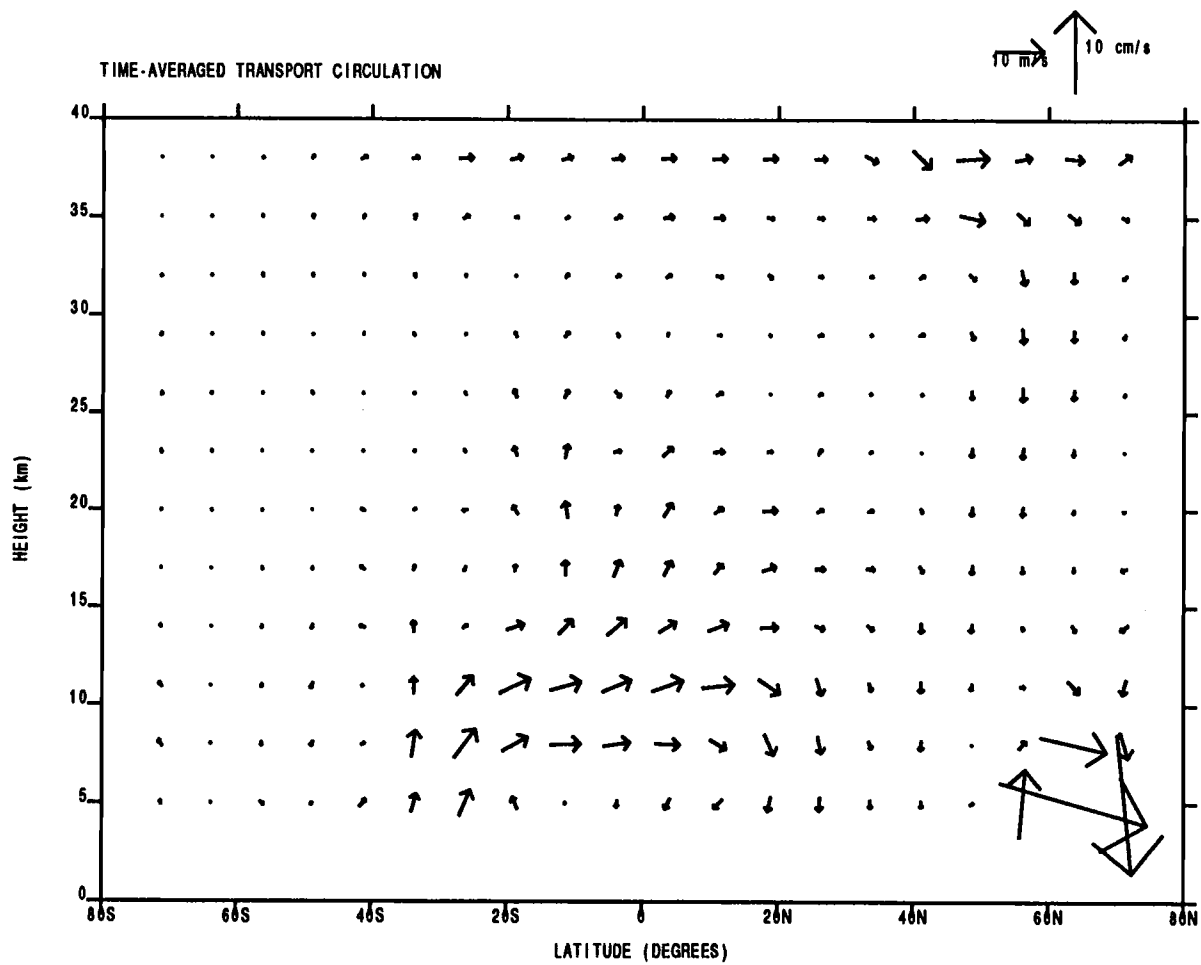


Fig. 36 Effective transport circulation for the northern hemisphere winter solstice case ($\tau=0$).

characterized by a single large cross-equatorial Hadley cell whose strongest motions are found between 30S and 30N at low levels (and at high northern latitudes near the ground). However, the vector plot does show evidence of a very weak Hadley circulation in the mid- to high latitudes of the southern hemisphere at low altitudes. The transport circulation is simpler than the mean meridional circulation since the Ferrell cell is not present. This result is in agreement with expectations based on the work of Plumb and Mahlman [1987]. They showed that the transport circulation, \vec{U}_T , is related to the residual and Lagrangian-mean circulations and thus, "in accord with theoretical expectation, . . . the successful cancellation of the Ferrell cell lends credibility to the calculation."

Comparing the transport circulation with the distribution of calculated diffusivities (see Figs. 37 and 38) it is again observed that the largest transport vectors are found in regions of large diffusivities. The low level tropics and subtropics and low levels between 50N and 80N highlight this feature. (In plotting K_{yy} and K_{zz} less than two percent of the data points were affected by the "quality control" scheme.) For K_{yy} the largest values are concentrated in two main regions. First, there is a band which begins at low levels in the southern subtropics and tropics and stretches upward (up to 25 km) above the northern subtropics. The typical horizontal eddy coefficient here is $3-5 \times 10^6 \text{ m}^2/\text{s}$. The second main region is found at high northern latitudes near the ground and exhibits the largest values of K_{yy} , up to $40 \times 10^6 \text{ m}^2/\text{s}$.

In the band of strong mixing stretching across the tropics and subtropics of both hemispheres there are two noticeable correlations with the zonal wind lines.

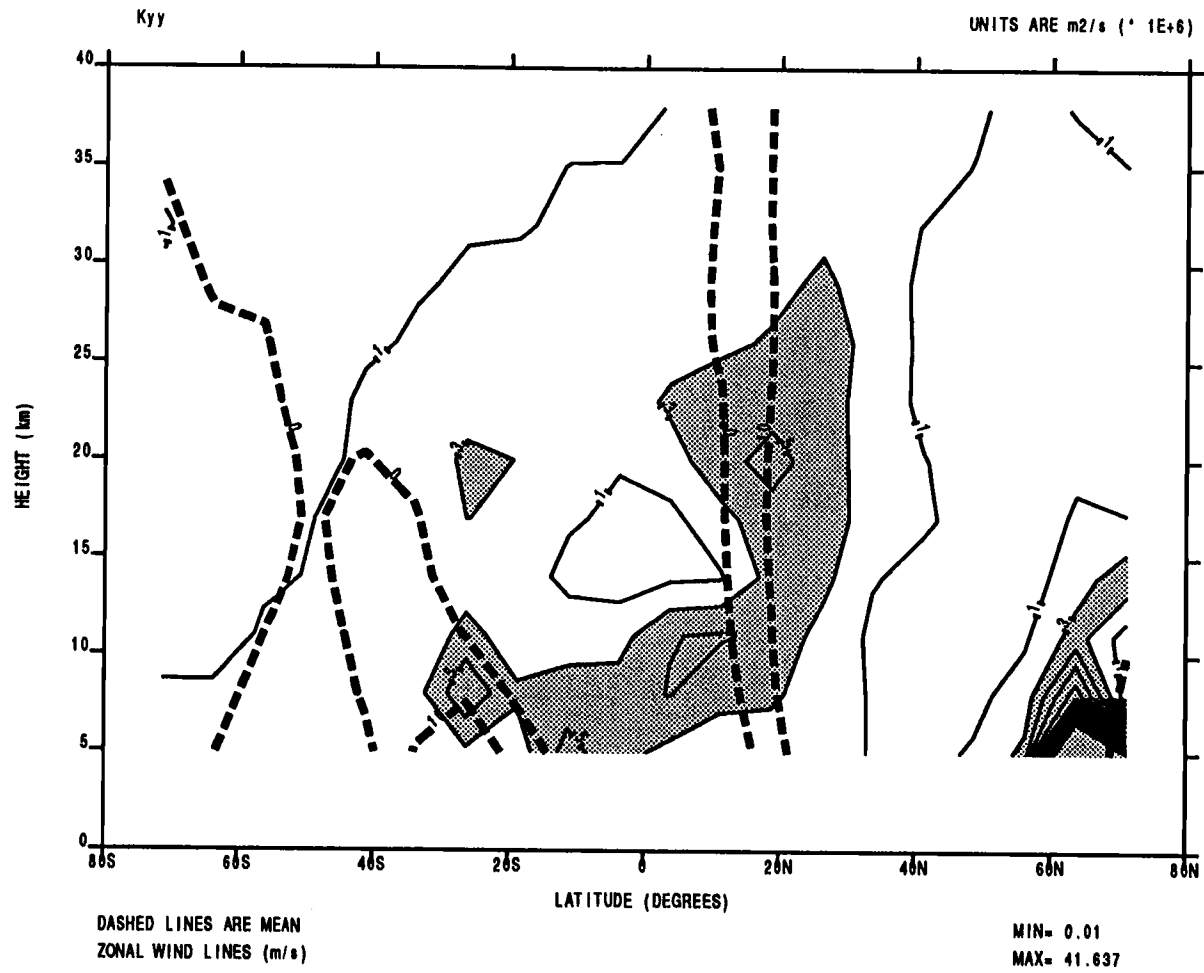


Fig. 37 Distribution of K_{yy} , the horizontal eddy diffusion coefficient. (NHWS, $\tau=0$)

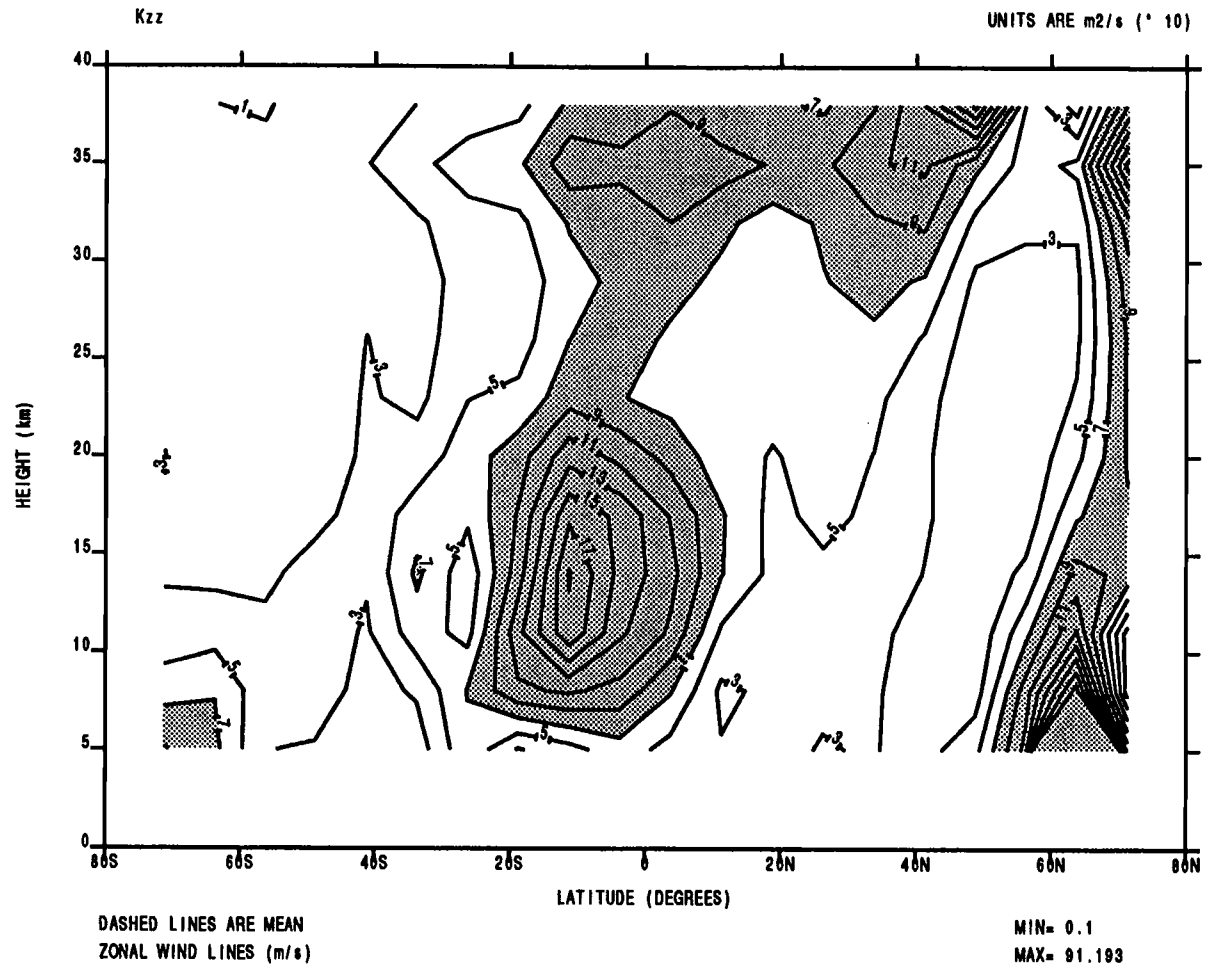


Fig. 38 Distribution of K_{zz} , the vertical eddy diffusion coefficient. (NHWS, $\tau=0$)

Looking closely at the portion of the band at low levels in the southern subtropics it is seen that there is a correlation with the zero wind line. This suggests that this region of mixing may be influenced by stationary planetary waves resulting from the high topography at these latitudes; this is also the region of the subtropical jet. The region of strong horizontal mixing at mid-levels above the northern subtropics is likely the result of breaking transient and/or quasistationary waves as suggested by the correlations with the zero and 10 m/s zonal wind lines. The tides are not expected to influence horizontal mixing significantly, especially in this region, so their contribution is probably small.

In the high northern latitudes it is suspected that the mixing is due to the transient eddies associated with mid- to high latitudes. The values of K_{yy} in this region are an order of magnitude greater than those observed in the equinox case which is likely the result of the increase in intensity of the synoptic eddies in the northern hemisphere in the winter season. (This also explains why a similar region of strong horizontal mixing is not observed in middle and high southern latitudes during summer. The southern latitudes show a marked decrease overall in diffusive mixing since the transient eddy activity has strongly decreased.)

The most prominent regions of mixing associated with K_{zz} are found above the southern tropics and subtropics between 5–20 km, at high levels of the northern hemisphere, and at mid- to high latitudes of the northern hemisphere from the surface to the top of the model. The typical values of K_{zz} at mid-levels above the equator are 70–170 m^2/s . This region is likely to be most strongly influenced by the tides but could have a significant contribution also from planetary waves. The

strong vertical mixing observed at the top of the model is again likely the result of the diurnal tides as discussed for the equinox case. The largest values of K_{zz} approach $900 \text{ m}^2/\text{s}$ and are located near the ground at northern mid-latitudes. The band of strong vertical mixing found here is believed to be the result of the vigorous transient eddy activity in this region. As for K_{yy} for northern winter solstice, K_{zz} shows a significant increase in magnitude (from 2 up to 10 times) as compared to the equinox the equinox case. This again is attributable to the more intense global circulation associated with solstice conditions.

Figs. 39–41 (provided by J. Barnes, 1994, personal communication, for the identical L_s span) lend support to the previous assertions as to the sources of the eddy mixing. Filtered plots were unavailable to isolate the transient and diurnal time scales, but some insight may still be gathered from these plots. Fig. 39 is the transient rms geopotential height variance which shows a maximum in the mid- to high latitudes between the ground and the top of the model. This implies vigorous transient eddy activity in this region and coincides with the areas of strong mixing (both horizontal and vertical) in these latitudes.

The stationary rms temperature variance shown in Fig. 40 shows maximum values near the ground between 50S and 30N. This suggests the potential for stationary waves to influence mixing at low levels in the equatorial regions. Fig. 41 is the transient rms temperature variance which highlights large variance at low levels and high levels. The variance at high levels is indicative of the influence of the thermal tides in this region. This supports the assertion that the tides are the likely source for the strong vertical mixing at high altitudes in Fig. 38.

23A TRANSIENT RMS GEOP. HT. VARIANCE (m)

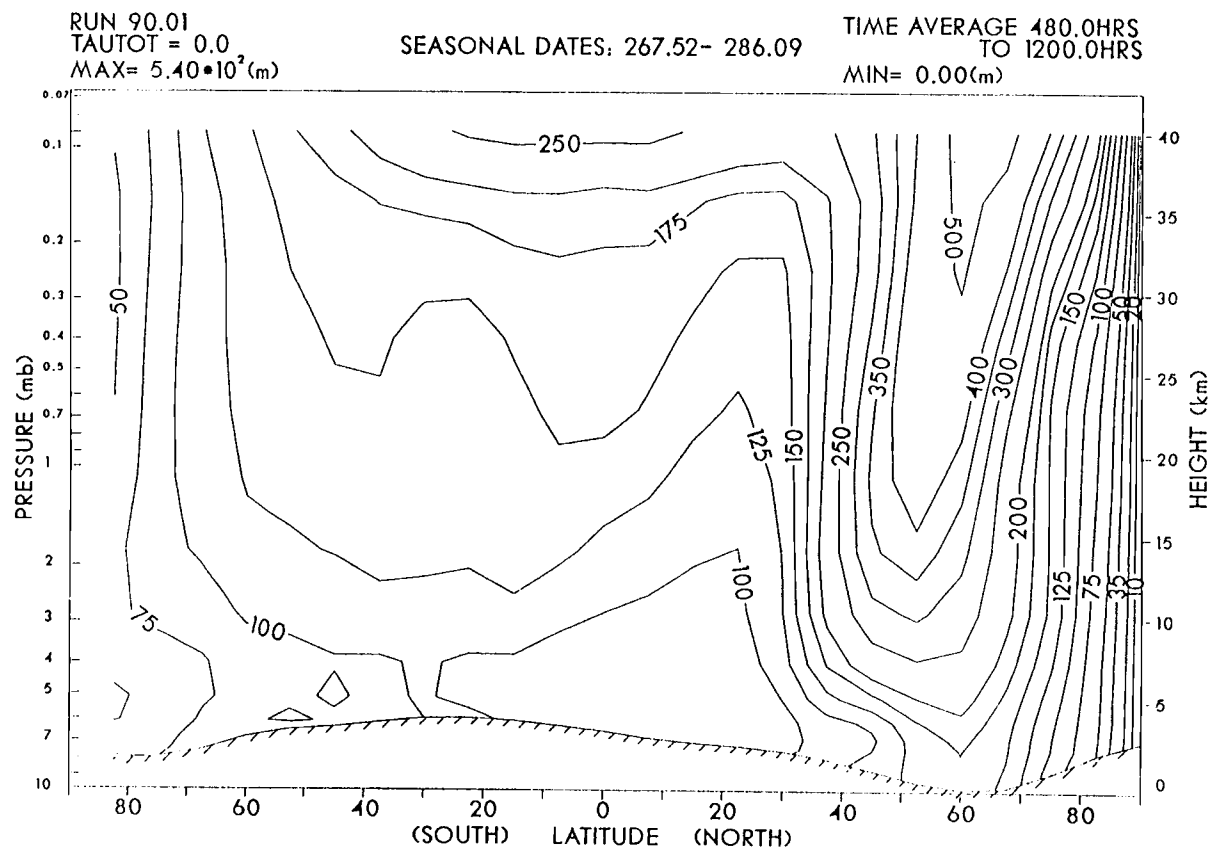


Fig. 39 Distribution of the transient rms geopotential height variance indicating regions of significant transient eddy activity.

24B STATIONARY RMS

TEMP. VARIANCE ($^{\circ}\text{K}$)

RUN 90.01
TAUTOT = 0.0
MAX= $6.16 \cdot 10^0$ ($^{\circ}\text{K}$)

SEASONAL DATES: 267.52- 286.09

TIME AVERAGE 480.0HRS
TO 1200.0HRS
MIN= 0.00 ($^{\circ}\text{K}$)

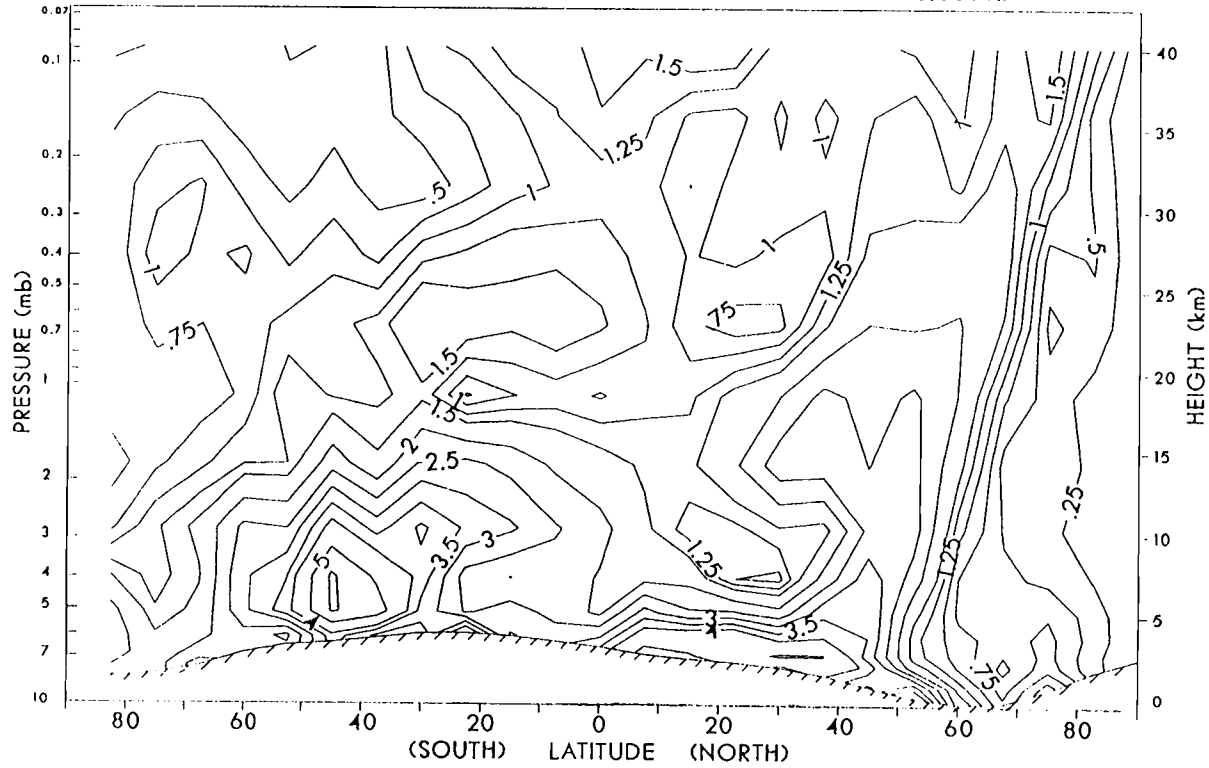


Fig. 40 Distribution of the stationary rms temperature variance indicating regions of significant stationary eddy activity.

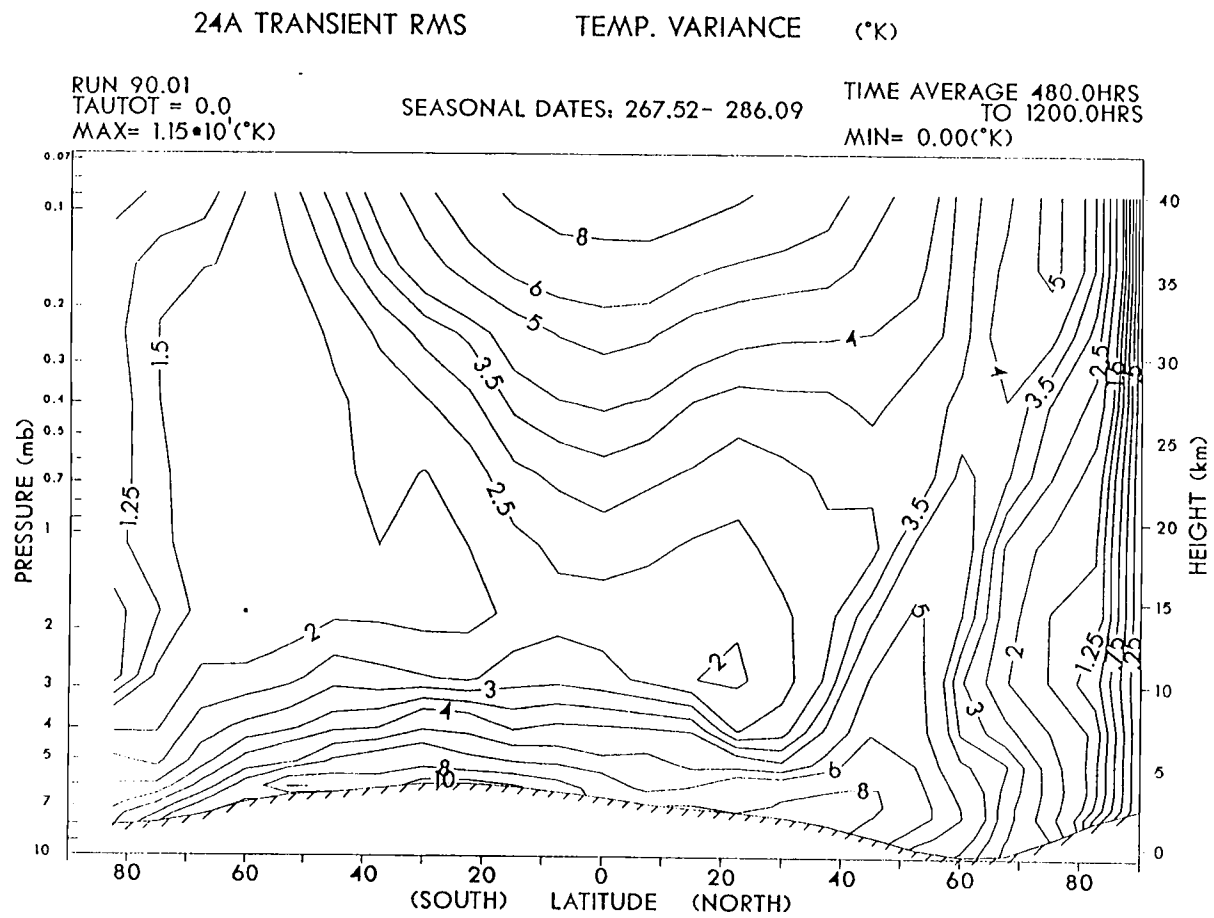


Fig. 41 Distribution of the transient rms temperature variance showing influence of the thermal tide.

4.3 Experiment 3: Northern Winter Solstice (with dust)

This case is identical to Case 2 ($L_s = 255^\circ$ – 286°) except that the optical depth, τ , has been set equal to 1.0 in order to simulate an atmosphere under dusty conditions. This experiment is of interest since it gives a glimpse of the dynamical effects of dust in the atmosphere. In addition, it is during this season that planet-encircling dust storms tend to occur. (A value of $\tau = 1.0$ represents moderately dusty conditions. It is known that the optical depths observed at the Viking lander sites reached values that were significantly greater than 1.0 [Colburn et al., 1989] and that global mean optical depths inferred from tidal signatures in the pressure data were also much larger than 1.0 [Zurek, 1981].)

The influence of dust in the atmosphere is very apparent in the mean winds. Comparing these winds (shown in Figs. 42–44) with those from Case 2 (as seen in Figs. 22–24), it is seen that the biggest change is in the intensity of the winds. The maximum speeds of the zonal winds have nearly doubled while those in the meridional and vertical directions have increased from 3 to 4 times their values under clear conditions. The maximum zonal winds are now up to 175 m/s in the westerly jet while meridional and vertical wind speeds exceed 20 m/s and 7 cm/s, respectively.

Very little structural differences are seen in the mean winds. The zonal winds are still characterized by westerlies dominating the northern hemisphere, surface westerlies in the southern subtropics, and easterlies dominating the southern hemisphere. The most noticeable changes are the prevalence of easterlies in high southern latitudes and the more pronounced westerly jet at high levels in the

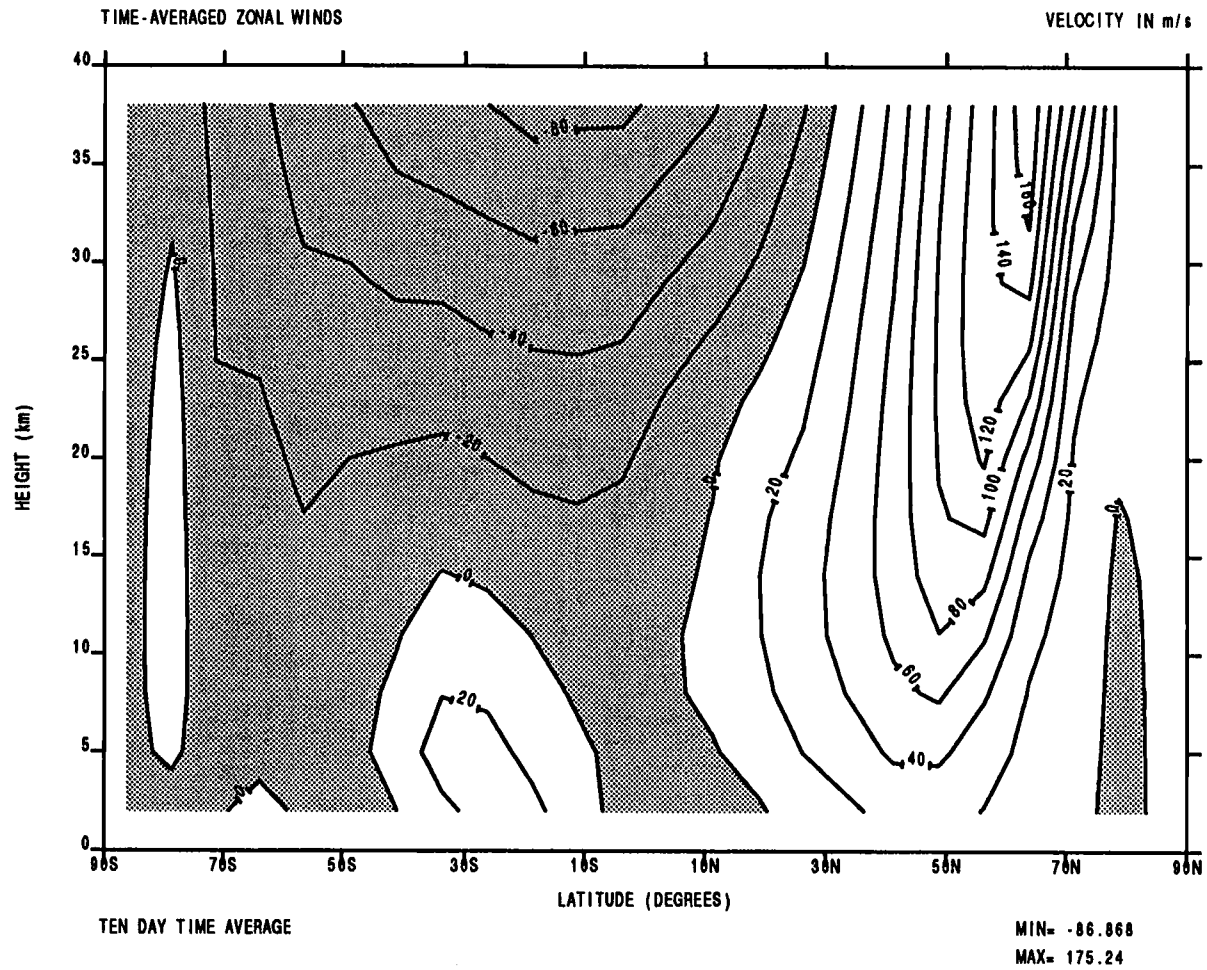


Fig. 42 Time-averaged mean zonal winds for northern hemisphere winter solstice (with $\tau=1.0$).

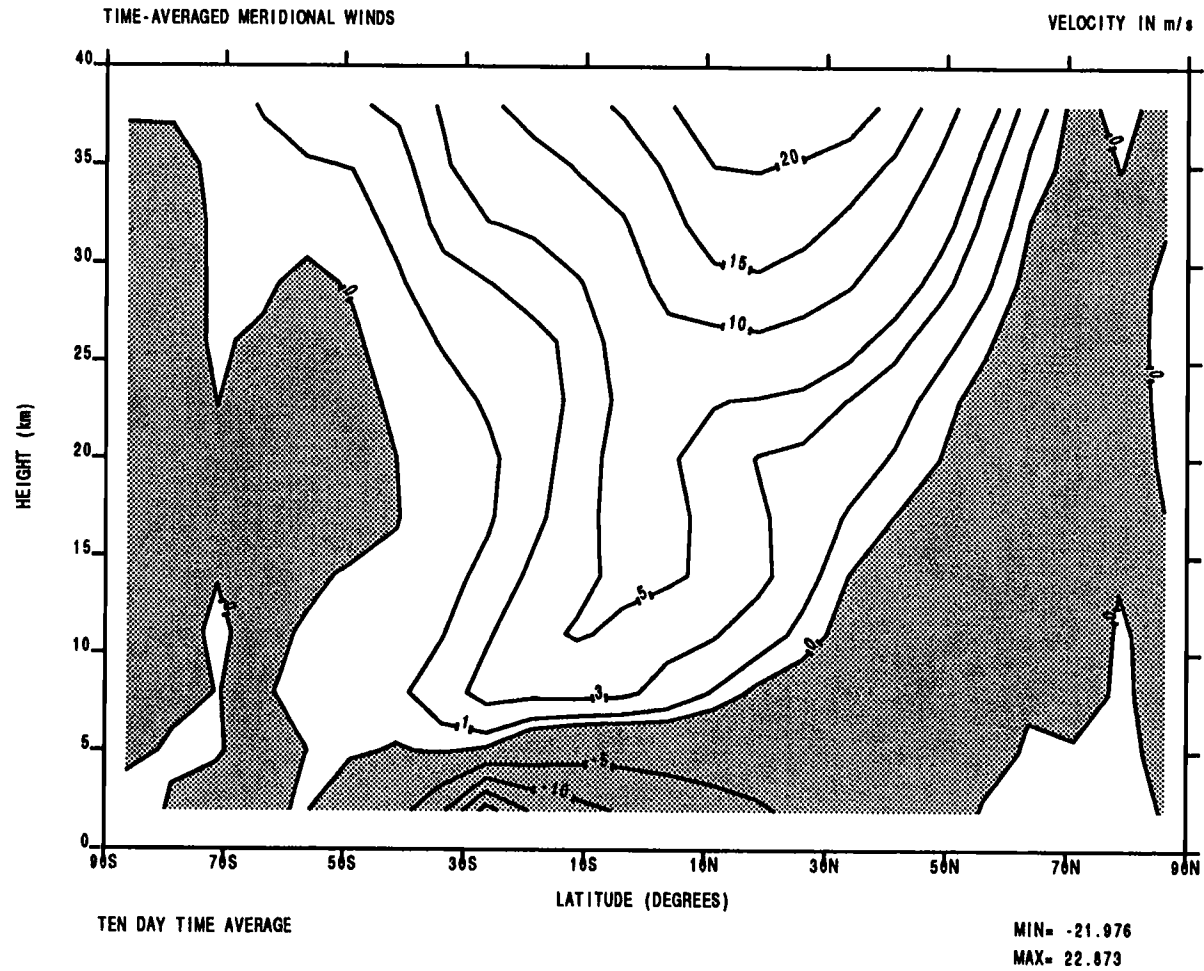


Fig. 43 Time-averaged mean meridional winds for northern hemisphere winter solstice (with $\tau=1.0$).

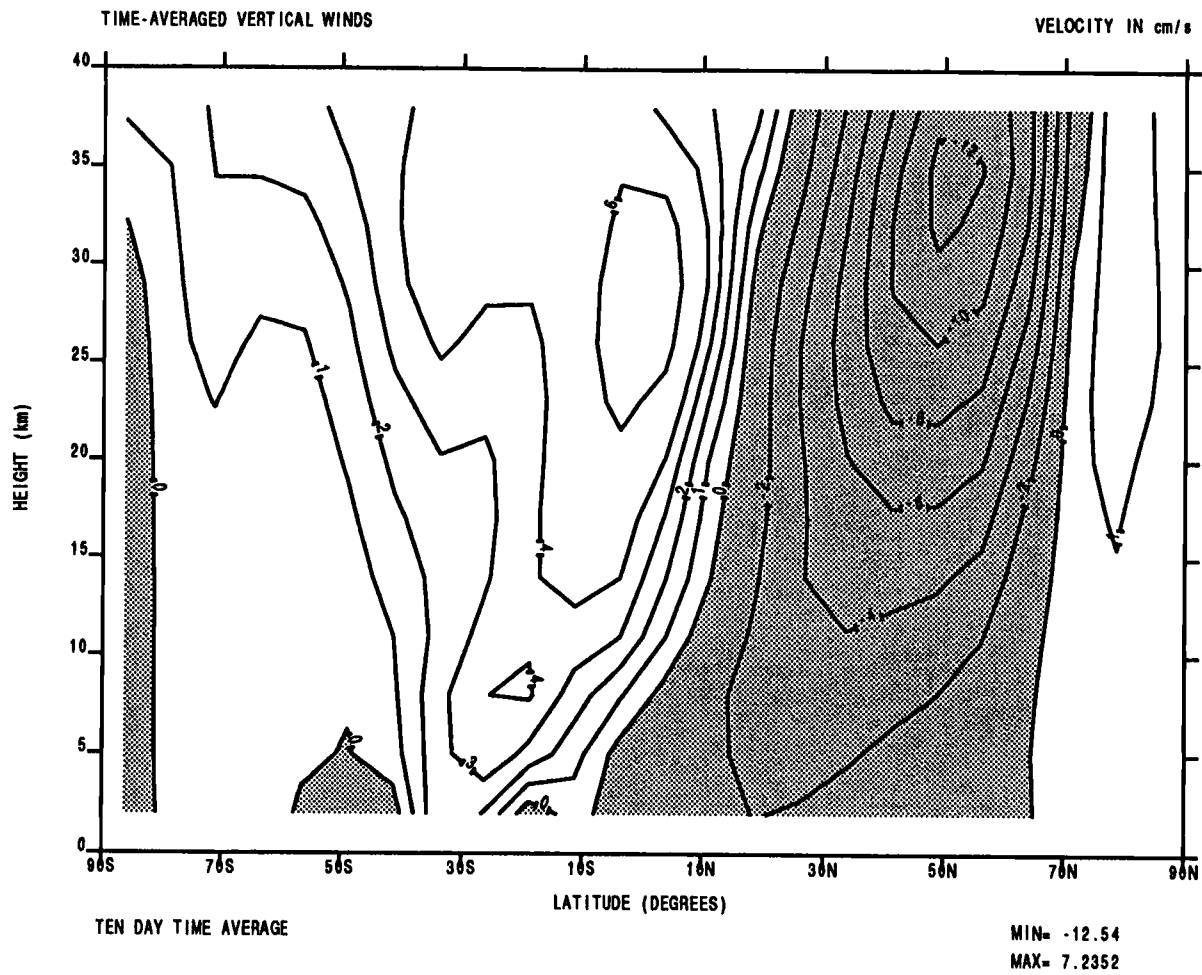


Fig. 44 Time-averaged mean vertical winds for northern hemisphere winter solstice (with $\tau=1.0$).

northern mid-latitudes. The meridional wind structure remains basically the same for the dusty case except that the southerly winds which begin at 5 km above the equatorial regions increase continuously to the top of the model (as opposed to increasing, decreasing, and then increasing again as in Case 2). The mean vertical winds show the largest structural change. Under dusty conditions the bands of rising and sinking motion are more confined horizontally and exhibit a degree of symmetry about the zero wind line above the equator. These winds are characterized by a thin band of weak sinking motion from the southern pole to 85S, relatively strong rising motion from about 85S to 10S, relatively strong sinking motion from 10S to 65N, and then a band of weak rising motion from 65N to the northern pole. In all three plots the increase in wind speed is associated with increased horizontal and vertical wind shears.

The increase in the intensity in the intensity of the mean winds from Experiment 2 to Experiment 3 can be explained as a result of the radiative effects of dust. Dust is a good absorber of the incoming solar radiation. When it is suspended in the atmosphere it directly heats the atmosphere increasing the atmospheric temperatures as well as the meridional temperature gradients (see Haberle et al., 1993). Thus, as expected, the winds increase in intensity according to the thermal wind relationship.

A closer examination of the mean meridional and vertical winds for this case suggests that the mean meridional circulation is very well defined. This is due to the distinct regions of different wind direction and the increased strength of the winds. The four components of flow in the large, cross-equatorial Hadley cell are readily identifiable in these plots: the strong rising and sinking motions centered at 30S and 40N, respectively, the strong upper level (southerly) winds, and the strong

(northerly) return flow at low levels. These features are even more readily seen in the mean meridional circulation plot (Fig. 55).

Looking at the time evolution of the tracer fields in Figs. 45–52 (and comparing them to Figs. 25–32) it is seen that the mixing is even more rapid than in the clear, winter solstice experiment. In addition, the mixing is quite thorough throughout the atmosphere between 60S and 60N in both the horizontally and vertically stratified cases. (Not surprisingly, this corresponds roughly to the span of the cross-equatorial Hadley cell.) The horizontal and vertical gradients in this region are small but no problems arose in calculating the mixing coefficients. (If the aerosol model had been run for a few more sols it appears that the mixing would have been too complete and problems with the mean tracer gradients approaching zero and/or the two cases having parallel gradients would have occurred.) Even at high latitudes very significant mixing is taking place as is evident by the changes in isopleth values.

The time-averaged mass mixing ratio plots in Figs. 53 and 54 highlight the thoroughness of the mixing under dusty conditions. The horizontal and vertical gradients of mean tracer have decreased significantly throughout the majority of the atmosphere. For the horizontal case this can be seen by comparing Fig. 53 with the initial tracer state in Fig. 45. In this instance the mass mixing ratios are generally seen to be increasing where they were initially small and decreasing where they were initially large indicating that tracer mass is being “transported” downgradient (and is subsequently decreasing those gradients).

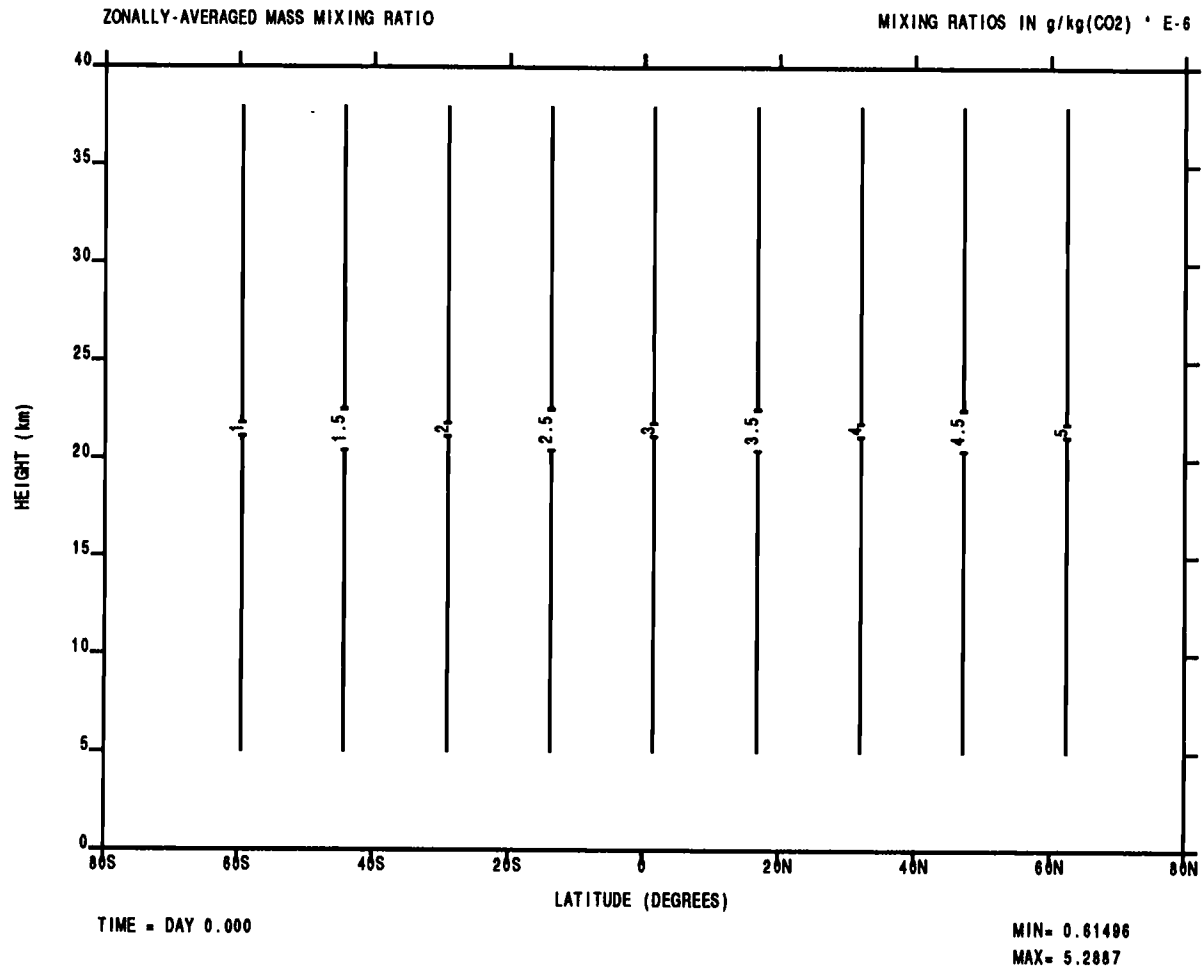


Fig. 45 Initial distribution of the mean mixing ratios for the horizontally stratified case. (NHWS, $\tau=1.0$)

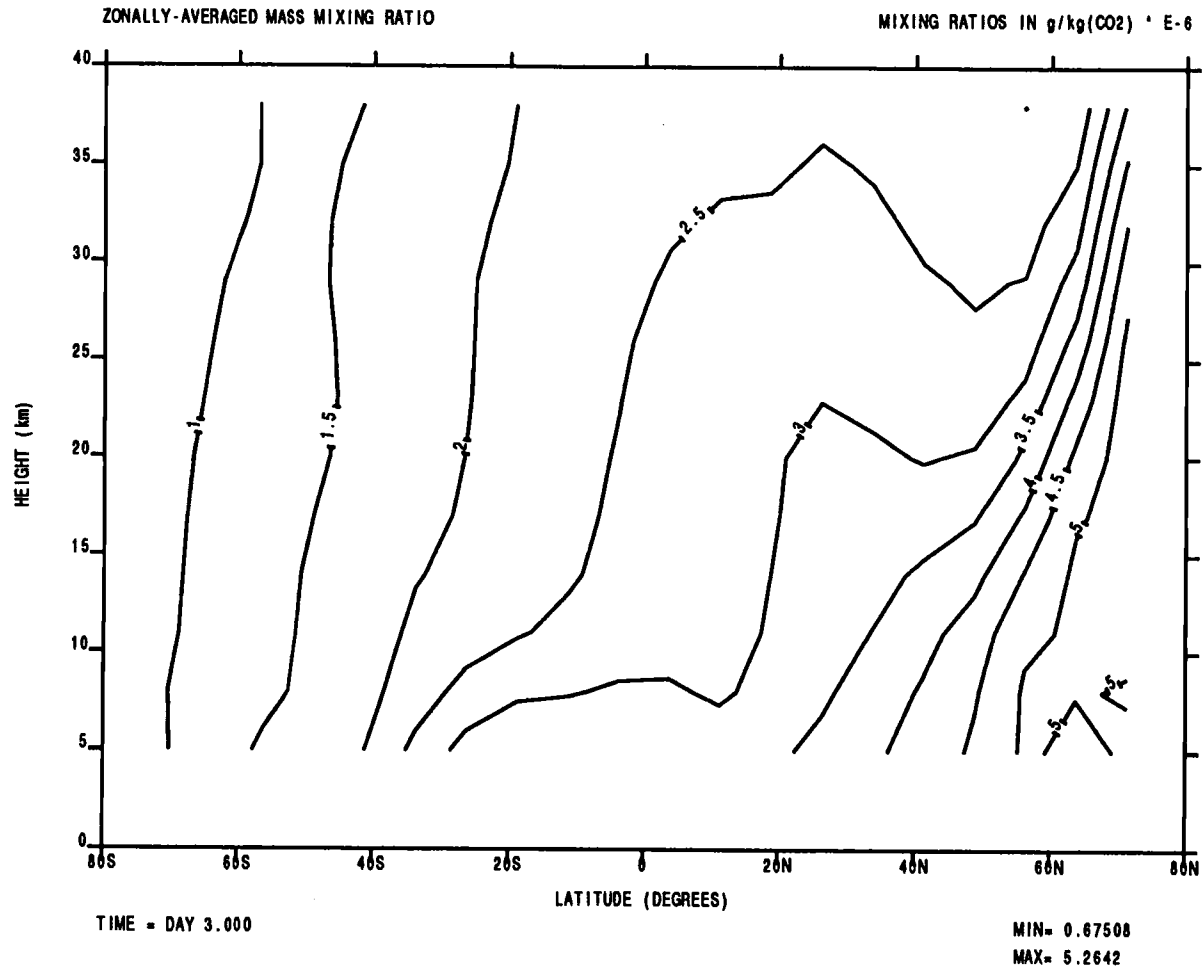


Fig. 46 Distribution of the mean mixing ratios after day 3 for the horizontally stratified case. (NHWS, $\tau=1.0$)

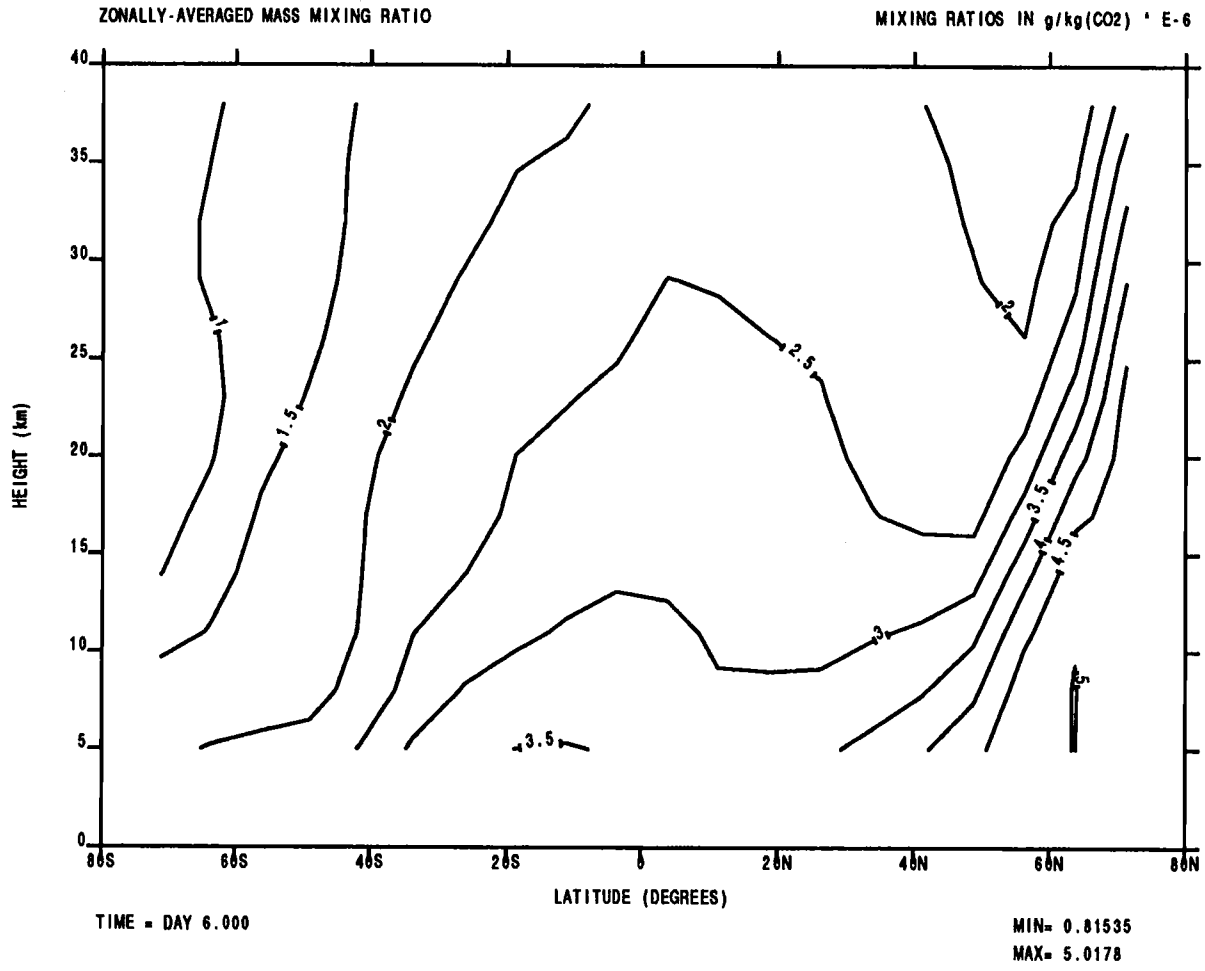


Fig. 47 Distribution of the mean mixing ratios after day 6 for the horizontally stratified case. (NHWS, $\tau=1.0$)

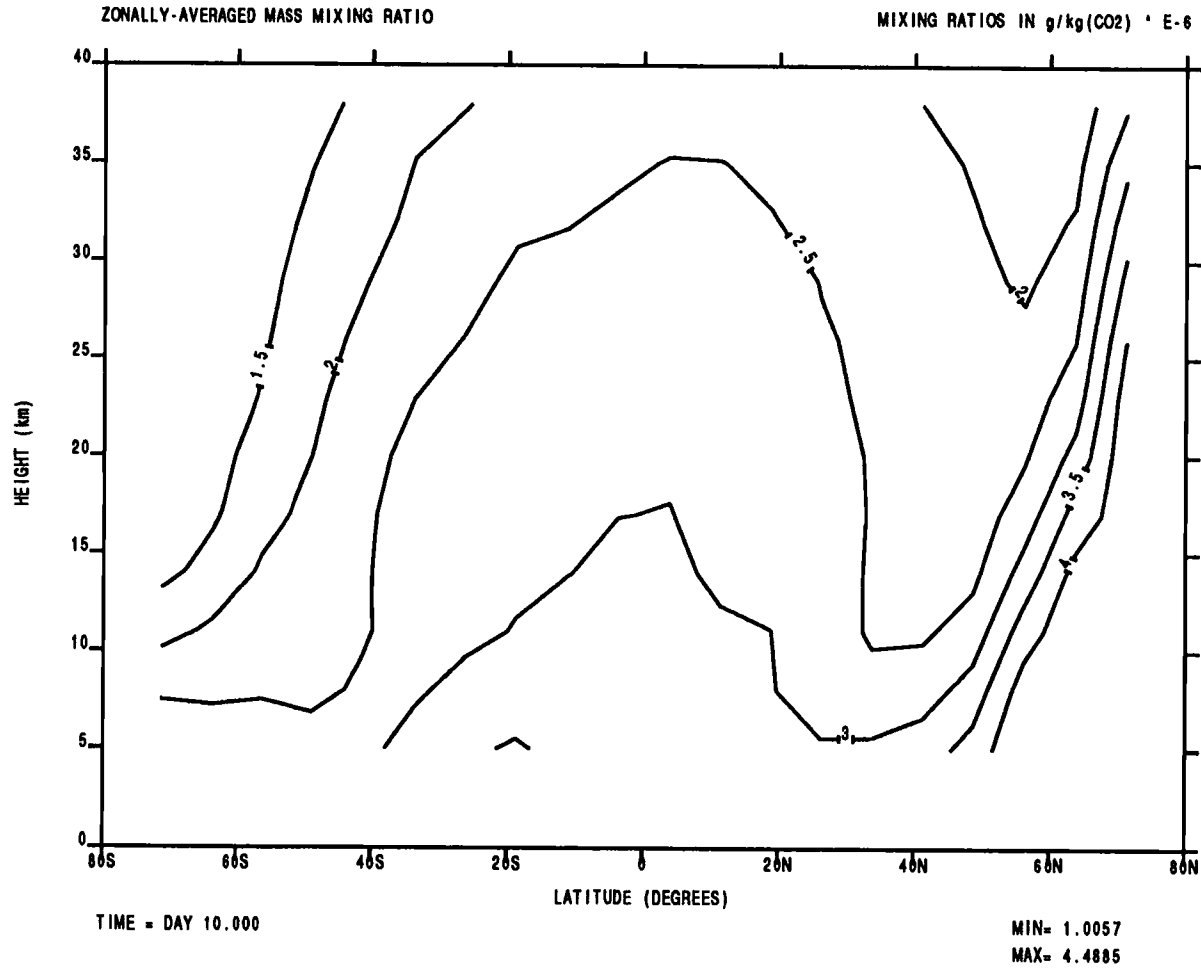


Fig. 48 Distribution of the mean mixing ratios after day 10 for the horizontally stratified case. (NHWS, $\tau=1.0$)

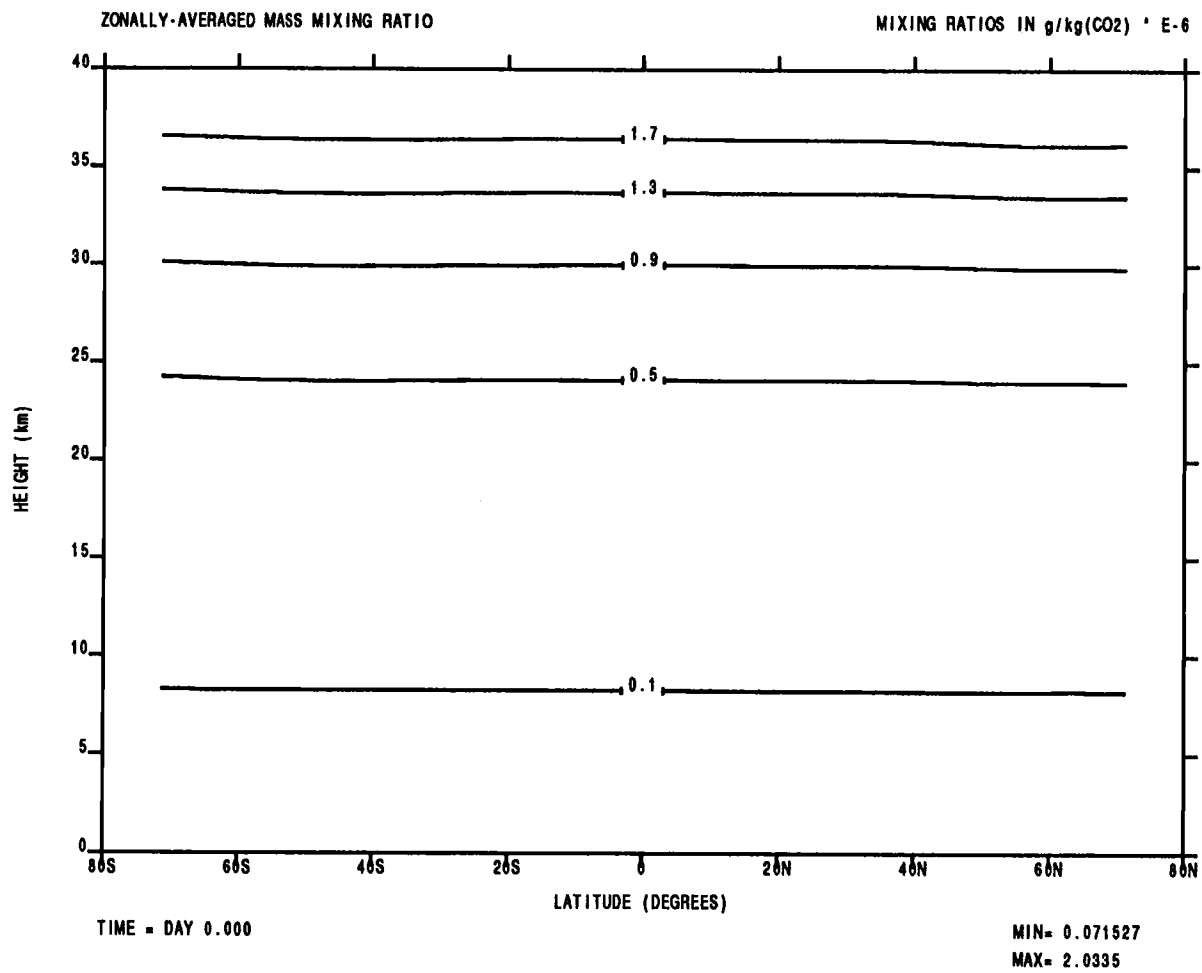


Fig. 49 Initial distribution of the mean mixing ratios for the vertically stratified case. (NHWS, $\tau=1.0$)

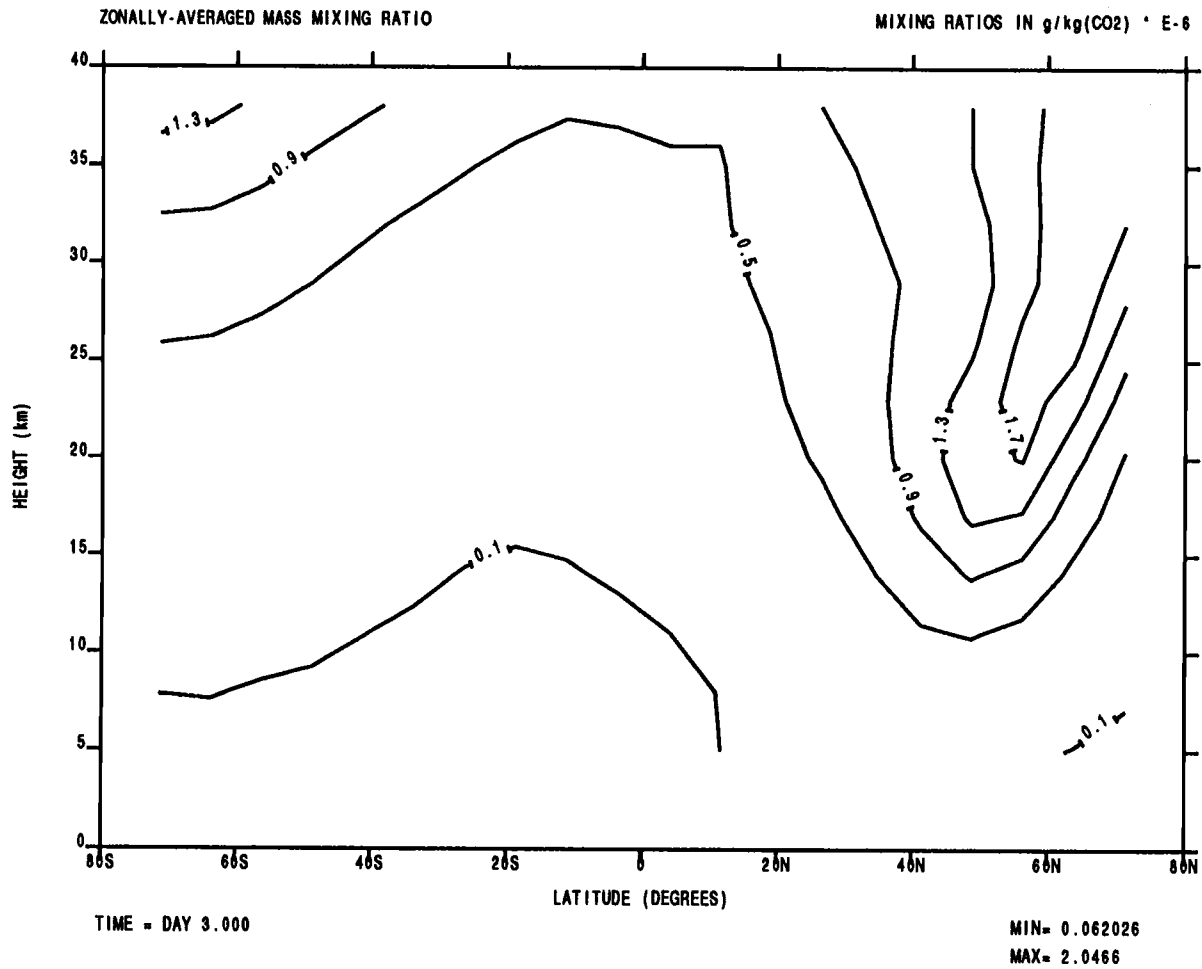


Fig. 50 Distribution of the mean mixing ratios after day 3 for the vertically stratified case. (NHWS, $\tau=1.0$)

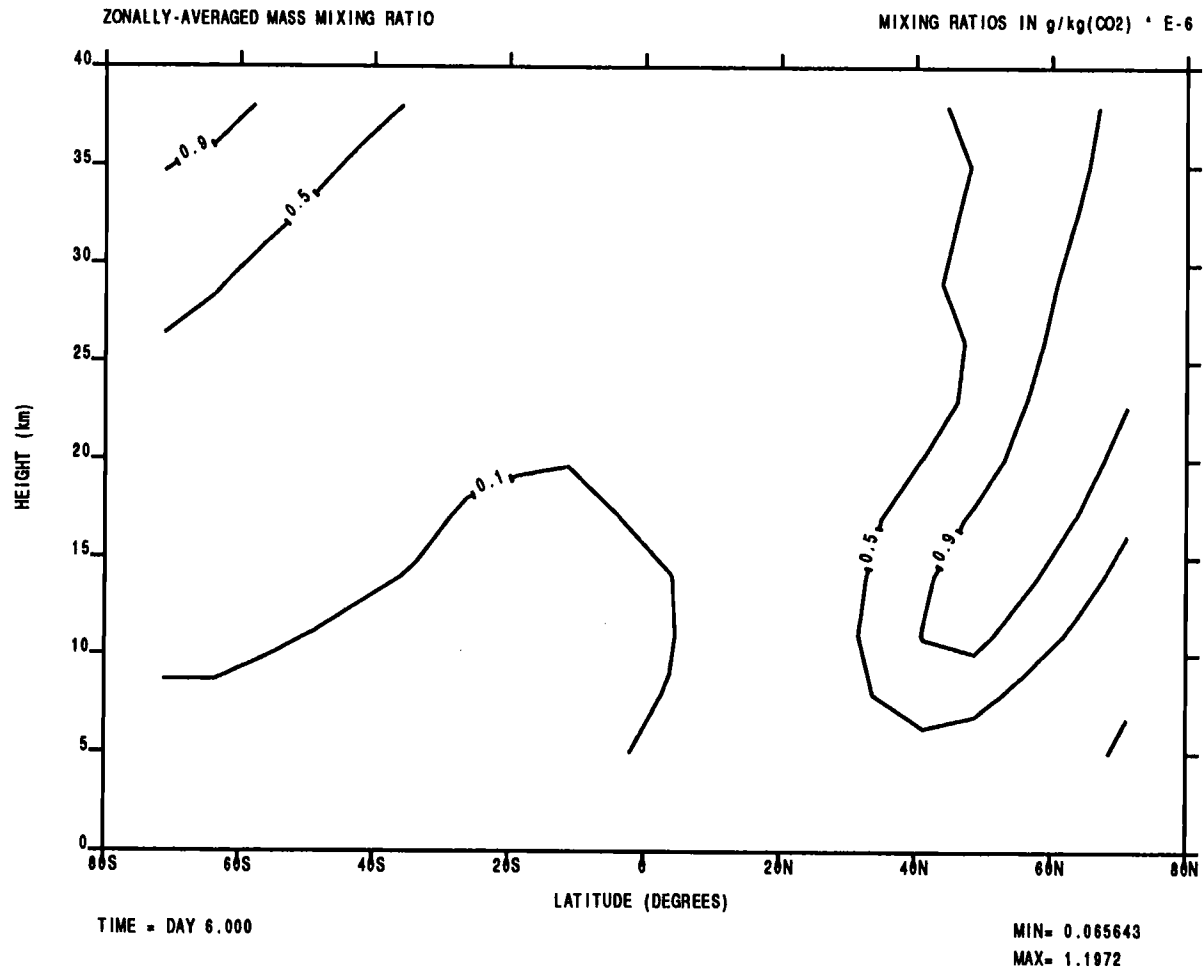


Fig. 51 Distribution of the mean mixing ratios after day 6 for the vertically stratified case. (NHWS, $\tau=1.0$)

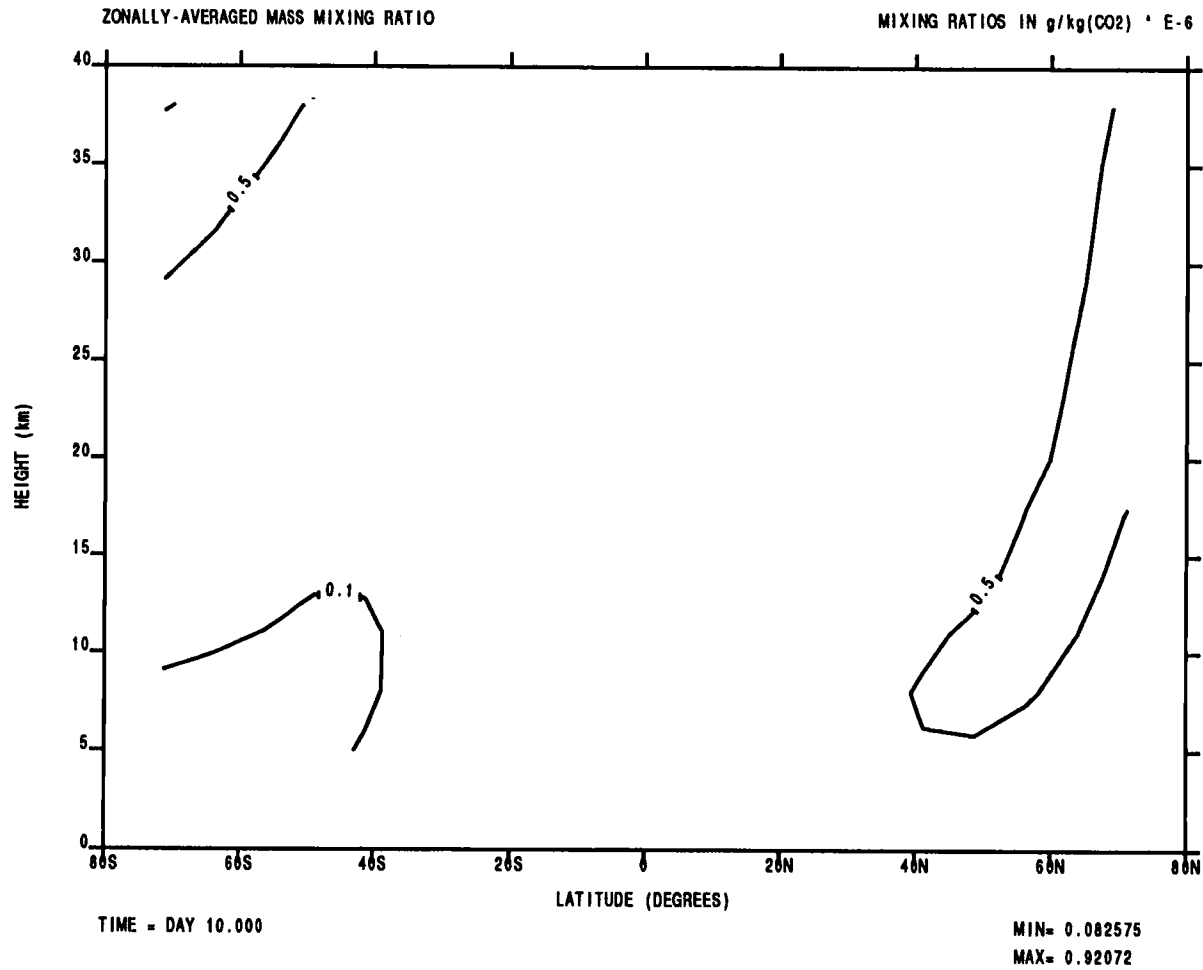


Fig. 52 Distribution of mean mixing ratios after day 10 for the vertically stratified case. (NHWS, $\tau=1.0$)

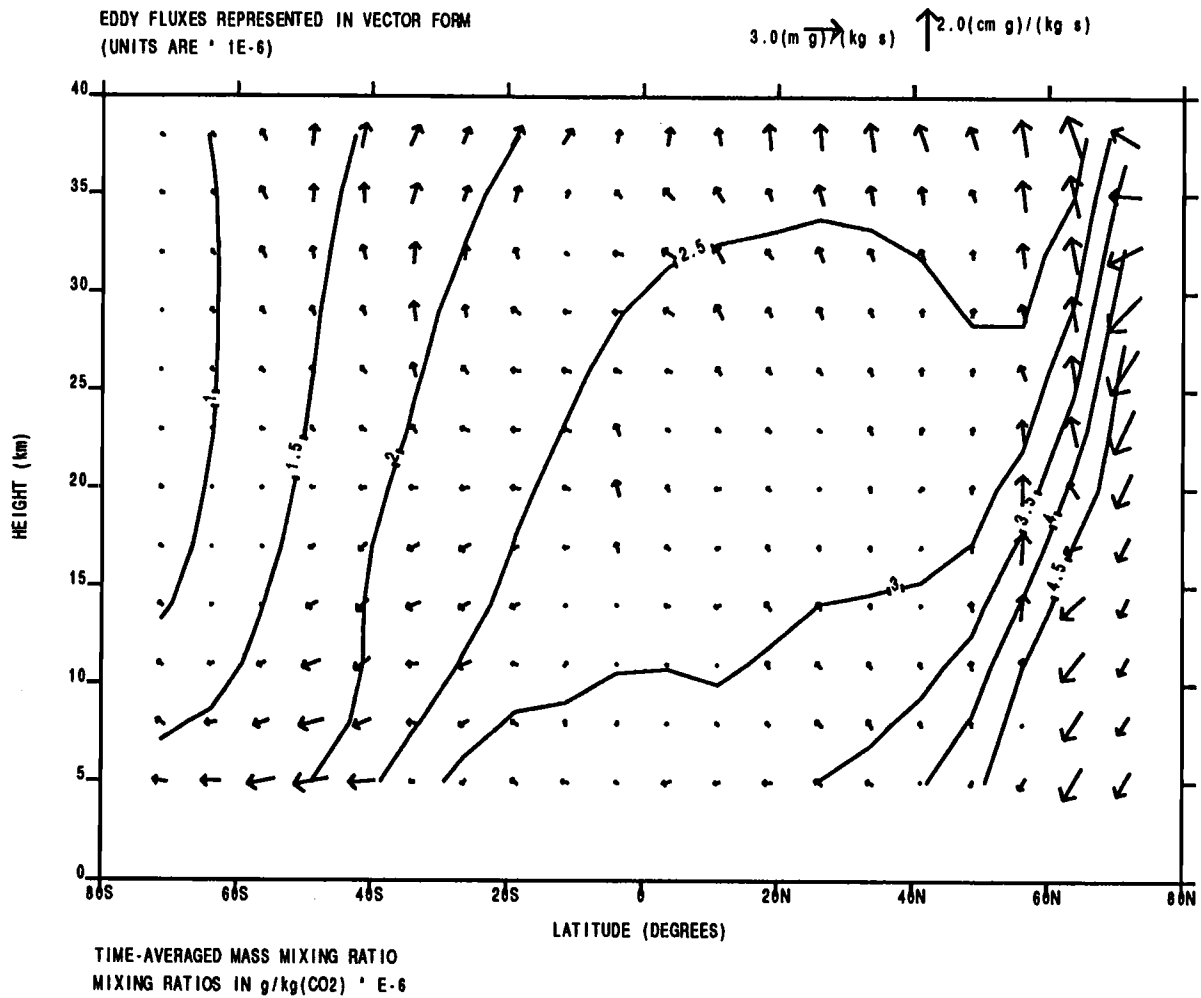


Fig. 53 Time-averaged mean mixing ratios and eddy fluxes for the horizontally stratified case. (NHWS, $\tau=1.0$)

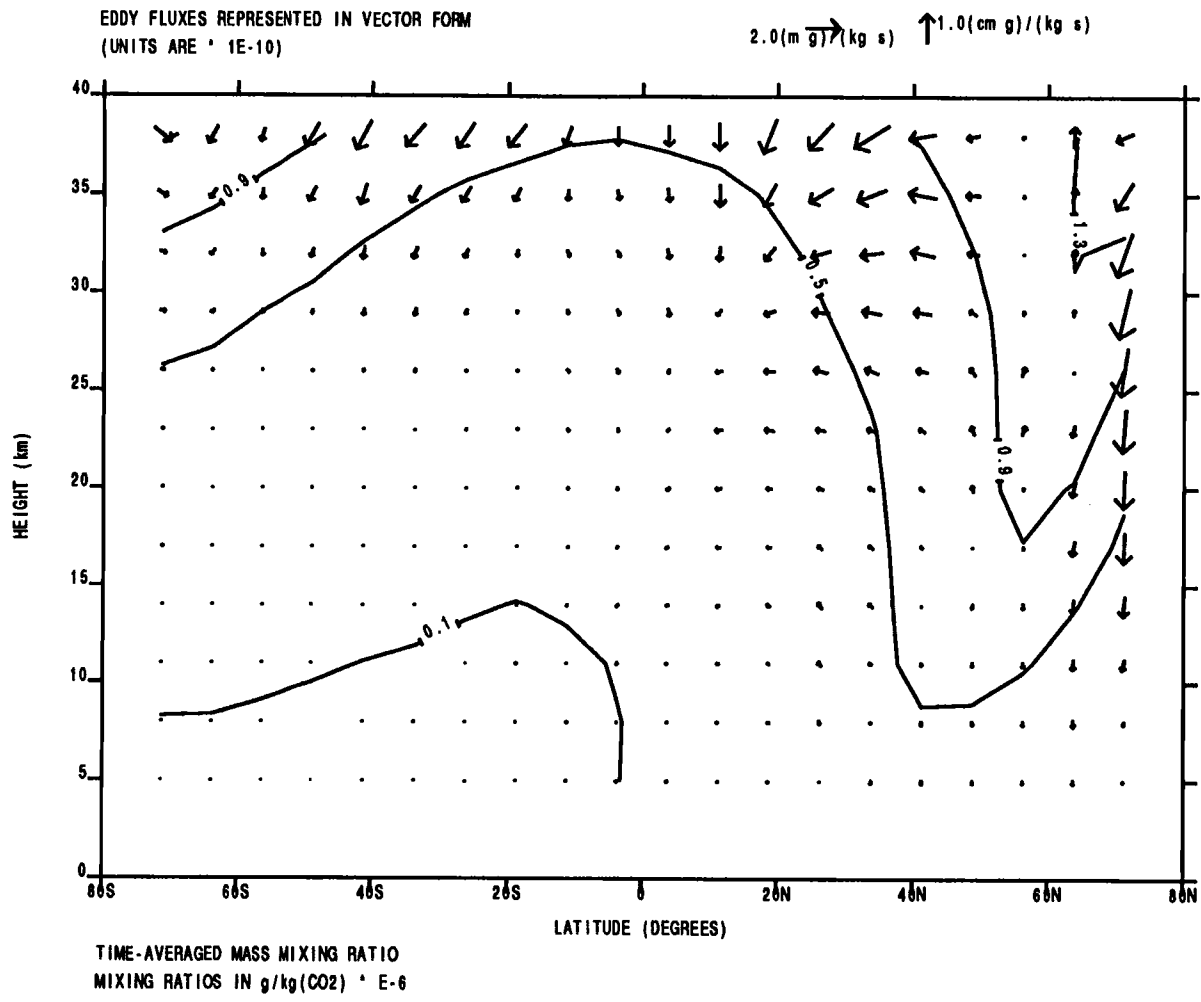


Fig. 54 Time-averaged mean mixing ratios and eddy fluxes for the vertically stratified case. (NHWS, $\tau=1.0$)

In the horizontal case the eddy fluxes are seen to be primarily cross-contour (downgradient) throughout the atmosphere from 30S to 50N indicating diffusive eddy transport in this region. In high northern latitudes and mid- to high southern latitudes the eddy fluxes are directed much less cross-contour suggesting advective-type eddy transport in these regions. Thus, for the horizontal case, the addition of dust to the atmosphere appears to increase the proportion of advective-type eddy transport relative to diffusive-type eddy transport.

Looking at the eddy fluxes for the vertical case it is seen that the largest values are concentrated at the top levels of the model and in the highest northern latitudes. The eddy fluxes at the top levels in the southern hemisphere and at the high northern latitudes are less cross-contour than those in the top levels of the lower northern latitudes. This suggests that the transport in the former regions is more of the advective type while that in the latter region is of the diffusive type.

Fig. 55 shows the mean meridional circulation which is dominated by a large, cross-equatorial Hadley cell. The rising and sinking branches are centered at approximately 30S and 45N as expected from the plot of \bar{w} in Fig. 44. This cell is characterized by strong winds, especially near the top of the model. (Thus, the overall effect of the dust loading on the mean circulation has been to increase the intensity of the winds and the span of the cross-equatorial Hadley cell.) Haberle et al. [1993] found a weak Hadley cell in high southern latitudes and an indirect Ferrell cell at high northern latitudes. These two features do not appear in this plot due to the cutoff of data at the highest two latitudes and the relatively small values of \bar{v} and \bar{w} in these regions.

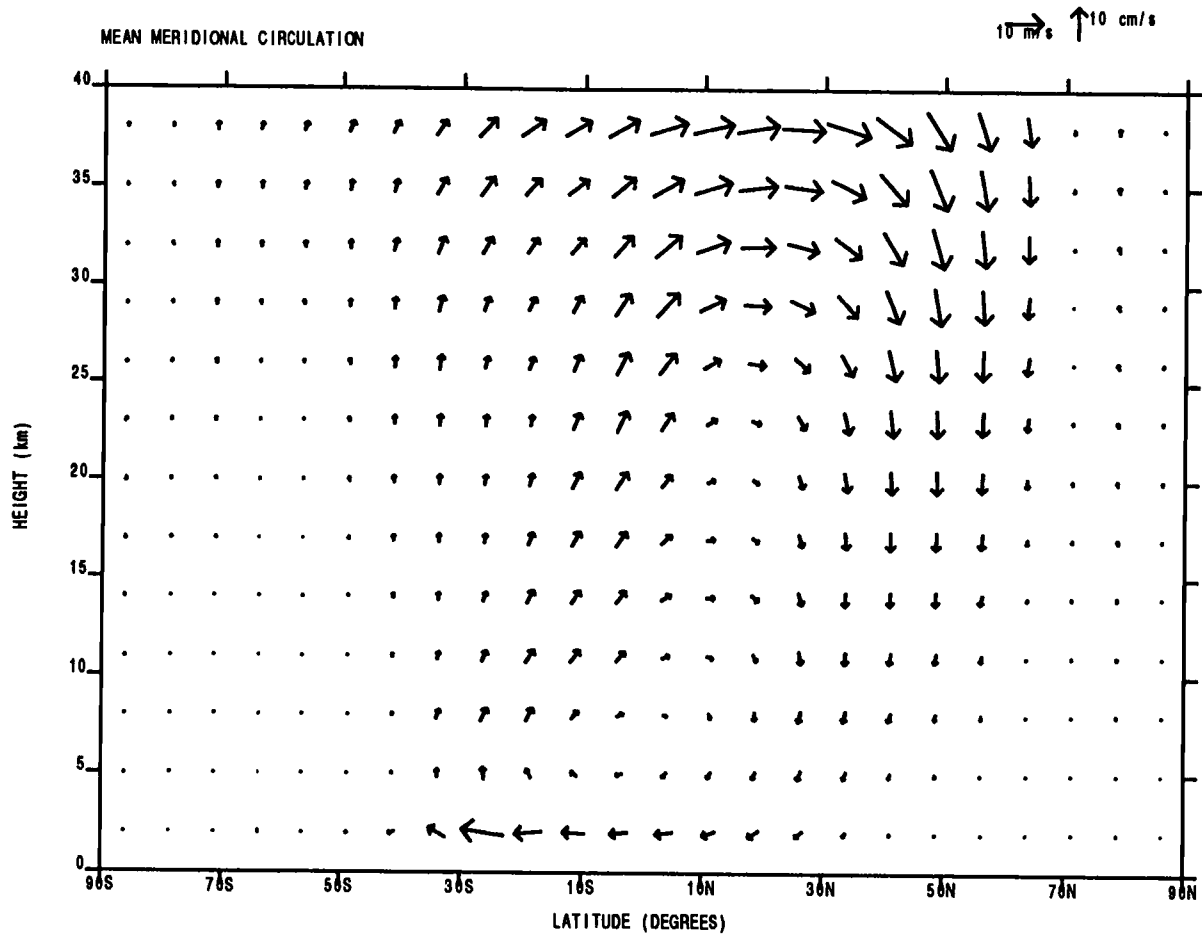


Fig. 55 Mean meridional circulation for the northern hemisphere winter solstice case ($\tau=1.0$).

The transport circulation for this case responds similarly to the dust loading. The horizontal span increases as does the intensity of the circulation (as seen in Fig. 56). Again, the most notable increase in circulation strength is at the highest levels of the model. The circulation vectors at these levels are also directed towards regions of strong horizontal and vertical mixing (see Figs. 57 and 58). As in the clear case, there is a barely discernible Hadley cell at low levels in the highest southern latitudes. Again, as for the clear case, essentially no Ferrell cell is evident.

Figs. 57 and 58 show the eddy mixing coefficient distributions for Case 3. After applying the quality control conditions to this experiment it was found that 11% of the K_{yy} values and 16% of the K_{zz} values needed adjusting to the minimum values specified. There was no apparent pattern or region, however, where data points systematically failed to meet the minimum values specified.

The distribution of K_{yy} under dusty conditions shows some similarities to that under clear conditions. The band stretching from low levels in the lowest southern latitudes to the mid-levels of the northern subtropics is still present but the values ($3-11 \times 10^6 \text{ m}^2/\text{s}$) in this region are about twice that in Case 2. However, in the present experiment this band continues on up to the highest levels of the model in northern mid-latitudes. This portion contains the largest values in this band (up to $17 \times 10^6 \text{ m}^2/\text{s}$) and highlights the significant increase in horizontal mixing in the upper atmosphere under dusty conditions. Another strong band of mixing common to both cases is found in the high latitudes of the northern hemisphere. It is this region that contains the largest values of K_{yy} in both plots.

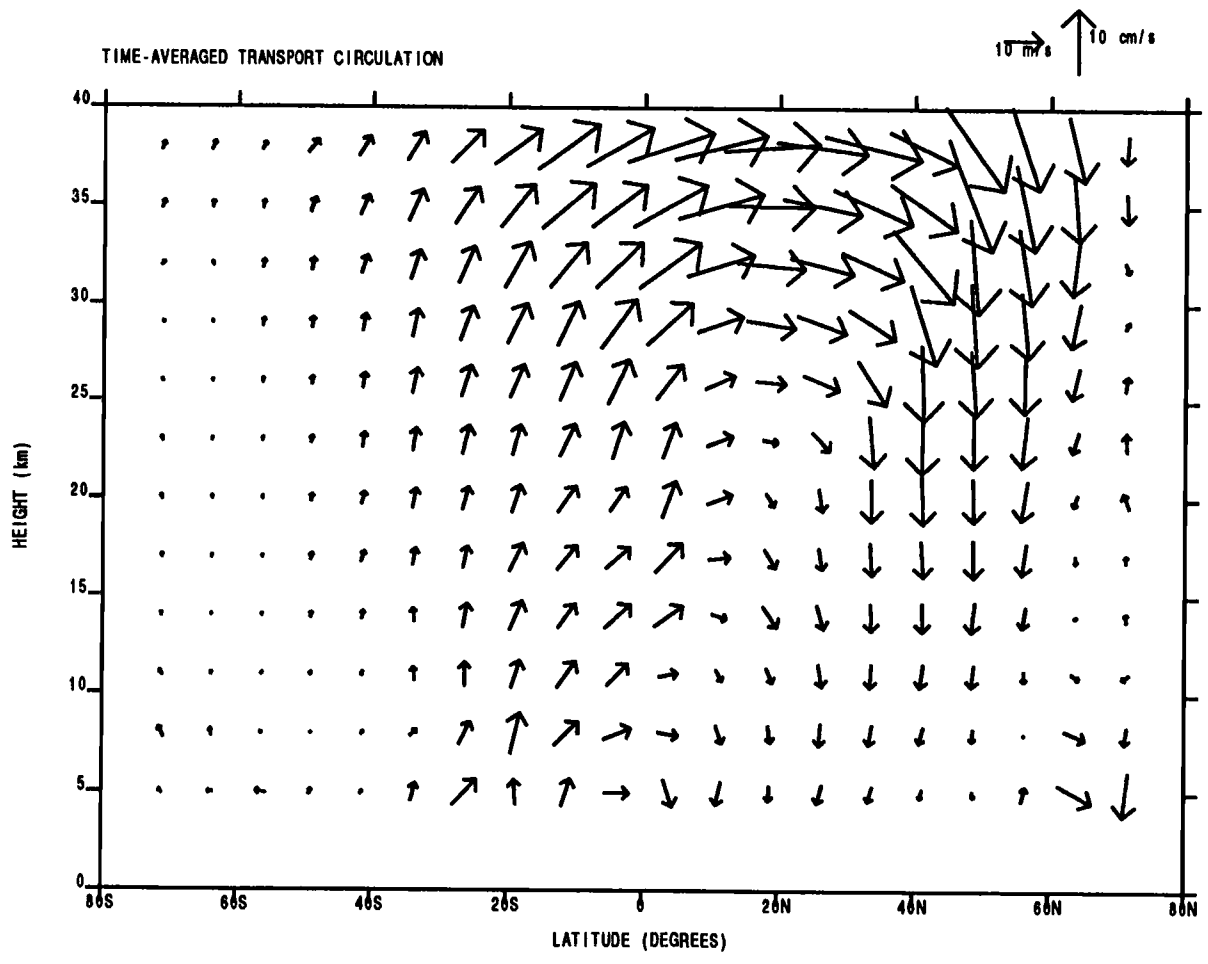


Fig. 56 Effective transport circulation for the northern hemisphere winter solstice case ($\tau=1.0$).

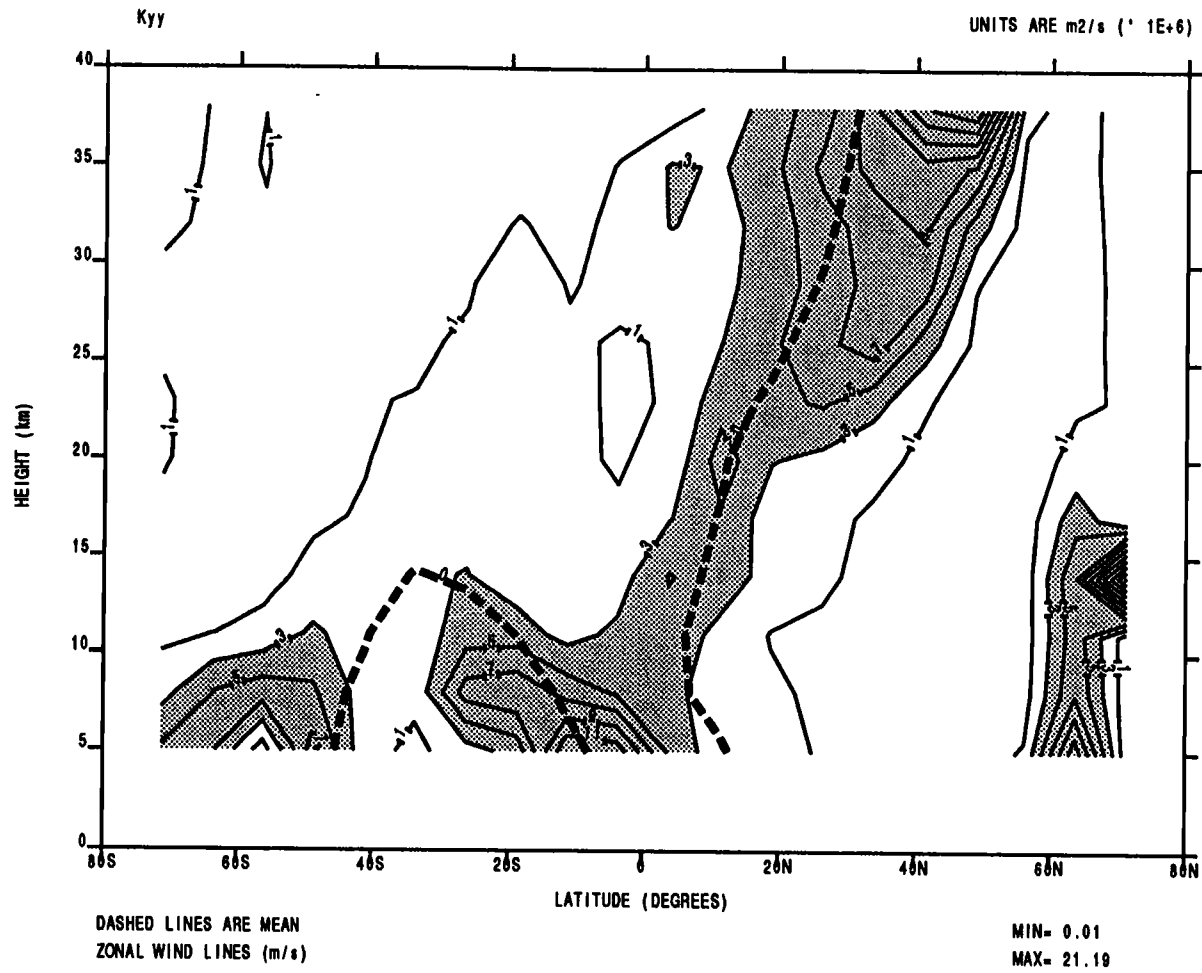


Fig. 57 Distribution of K_{yy} , the horizontal eddy diffusion coefficient. (NHWS, $\tau=1.0$).

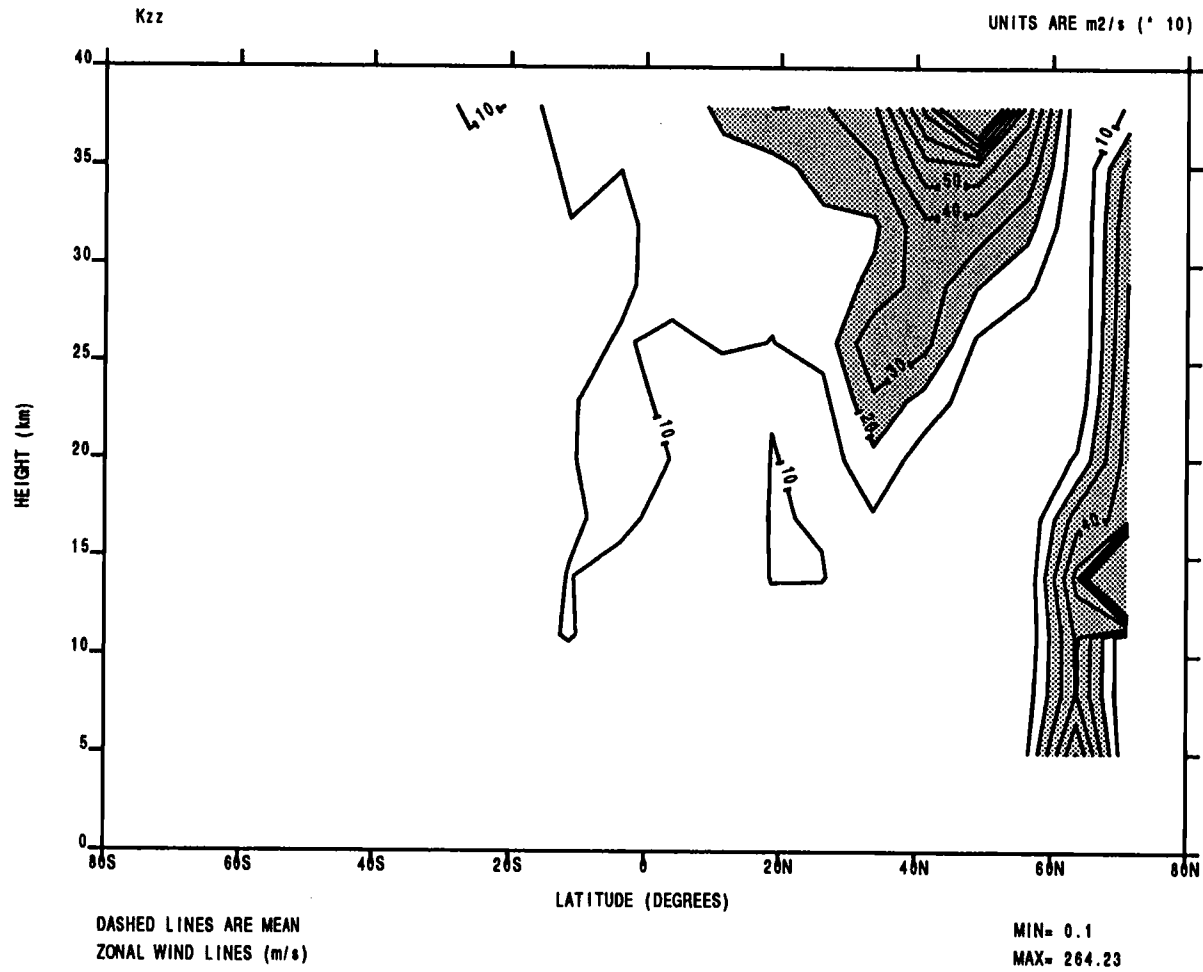


Fig. 58 Distribution of K_{zz} , the vertical eddy diffusion coefficient. (NHWS, $\tau=1.0$).

The area of large K_{yy} in mid- to high northern latitudes is attributable to transient eddy activity. The strong mixing at low southern latitudes is likely associated with stationary planetary waves. The strong horizontal mixing in the higher levels is correlated with the low zonal wind speeds and again suggests breaking quasistationary and/or transient waves as the source. It is possible that the tides could be contributing to the horizontal mixing near the top of the model also.

The key difference in the dusty case is a region of relatively strong mixing in the mid- to high southern latitudes at low levels which does not appear in the dust-free case. This region shows some correlation with the lower zonal wind speed lines which suggests planetary waves as the source. However, as will be seen in Fig. 59, the transient eddy activity in the southern hemisphere is minimal and thus is not expected to be the cause of strong mixing in the southern hemisphere. This region may be influenced by quasistationary eddies.

The distribution of K_{zz} is characterized by two bands of maximum values. One is located in the higher northern latitudes and stretches from the ground to the top of the atmosphere. This band is almost identical to that observed in the clear atmosphere case. In each case the largest values of K_{zz} are found in this region but those in the dusty case are up to two and one half times larger than those in the dust-free case. This band is in a latitudinal location where transient eddies are prevalent and shows some correlation with low wind speed lines which would seem to indicate that transient eddies are the dominant influence on the vertical mixing in this region. At higher altitudes the diurnal tides are also likely to make a significant contribution to the values of K_{zz} .

The second band of strong vertical mixing spans 10N to 60N between 20 and 38 km. As mentioned before, strong vertical mixing in this region is likely the result of the diurnal tides. This region of maximum values was also observed in the clear case, however the values in the dusty case ($200\text{--}1000\text{ m}^2/\text{s}$) are again much larger (up to 5 times) than those in the clear case indicating the significance of dust for the strength of the vertical mixing in this region. Also of interest is the lack of a band of maximum values located over the southern subtropics and tropics from 5 to 20 km. This was well defined in the clear case (see Fig. 38) but is not observed in the present case. This result is in accord with the results of Zurek [1976] who found that the topographic distortion of the thermal forcing (of the diurnal tides) is minimized by a warm, dust-laden atmosphere. This is because the airborne dust absorbs a large fraction of the incoming solar radiation producing a warm atmosphere. However, even though the topographic contribution is minimized, the dust-filled atmosphere will itself produce a diurnal response which is stronger than that under clear conditions. Thus, if the response observed in Experiment 2 is a result of the topographic forcing of the thermal tide it is expected that this result would be minimized (or not observed at all) under dusty conditions.

Figs. 59–62 (provided by J. Barnes, 1994, personal communication, identical L_s span) support the above suggestions as to the likely sources responsible for the strong diffusive mixing in both the horizontal and vertical for the dusty, northern hemisphere winter solstice experiment. Figs. 59 and 60 show the transient eddy horizontal and vertical heat fluxes for time scales greater than two days. It is seen that the horizontal fluxes are concentrated from 30N to 70N at low levels and from 20S to 80N between 25 and 45 km. Thus, transient eddy activity appears to be a

30A4 TRANS. EDDY HORIZ. HEAT FLUX: LOW ($^{\circ}\text{K m/s}$)

RUN 87.57
TAUTOT = 1.0
MAX = $2.20 \cdot 10^1 \text{ } ^{\circ}\text{K m/s}$

SEASONAL DATES: 267.52 - 286.09

TIME AVERAGE 480.0HRS
TO 1200.0HRS
MIN = $-3.70 \cdot 10^1 \text{ } ^{\circ}\text{K m/s}$

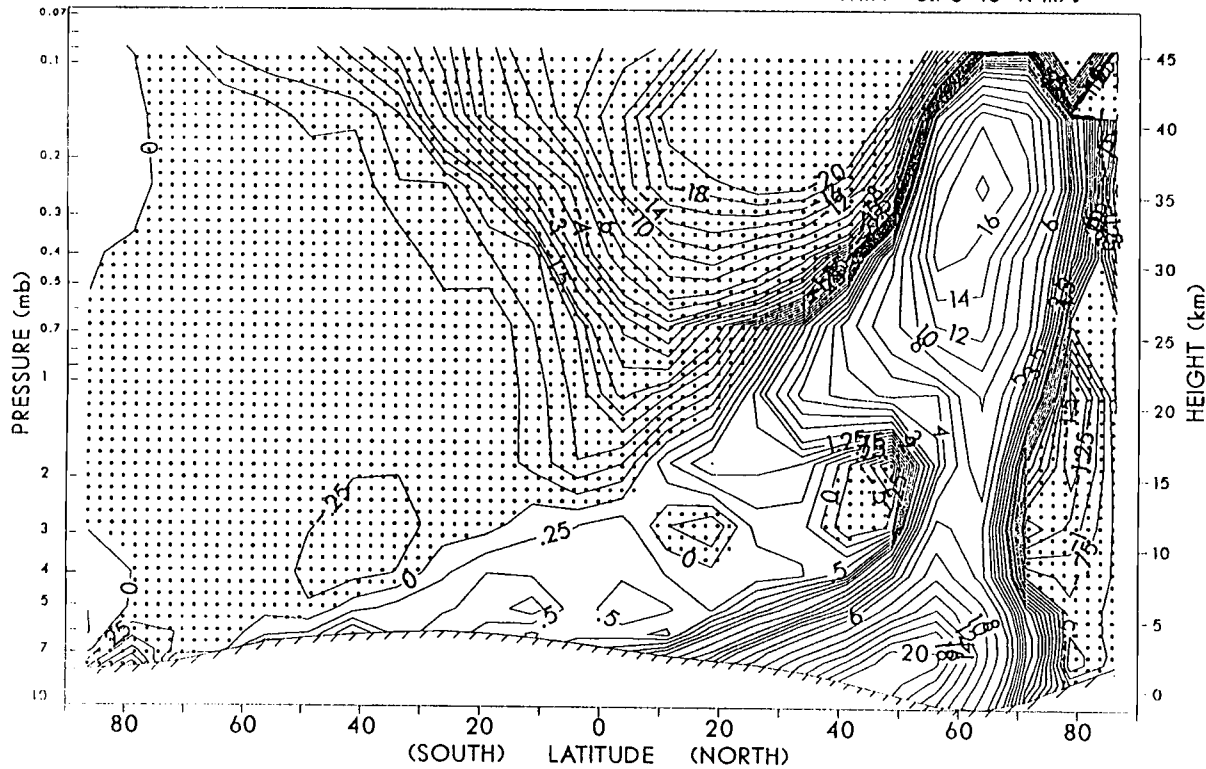


Fig. 59 Distribution of the transient eddy horizontal heat fluxes (after low-pass filtering) showing the regions of significant transient eddy activity.

30A6 TRANS. EDDY VERT. HEAT FLUX: LOW ($10^{-6} \text{ } ^\circ\text{K m/s}$)

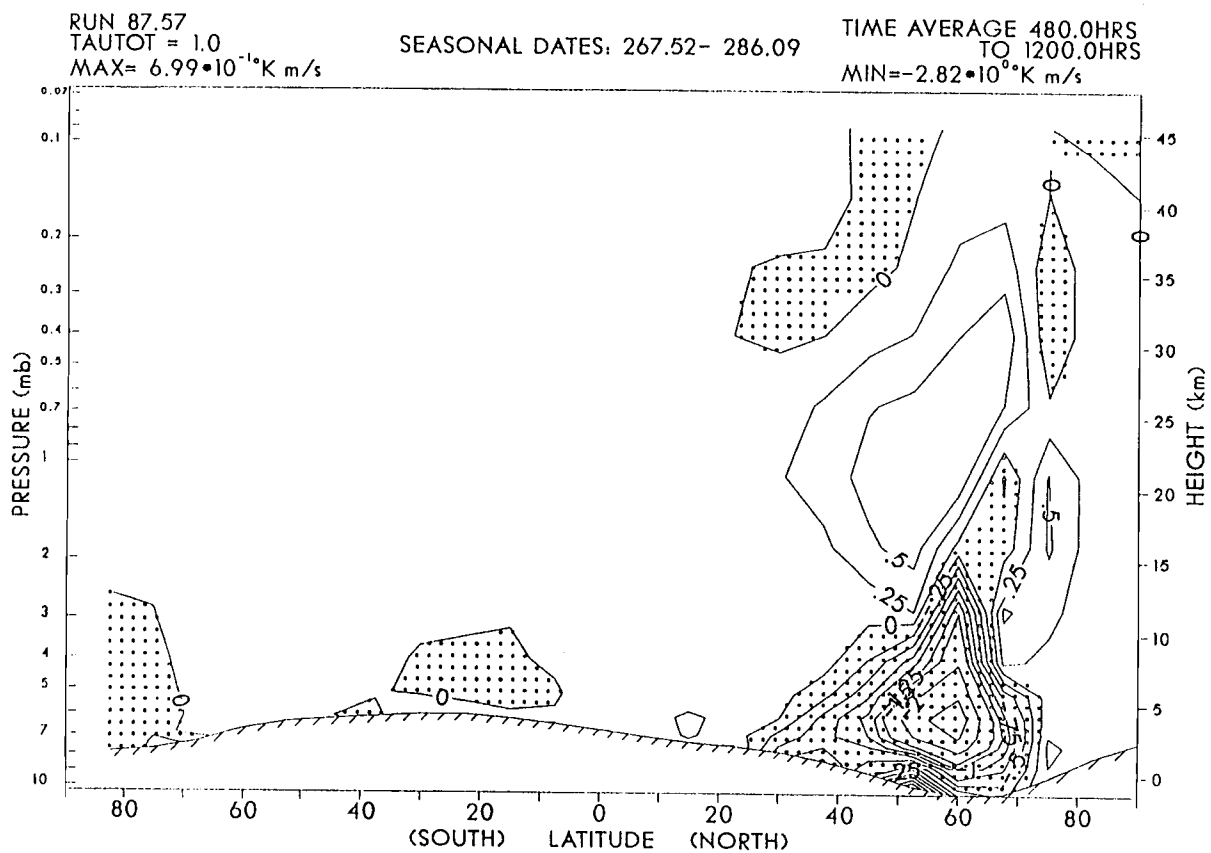


Fig. 60 Distribution of the transient eddy vertical heat fluxes (after low-pass filtering) showing the regions of significant transient eddy activity.

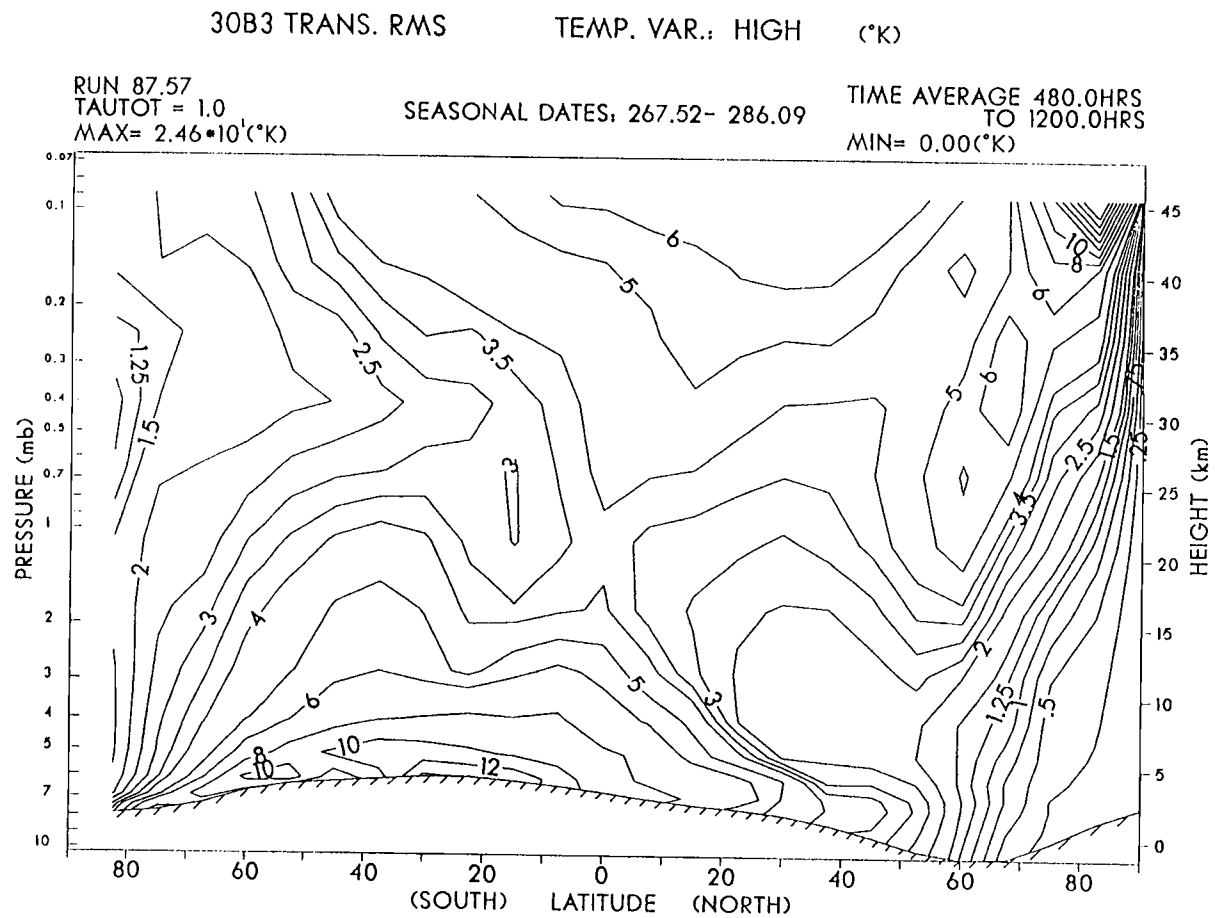


Fig. 61 Distribution of the transient rms temperature variance (after high-pass filtering) showing the influence of the thermal tide.

23B STATIONARY RMS GEOP. HT. VARIANCE (m)

RUN 87.57
TAUTOT = 1.0
MAX= $6.62 \cdot 10^2$ (m)

SEASONAL DATES: 267.52- 286.09

TIME AVERAGE 480.0HRS
TO 1200.0HRS
MIN= 0.00(m)

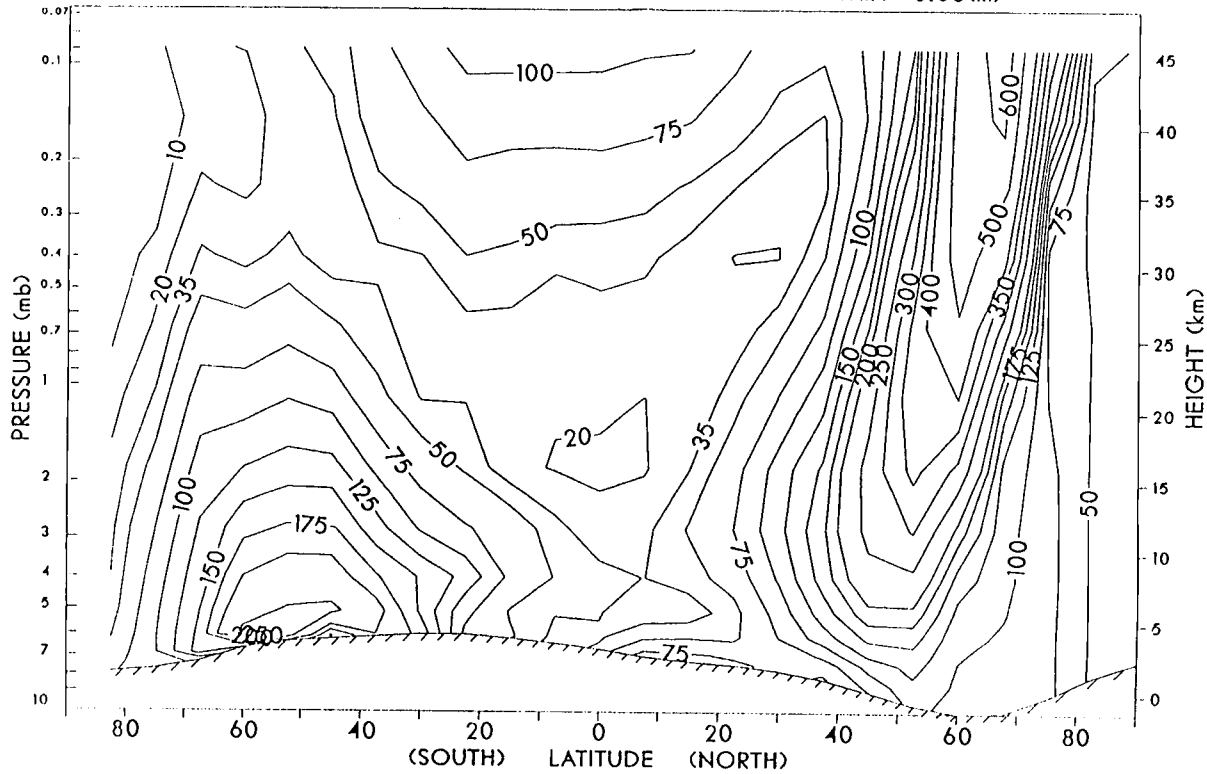


Fig. 62 Distribution of the stationary rms geopotential height variance showing the influence of stationary eddy activity.

source of the strong horizontal mixing observed in these regions. The maximum vertical fluxes are located between 30N and 70N from the ground to about 35 km which supports the assertion that the large K_{zz} values at low levels near 60N are due to the transient eddies.

Fig. 61 is the transient rms temperature variance after high-pass filtering to isolate the tidal motions. This plot shows that the largest tidal activity is now located in the lower southern latitudes near the ground and at high northern latitudes between 35 and 45 km. Thus the Martian tides are now expected to have their greatest impact in these regions under dusty conditions. The latter region correlates with the strong vertical mixing in the high altitudes of the northern hemisphere. The tides and/or stationary waves are the likely contributors to the strong horizontal mixing in the southern latitudes. The stationary wave contribution is suggested by Fig. 62 (the stationary rms geopotential height variance) which shows a local maximum of activity near the ground in southern latitudes as well as a local maximum in the high altitudes of the mid-latitudes of the northern hemisphere.

4.4 Time Scales for Atmospheric Overturning

In this section, the time scale for atmospheric overturning by the mean meridional circulation is computed following the methodology used by Santee and Crisp [1994]. A time scale formulation defined by

$$t_A^{-1} = \frac{1}{M} \frac{dM}{dt} \quad (52)$$

is adopted, where M is the total "stratospheric" mass and $\frac{dM}{dt}$ is the mass flux into the Martian stratosphere, which by mass continuity must also equal the flux out

of the stratosphere. (For Mars, the “stratosphere” is defined as that part of the atmosphere above 1 mb. There is no physical basis for this choice but is being used in order to facilitate comparisons of my results with those of Santee and Crisp [1994].) Thus, t_A is an advective residence time for air parcels in the stratosphere, associated with transport by the mean circulation only. Of course, in reality, eddy transports also act to mix air between the “stratosphere” and the “troposphere.”

The mass of the Martian stratosphere is given by the following expression,

$$M = 4\pi (a + z(1 \text{ mb}))^2 \int_{z(1\text{mb})}^{\infty} \rho(z) dz \quad (53)$$

where a is the radius of Mars, $z(1 \text{ mb})$ is the log-pressure height at 1 mb, and $\rho(z)$ is the vertical density profile given by

$$\rho(z) = \rho_s e^{(-\frac{z}{H})} \quad (54)$$

where ρ_s is the density at the surface ($z = 0$),

$$\rho_s = 100 \frac{P_s}{gH} \quad (55)$$

where P_s is the surface pressure in mb, g is the Martian gravity constant, and H is the atmospheric scale height. The mass flux, $\frac{dM}{dt}$, can be estimated from the mass-weighted stream function Ψ_m (as in Santee and Crisp [1994]) defined by

$$\Psi_m = 2\pi a^2 \rho_s e^{(-\frac{z}{H})} \int_{-\frac{\pi}{2}}^{\phi} \cos \phi' \bar{w} d\phi' \quad (56)$$

This represents the horizontally integrated mass flux across the level z , from the south pole to latitude ϕ . Thus, $\frac{dM}{dt}$ can be approximated by considering the range

of latitudes where \bar{w} is positive at 1 mb. For example, $\frac{dM}{dt}$ for the equinox case can be estimated by

$$\frac{dM}{dt} \approx \Psi_m(42N, 1 \text{ mb}) - \Psi_m(35S, 1 \text{ mb}) \quad (57)$$

Once M and $\frac{dM}{dt}$ have been estimated, it is straight forward to calculate the residence time t_A . Table 1 contains the pertinent parameters for these calculations as well as the calculated values of t_A .

For the equinox case the estimated parcel residence time is about 36 days. This is very close to the value obtained by Santee and Crisp [1994], of 38 days, based on a subset of Mariner 9 data taken near the same equinox season ($L_s = 343^\circ\text{--}348^\circ$). For the clear, northern hemisphere winter solstice case the residence time drops to about 19 days. This indicates that the increased intensity of the solstice circulation has shortened the advective time scale for overturning the atmosphere. The effect of dust is to further shorten the time scale as seen by the value of 6.6 days for the dusty, northern hemisphere winter solstice case. For purposes of comparison, Shia et al. [1989] show that the stratosphere on Earth has an advective residence time of approximately 1.8 years. Thus, one can see that mean transport time scales in the Mars atmosphere are dramatically shorter than in Earth's stratosphere.

Chamberlain and Hunten [1987] discuss a diffusive time scale, t_d , associated with eddy mixing,

$$t_d = \frac{L^2}{D} \quad (58)$$

where L is an arbitrary but typical length scale and D is the appropriate eddy diffusion coefficient. H is an appropriate length scale in the vertical direction and

	Spring Equinox ($\tau = 0$)	Northern Hemisphere Winter Solstice ($\tau = 0$)	Northern Hemisphere Winter Solstice ($\tau = 1.0$)
H (m)	8692.8	9099.7	9976.0
P_s (mb)	7.903	7.437	7.589
z(1mb) (m)	17,970	18,260	20,220
ρ_s ($\frac{\text{kg}}{\text{m}^3}$)	0.0244	0.0220	0.0204
ϕ_1, ϕ_2	35S, 42N	50S, 33N	80S, 15N 70N, 86N
M ($\text{kg} \times 10^{15}$)	3.8912	3.8919	3.8964
$\frac{dM}{dt}$ ($\frac{\text{kg}}{\text{s}} \times 10^9$)	1.2514	2.3793	6.7884
t_A (days)	36.0	18.9	6.6
t_d vertical (days)	21.9	12.0	11.5
t_d horizontal (days)	46.3	23.1	15.4

Table 1 Results for time scale calculations. t_A is the advective transport time scale (for both horizontal and vertical directions), t_d is the diffusive transport time scale.

2000 km has been chosen as an appropriate horizontal length scale for “stratospheric” levels. Conrath [1975], Zurek [1976], Kong and McElroy [1977], Toon et al. [1977], and Anderson and Leovy [1978] have all estimated global values of K_{zz} using various methods. These estimates and methods have been summarized by Santee and Crisp [1994] as follows:

“Conrath [1975] deduces the dust optical depth during the dissipation phase of the 1971 dust storm from Mariner 9 IRIS temperature profiles and a simplified atmospheric heating model. To explain

the exponential decay of the dust opacity at both upper and lower atmospheric levels, he requires a vertical eddy diffusion coefficient $K_{zz} \geq 10^3 \text{ m}^2/\text{s}$. Zurek [1976] estimates the eddy coefficient for the turbulence generated by the diurnal atmospheric tide to be $K_{zz} \sim 5 \times 10^3 \text{ m}^2/\text{s}$. Kong and McElroy [1977] investigate a variety of photochemical models and conclude that mixing coefficients in this range are required to match the observed abundances of various atmospheric constituents. Toon et al. [1977] use a multiple scattering radiation code to find the best fit synthetic spectra to the Mariner 9 IRIS observations. They conclude that the size distribution of the dust particles did not change appreciably during the dissipation of the dust storm, and they invoke vertical mixing on the order of $10^3 \text{ m}^2/\text{s}$ to explain the constancy of the distribution. Anderson and Leovy [1978] examine Mariner 9 television reflectance profiles which crossed the limb of Mars. From an analysis of the decay of dust scale heights they also determine the vertical eddy mixing coefficient to be $K_{zz} \sim 10^3 \text{ m}^2/\text{s}$."

Each of these studies have suggested values of K_{zz} on the order of $10^3 \text{ m}^2/\text{s}$.

In their analysis of these studies Santee and Crisp note that

"The determinations of the eddy diffusion coefficient outlined above parameterized all contributions to the vertical transport. The derived values of the eddy diffusion coefficient therefore include the effects of large-scale organized motions, such as the mean meridional circulation, and are consequently much larger than they would be if they represented only the small-scale mixing processes. Although these large values of K_{zz} may be valid for the dustiest conditions or in limited regions, e.g., within the boundary layer, they are not appropriate for application on a global scale."

The results, as seen in the distributions of K_{zz} in Figs. 18, 38, and 58 support this. The only instances in which values of K_{zz} approach $10^3 \text{ m}^2/\text{s}$ are at lower levels near 60N in both the clear and dusty northern winter solstice cases and at the highest level near 40N in the dusty northern winter solstice case. (These values are approximately 900, 2000, and 1000 m^2/s , respectively.) These are certainly limited regions and not representative of typical values throughout the Martian

atmosphere. (However, it is again noted that the convective mixing in the aerosol model has been turned off for these experiments. The convective mixing would act to increase the K_{zz} values if on.)

In Figs. 18, 38, and 58 it is seen that the typical values of K_{zz} vary with conditions (season and dust loading) as well as location in the atmosphere (latitude and height). For the equinox case typical values of K_{zz} range from 20 to 70 m^2/s . For the clear northern winter solstice case the typical values are 40 to 120 m^2/s , while values of 100 m^2/s are typical for the dusty case.

For a value of K_{zz} on the order of $10^3 \text{ m}^2/\text{s}$ (and H approximately 9.5 km) the time scale for vertical diffusive mixing is $t_d \approx 1.0$ day. This is more than an order of magnitude less than the advective time scale for mean transport in both of the first two experiments and about six times shorter than that for the third experiment (see Table 1). If this value of K_{zz} is appropriate it would suggest that the vertical transport is dominated by diffusive mixing. However, the results (as seen in Table 1) for t_d show that the vertical diffusive transport time scale is comparable to the advective time scale in all three cases and is in fact not always the dominant process. These values were calculated based on the "typical" values of K_{zz} ; values used were 50 m^2/s for the equinox case, 80 m^2/s for the clear northern winter hemisphere solstice case, and 100 m^2/s for the dusty northern winter solstice case. These values lead to time scales of 22 days, 12 days, and 12 days, respectively. (For purposes of comparison, Shia et al. [1989] found the characteristic diffusive time scale (based on an upper limit of 1 m^2/s for K_{zz}) for Earth's stratosphere to be on the order of 1.5 years.)

From Figs. 17, 37, and 57 it is seen that “typical” values of K_{yy} are 1×10^6 m²/s for the first experiment, 2×10^6 m²/s for the second experiment, and 3×10^6 m²/s in the third. This gives horizontal diffusive time scales of 46 days for the first case, 23 days for the second, and 15 days in the last case. Of course, in this case, the choice of $L = 2000$ km is rather arbitrary, and different choices would yield somewhat different results. But horizontal mixing would appear to be roughly comparable to vertical mixing in efficiency.

By using the vertical transport velocity w_T in place of \bar{w} in equation (56) it is possible to compute a time scale, t_{tot} , that includes the effects of both mean advection and eddy advective transport. This is because the effective transport circulation includes both processes. Using W_T yields the following overturning time scales for the stratosphere: 35 days for the equinox case, 20 days for the clear, northern winter solstice case, and about 7 days for the dusty, northern winter case. These results are listed in Table 2. As can be seen by comparing the results in Tables 1 and 2, the Eulerian advective time scales and the transport advective time scales are essentially the same. This is because the eddy advective transports modify the Eulerian mean transports only slightly in the “stratosphere.”

Over all, these results show that advective and diffusive transport processes are of similar magnitude. My results support the view of Santee and Crisp [1994], that it is inappropriate to adopt one global value of K_{zz} (or K_{yy}) for the entire Martian atmosphere. Appropriate values of K_{zz} and K_{yy} are strongly dependent on season, dust loading, and location in the atmosphere. Values of K_{zz} of the order of 10^3 m²/s appear to be inappropriate, except in regions (mostly at low levels, and at high altitudes where wave breaking is occurring) of strongly turbulent, small-scale

	Spring Equinox ($\tau = 0$)	Northern Hemisphere Winter Solstice ($\tau = 0$)	Northern Hemisphere Winter Solstice ($\tau = 1.0$)
ϕ_1, ϕ_2	33S, 44N	45S, 32N	70S, 14N
t_{tot} (days)	35.2	20.0	6.7

Table 2 Computed time scales for stratospheric overturning based on the effective transport circulation.

mixing — as associated with convection. Again, it is important to note that the values of K_{zz} obtained here do not include the effects of convective mixing.

Chapter 5: Summary and Conclusions

A Mars GCM and an aerosol transport model have been employed to study Martian atmospheric transport for three different combinations of season and dust loading. Eddy mixing coefficients have been computed for each case based on the flux-gradient relationship. In this chapter the main results are summarized and some final conclusions are presented.

5.1 Mean Meridional Circulations

For the spring equinox case the mean meridional circulation is characterized by a dual Hadley cell system with a rising branch located just south of the equator, poleward flow at high altitudes, sinking motions at high latitudes, and strong return flow at low levels. The most vigorous winds are found in the equatorial regions where the zonal-mean meridional speeds reach 2 m/s at low levels from 30S to 10N while the strongest zonal-mean vertical winds reach 1 cm/s at 15 km near 10S. The zonal winds are predominately westerly in both hemispheres and have jets located at approximately 60S at 20 km and 50N at 20 km. These jets are similar in intensity, reaching 35 and 45 m/s, respectively.

The mean meridional circulation for the clear, northern hemisphere winter solstice experiment is also characterized by a two-cell Hadley circulation. However, one is a large, intense cross-equatorial cell while the other is a small, relatively weak cell confined to the southern hemisphere. There is also a thermally indirect Ferrell

cell at high northern latitudes. The dominant Hadley cell has rising and sinking branches at 30S and 40N, respectively. The flow is northerly at high altitudes and southerly at low levels. The zonal-mean meridional winds are strongest at low levels over equatorial regions where they reach 6 m/s. The vertical winds reach 2.5 cm/s above the subsolar point and 1.5 cm/s over 40N. The zonal winds are predominantly westerly in the northern hemisphere (with a jet of 95 m/s at 20 km near 50N) and predominantly easterly in the southern hemisphere (with a jet of 30 m/s at 30 km near 20S). In addition there is a surface westerly jet of 10m/s at 10S.

The dusty, northern hemisphere winter solstice circulation pattern is essentially similar to that under clear conditions. The major difference is that the zonal-mean winds have increased in intensity (especially at high altitudes) and the mean meridional circulation is stronger throughout the depth of the atmosphere. Meridional winds now exceed speeds of 15 m/s at the ground near 25S and at 35 km near 25N. Vertical motions (which are predominantly rising in the southern hemisphere and sinking in the northern hemisphere) exceed 7 cm/s at high altitudes near 10S (the rising branch of the main Hadley cell) and 50N (the corresponding sinking branch). The zonal winds intensify significantly compared to those under clear conditions. The westerly jet approaches 175 m/s at 35 km near 60N while the easterly jet reaches 80 m/s at 35 km near 10S. The surface westerly jet now exceeds 20 m/s at 30S.

As a result of these three experiments it is seen that the mean meridional circulation of Mars undergoes significant changes as the seasons progress (unlike the Earth's circulation pattern which remains relatively constant year round due to the effects of the oceans). This has a strong effect on the intensity of the winds,

which are stronger for solstice seasons and weaker for equinox seasons. In addition, while jets are comparable in both hemispheres at the spring equinox, the winter hemisphere jet is much stronger than the summer jet which is easterly for both of the winter solstice cases. The first order effects of dust are also evident by comparing the two winter solstice experiments. Most obvious is the increase in intensity of the mean winds and the meridional circulation, especially at high altitudes. In addition, the extent of the mean meridional circulation increases slightly and it is more clearly defined (as seen by comparing Figs. 35 and 55).

5.2 Transport Circulations

In all three cases the effective transport circulation patterns are largely similar in structure to the corresponding Eulerian mean meridional circulation patterns. To first order, the two circulations have the same strength, however in each case the effective transport circulation is somewhat stronger in regions where the diffusive mixing is strong (regions of large K 's). The transport circulation combines the mean advective transport and the eddy advective transport (from the eddy mixing). From Figs. 16, 36, and 56 it is seen that the transport circulation responds as does the mean meridional circulation to changes in season and dust loading.

5.3 Eddy Diffusion Coefficients

In all three cases it is clear that no single K value can adequately represent eddy mixing for the entire Martian atmosphere. In general, the values change strongly with season, dust loading, and location in the atmosphere. For spring

equinox the largest values of K_{yy} are $2-4 \times 10^6$ m²/s and are found in various portions of the atmosphere (see Fig. 17), while the largest values of K_{zz} are 40–90 m²/s and are found between 30S and 30N throughout the atmosphere and in high latitudes (of both hemispheres) at low levels.

For the winter solstice case with no dust, the values of K_{yy} increase somewhat throughout the atmosphere, with the largest values typically found near the ground in equatorial regions and in high northern latitudes. The largest values of K_{zz} (70–170 m²/s) are two to three times bigger than those of the equinox case, but are concentrated in similar regions with an additional band of strong mixing located at high northern latitudes.

With the addition of dust to the winter solstice experiment, the values of K_{yy} increase by a factor of two to four in regions where they were previously large, and at high altitudes over the low latitudes of the northern hemisphere. The values of K_{zz} also increased similarly, but the regions of strong mixing are confined to a small band at high altitudes in the northern hemisphere and a thin band from 5 to 35 km near 60N.

In general, the location of the regions of strong mixing give a good indication as to the source of the eddies responsible for the mixing. For K_{yy} the bands of strong mixing found at mid- to high latitudes are likely due to transient eddies at these latitudes (in the winter hemisphere). Regions of large K_{yy} values correlated to low zonal wind speeds suggest that this mixing is due to the breaking of transient and/or quasistationary waves propagating equatorwards. Those regions of large K_{yy} at low levels in the southern tropics are most likely influenced by stationary

planetary waves which have been forced by the large Martian topography at these latitudes.

The strong vertical mixing in mid- to high latitudes near the surface may be attributable to transient eddy activity. However, the strong mixing above equatorial regions is most likely due to thermal tides. Large values of K_{zz} are expected at these high altitudes, especially for dusty conditions (Zurek [1976] found this to be the region and condition for maximum tidal effects). The strong vertical mixing found over equatorial latitudes from low to mid levels of the model may be a combination of the tides and the effects of topographically forced stationary waves. These results are supported by the figures provided by Barnes [1994, personal communication], which indicate the regions most influenced by the transient and stationary eddies as well as the thermal tides. A further method of examining the sources of the strong mixing would be to examine the GCM wind data for the components associated with the transient eddy time scales and the tidal time scales. This would be a desirable goal of future work in this type of study.

5.4 Transport Time Scales

For purposes of comparison, Table 1 shows time scales based on advection alone (t_A) and diffusion alone (t_d). The advective time scale is based on the mean meridional circulation while the diffusive time scales are estimated based on the calculated K values. In Table 1 it is seen that the time scales are similar for advection and diffusion. Overall, the time scales associated with the Mars

“stratosphere” (from $\sim 5 - 50$ days) are vastly shorter than those associated with the Earth’s (up to 1.8 years).

Based on the effective transport circulation wind speeds, the time scales for complete overturning of the “stratosphere” are 35 days for the spring equinox case, 20 days for the clear northern winter solstice case, and 7 days for the dusty northern winter case. (It should be noted that the stratosphere will only overturn at these rates if these circulations are maintained for the appropriate lengths of time computed.) The solstice season circulations overturn the stratosphere much faster than the equinox circulation, and a dusty atmosphere causes the overturning to occur much more rapidly. The results also indicate that there is little difference in mean overturning between the Eulerian and transport circulations. This is because the eddy transport process has little effect on the mean advective transport, except at low levels.

5.5 Conclusions

The major findings of this study are as follows:

1. Zonal mean winds
 - change structure and intensity with season
 - change intensity (increase) with atmospheric dust
2. Mean meridional circulation
 - changes structure and intensity with season
 - changes intensity (increases) and depth with dust

3. Effective transport circulation

- similar in structure to mean meridional circulation
- responds similarly to changes in season and dust loading
- slightly stronger than the mean meridional circulation in regions of strong diffusive mixing

4. Eddy diffusion coefficients

- values change considerably with season, dust loading, and location in the atmosphere
- locations of strong mixing give an indication of the eddy sources of the mixing: thermal tides and transient eddies appear to play major roles
- the values calculated here (especially for K_{zz}) represent a lower bound, since the transport is only by larger-scale motions

5. "Stratospheric" overturning time scales

- time scales range from approximately 5–50 days depending on season and dust loading
- these time scales are dramatically shorter than those for Earth
- advective and diffusive time scales are comparable

Overall, this study has provided insight into the nature of the atmospheric circulation and transport processes of the Martian atmosphere for three sets of conditions. This study has examined the structure and intensity of the circulation, the transport of a hypothetical tracer species, the sources of atmospheric mixing, as well as the time scales of "stratospheric" overturning. In addition, a set of eddy diffusion coefficients (representing a lower bound for these coefficients) has been calculated for each experiment.

Bibliography

- Anderson, E. and C.B. Leovy, 1978: Mariner 9 Television Limb Observations of Dust and Ice Hazes on Mars. *J. Atmos. Sci.*, 35, 723–734.
- Andrews, D.G., J.R. Holton, and C.B. Leovy, Middle Atmosphere Dynamics, Academic Press Inc., Orlando, 1987, pp 343–391.
- Andrews, D.G., and M.E. McIntyre, 1978: An exact theory of nonlinear waves on a Lagrangian-mean flow. *J. Fluid Mech.*, 89, 609–646.
- Chamberlain, J.W. and D.M. Hunten, Theory of Planetary Atmospheres: An Introduction to Their Physics and Chemistry, Academic Presses, Inc., Orlando, 1987, pp. 89, 141.
- Clark, J.H.E., and T.G. Rogers, 1978: The transport of conservative trace gases by planetary waves. *J. Atmos. Sci.*, 35, 2232–2235.
- Colburn, D.S., J.B. Pollack, and R.M. Haberle, 1989: Diurnal Variations in Optical Depth at Mars. *Icarus*, 79, 159–189.
- Conrath, B.J., 1971: Thermal Structure of the Martian Atmosphere During the Dissipation of the Dust Storm of 1971. *Icarus*, 24, 36–46.
- Haberle, R.M., 1986: The Climate of Mars. *Sci. Amer.*, 254, 54–62.
- Haberle, R.M., J.B. Pollack, J.R. Barnes, R.W. Zurek, C.B. Leovy, J.R. Murphy, H. Lee, and J. Schaeffer, 1993: Mars Atmospheric Dynamics as Simulated by the NASA Ames General Circulation Model 1. The Zonal-Mean Circulation. *J. Geophys. Res.*, 98, 3093–3123.
- Houghton, J.T., The Physics of Atmospheres, (2nd edition), Cambridge University Press, Cambridge, 1986, pp. 58, 129–131, 175.
- Kida, H., 1983a: General circulation of air parcels and transport characteristics derived from a hemispheric GCM. Part 1. A determination of advective mass flow in the lower stratosphere. *J. Meteor. Soc. Japan*, 61, 171–187.
- Kong, T.Y., and M.B. McElroy, 1977: Photochemistry of the Martian Atmosphere. *Icarus*, 32, 168–189.

- Leovy, C.B., 1982: Martian Meteorological Variability. *Adv. Space Res.*, 2, 19–44.
- Lettau, H., 1951: Diffusion in the Upper Atmosphere. *Compendium of Meteorology*, T.F. Malone, Ed., Academic Press, 320–333.
- Levine, J.S., The Photochemistry of Atmospheres, Academic Press Inc., Orlando, 1985, pp. 8, 9, 20–21, 169, 298–299, 360–361.
- Matsuno, T., 1980: Lagrangian Motion of Air Parcels in the Stratosphere in the Presence of Planetary Waves. *Pure Appl. Geophys.*, 118, 189–216.
- Murphy, J.R., O.B. Toon, R.M. Haberle, and J.B. Pollack, 1990: Numerical Simulations of the Decay of Martian Global Dust Storms. *J. Geophys. Res.*, 95, 14,629–14,648.
- Pasquill, F. and F.B. Smith, Atmospheric Diffusion, (3rd edition), Ellis Horwood Limited, West Sussex, 1983, pp. 41, 88–97.
- Plumb, R.A., 1979: Eddy Fluxes of Conserved Quantities by Small-Amplitude Waves. *J. Atmos. Sci.*, 36, 1699–1704.
- Plumb, R.A., and J.D. Mahlman, 1987: The Zonally Averaged Transport Characteristics of the GFDL General Circulation/Transport Model. *J. Atmos. Sci.*, 44, 298–327.
- Pollack, J.B., Atmospheres of the Terrestrial Planets, in The New Solar System, edited by J.K. Beatty and A. Chaikin, Cambridge University Press, Cambridge, 1990, pp. 91–106.
- Pollack, J.B., R.M. Haberle, J. Schaeffer, and H. Lee, 1990: Simulations of the General Circulation of the Martian Atmosphere 1. Polar Processes. *J. Geophys. Res.*, 95, 1447–1473.
- Santee, M. and D. Crisp, 1994: Diagnostic Calculations of the Circulation in the Martian Atmosphere. Unpublished article submitted to *J. Geophys. Res.*
- Sutton, O.G., Micrometeorology, McGraw-Hill Book Company, New York, 1953, pp. 61–70.
- Shia, R.L., Y.L. Yung, M. Allen, R.W. Zurek, and D. Crisp, 1989: Sensitivity Study of Advection and Diffusion Coefficients in a Two-Dimensional Stratospheric Model Using Excess Carbon 14 Data. *J. Geophys. Res.*, 94, 18,467–18,484.

- Toon, O.B., J.B. Pollack, and C. Sagan, 1977: Physical Properties of the Particles Composing the Martian Dust Storm of 1971–1972. *Icarus*, 30, 663–696.
- Toon, O.B., R.P. Turco, D. Westphal, R. Malone, and M.S. Liu, 1988: A Multi-dimensional Model for Aerosols: Description of Computational Analogs. *J. Atmos. Sci.*, 45, 2123–2143.
- Zurek, R.W., 1976: Diurnal Tide in the Martian Atmosphere. *J. Atmos. Sci.*, 33, 321–337.
- Zurek, R.W., 1981: Inference of Dust Opacities for the 1977 Martian Great Dust Storms from Viking Lander 1 Pressure Data. *Icarus*, 45, 202–215.